SANDIA REPORT
SAND2008-5737
Unlimited Release
Printed September 2008

Modeling Pore Corrosion in Normally Open Gold-Plated Copper Connectors

Harry Moffat, Amy Sun, David Enos, Lysle Serna, Rob Sorensen, and Corbett Battaile

Prepared by
Sandia National Laboratories
Albuquerque, New Mexico 87185 and Livermore, California 94550

Sandia is a multiprogram laboratory operated by Sandia Corporation,
a Lockheed Martin Company, for the United States Department of Energy's
National Nuclear Security Administration under Contract DE-AC04-94AL85000.

Issued by Sandia National Laboratories, operated for the United States Department of Energy by Sandia Corporation.

Available to DOE and DOE contractors from
U.S. Department of Energy
Office of Scientific and Technical Information
P.O. Box 62
Oak Ridge, TN 37831

Telephone: (865) 576-8401
Facsimile: (865) 576-5728
E-Mail: reports@adonis.osti.gov
Online ordering: http://www.osti.gov/bridge

Available to the public from
U.S. Department of Commerce
National Technical Information Service
5285 Port Royal Rd.
Springfield, VA 22161

Telephone: (800) 553-6847
Facsimile: (703) 605-6900
E-Mail: orders@ntis.fedworld.gov
Online order: http://www.ntis.gov/help/ordermethods.asp?loc=7-4-0#online

SAND2008-5737
Unlimited Release
Printed September 2008

Modeling Pore Corrosion in Normally Open Gold-Plated Copper Connectors

Harry Moffat
Nanoscale and Reactive Processes

Amy Sun
Geohydrology

David Enos, Lysle Serna, Rob Sorensen
Materials Reliability

Corbett Battaile
Computational Materials Science and Engineering

Sandia National Laboratories
P.O. Box 5800
Albuquerque, NM 87185-0888

Abstract

The goal of this study is to model the electrical response of gold plated copper electrical contacts exposed to a mixed flowing gas stream consisting of air containing 10 ppb H_2S at 30°C and a relative humidity of 70%. This environment accelerates the attack normally observed in a light industrial environment (essentially a simplified version of the Battelle Class 2 environment). Corrosion rates were quantified by measuring the corrosion site density, size distribution, and the macroscopic electrical resistance of the aged surface as a function of exposure time. A pore corrosion numerical model was used to predict both the growth of copper sulfide corrosion product which blooms through defects in the gold layer and the resulting electrical contact resistance of the aged surface. Assumptions about the distribution of defects in the noble metal plating and the mechanism for how corrosion blooms affect electrical contact resistance were needed to complete the numerical model. Comparisons are made to the experimentally observed number density of corrosion sites, the size distribution of corrosion product blooms, and the cumulative probability distribution of the electrical contact resistance. Experimentally, the bloom site density increases as a function of time, whereas the bloom size distribution remains relatively independent of time. These two effects are included in the numerical model by adding a corrosion initiation probability proportional to the surface area along with a probability for bloom-growth extinction proportional to the corrosion product

bloom volume. The cumulative probability distribution of electrical resistance becomes skewed as exposure time increases. While the electrical contact resistance increases as a function of time for a fraction of the bloom population, the median value remains relatively unchanged. In order to model this behavior, the resistance calculated for large blooms has been weighted more heavily.

CONTENTS

1.0 Introduction

Atmospheric corrosion of intermittently-mated electrical connectors can lead to increased contact resistance and reduced reliability of the devices that contain them. Typical measures taken to protect such devices include an electroplated layer of nickel followed by an electroplated layer of gold. The primary purpose of these cover layers is to provide the connector with increased resistance to environmental degradation while maintaining a low contact resistance, thereby enhancing the long-term reliability of the connector. Electrodeposited gold is inherently porous, with the degree of through-deposit porosity being a function of the deposit thickness, deposition technique (i.e., pulsed vs. DC), substrate surface roughness, substrate surface contamination, and the use of a multilayer deposit (e.g., gold on top of nickel) [1]. Through-deposit porosity allows the underlying substrate material, in the case of this work, copper, to be exposed and potentially undergo atmospheric corrosion. Such corrosion often results in corrosion product growth through the pore onto the surface of the electrodeposited gold. If extensive enough, the resulting corrosion products may degrade the electrical performance of the connector.

The primary goals of this research are two fold: 1) to first characterize the degradation mechanisms of gold-plated copper, as used in microelectronic connectors, and 2) to construct an appropriate mathematical model encompassing the key physical phenomena. This model, once calibrated via experimental data, may then be utilized to predict the electrical contact resistance of actual devices, such as electrical connectors, a very practical and important goal [2], and then linked with a system-level electrical model to assess the impact which the corrosion process will have on system performance.

In this report, we build upon our earlier work on understanding the kinetics of the sulfidation process for pure copper coupons in an H_2S containing environment with a moving-boundary model for pore growth in an effort to understand the corrosion of gold-plated copper [3]-[6]. While the kinetics of the sulfidation process is expected to be similar microscopically, there are least two significant phenomenological differences between the sulfidation of bare copper and the sulfidation of noble metal-plated copper that we have seen necessary to add in order to fit experimental data on corrosion bloom densities. A longer induction period is observed prior to the onset of corrosion (i.e., the observation of corrosion product on the metal surface) for the noble metal-plated materials. This induction period appears to also be a function of the environmental conditions and plating morphology. Furthermore, the induction period for the initiation of corrosion at a given defect site varies significantly from site to site, and is believed to be a strong function of the geometric nature of each defect site. This variation in induction time is manifested experimentally in this study by the continuous nucleation of corrosion product blooms through exposure times (multiple months). Additionally Kirkendall voiding, also seen in the sulfidation of bare copper is concentrated under the pore. We believe this effects leads to a reduction in the concentration of large blooms due to a cutoff of their Cu source. With the inclusion of Kirkendall voiding combined with the inclusion of an induction period we have successfully matched experimental data on the time dependence of the number of corrosion flowers and their distribution (see Section 4.2 and 4.3).

Once the model has been assembled, the resulting predictions of the corrosion process provide the basic inputs for a macroscopic electrical contact resistance model. To our knowledge, such a complete corrosion-to-electrical resistance model has not been attempted in other works. Sun et al. have attempted to model the growth of corrosion product blooms on Au/Ni/Cu in the Battelle Class II, mixed flowing gas (MFG) environment [7]. While they did employ one-dimensional diffusion equation in Cartesian and cylindrical coordinates, they did not use a moving boundary approach to locate the extent of the solid corrosion product.

As a necessary precursor to treating the contact between corrosion-aged surfaces, we present the theory of contact between two rough surfaces in Section 5.1, that we have employed and that underlies much of the numerical analysis. This theory provides a model for the number and size of asperities created by contact of two rough surfaces as a function of the load of the contact. The ratio of the apparent to nominal area of contact is obtained as a function of the surface pressure to microhardness of the materials. This theory assumes plastic deformation of asperities; however, the assumption of elastic deformation does not yield much different results. The theory also provides an estimate of the amount of overlap between contacting asperities, which we call the Interference.

We then derive an electrical contact resistance model for aged surfaces based on the rough surfaces contact model. The original theory for clean surfaces was developed by Greenwood. Malucci has taken that theory and modified for aged surfaces where a corrosion product layer is postulated to interfere with the direct metal-metal contact at asperities. We use the concept of the Interference to develop a statistical derivation of the number of micro-asperity contacts that are created during the contacting process that have metal-metal contacts. We employ this theory, because it has been shown on some experimental data in the literature to be critical to obtaining the overall magnitude of the electrical contact resistances and their cumulative probability distributions) observed. However, we should also note that no direct experimental verification of the theory (or even numerical experimentation) has been carried out yet.

We then combine our predictions for growth of the corrosion product layer on plated copper with our electrical contact resistance model to yield predictions of the electrical contact resistance. We do this by postulating that there is a separation of the corrosion blooms into small and large bins. The small values are lumped together to estimate the time dependence of a uniform corrosion product layer, that we then use the contact resistance model for aged surfaces developed previously to estimate electrical contact resistances. The distribution of large blooms is handled differently. It has been experimentally shown that large corrosion blooms may significantly occlude electrical contacts. Therefore, we have implemented a stochastic model wherein probes making contact with surfaces undergo poisson statistics to test whether they hit a large bloom based on the probability density distribution of large blooms on that surface. This process has been shown to predict the large tails in the cumulative probability distribution (CPD) that we have experimentally observed.

Despite all of these heuristic submodels, we present evidence that we have had trouble reproducing experimental measurements for the CPD of electrical contacts made from electroplated copper. Specifically, we have determined that we have trouble even reproducing the zero-time (i.e. baseline) CPD of electrical contact resistance and its dependence on load. None of the available numerical modeling theories for electrical contact resistances can duplicate

the large absolute magnitude and load dependence of the electrical contact resistances that we see in our data. We have searched for experimental causes for these discrepancies, using Auger sputtering analysis to characterize the baseline surface film composition and thickness and using optical interferomentry to analyze the surface roughness of the after-electroplating surface. We have varied probe tip radii and the presence of wipe to try to understand the trends as well. Recently we have varied the plating materials and thicknesses and have noticed a dramatic effect on the baseline resistances (Section 7.2). Our current theory is that the electroplating process is the important contributor to the baseline resistance, and we have developed a theory (Section 7.1) based on the existence of a buried layer of electrical contact resistance due to imperfections in the plating process that matches experimental trends with respect to the load dependence. With the baseline data relatively well matched, we then go on to match exposed plated-copper surfaces in Section 7.5. We conclude that the theory is robust enough to match experimental data on the H_2S system at 80% humidity conditions after a proper amount of calibration is carried out.

Finally, recent experiments at near 10% relative humidity has demonstrated a significant and surprising departure from bare copper experimental results. Much less corrosion is observed in the 10% relative humidity case than in the 70% relative humidity case, in stark contrast to the bare copper data where the 10% humidity level actually exhibited larger corrosion film thicknesses. We postulate that the induction effect due to corrosion initiation is the cause of the different 10% results.

2.0 Sulfidation Kinetics of Bare Copper

The sulfidation of atmospherically exposed copper occurs through a chemical reaction between metallic copper and the H_2S in the gas stream. Historical experimental data measuring the growth of the copper sulfide layer as a function of exposure time at different H_2S concentrations and at different relative humidity concluded that the growth consisted of two stages [8, 9, 10]. This two stage growth is illustrated schematically in Fig. 1. In Stage I, the kinetics of copper sulfide formation is either gas-phase mass transport or surface-reaction controlled, and the thickness of the sulfide layer is proportional to kT, where k is the surface reaction rate constant. With time, the growth mode transitions to Stage II, where the growth rate is controlled by diffusion through the sulfide layer and the resulting sulfide layer thickness becomes proportional to $(Dt)^{0.5}$, where D is the effective diffusivity through the sulfide layer and t is time. While this second stage is followed by a third stage during which the sulfide layer begins to spall, exposing fresh material which can then sulfidize, only the first two stages are of relevance to this study. The kinetics of the sulfidation reaction in Stage I and II have been found to be effectively independent of relative humidity. However, the transition from Stage I to Stage II has been found to be impacted by the relative humidity [11, 12]. Higher humidity promotes a more rapid transition to Stage II (i.e., the length of Stage I growth appears to decrease with increasing relative humidity).

Studies of the initial nucleation of Cu_2S on bare copper coupons have shown that the relative humidity has a large effect on the initial structure of the Cu_2S formed. Under conditions of high RH, the sulfide film is initially patchy with numerous nodular sulfide nuclei, while at low RH initial film formation is more uniform across the surface. Cross-sectional TEM images of the resulting sulfide layers indicate that the grain structure also varies as a function of RH. When formed at low RH, the resulting Cu_2S layer is composed of large grains that span the thickness of the film, while films formed at high RH consist of small grains with high porosity between the grains. As such, it is possible that the transition to Stage II may be related to the evolving grain structure of the product layer. It should be noted that the transition from Stage I to Stage II growth appears to be irreversible - in experiments where copper coupons were allowed to sulfidize at one at a high RH, transitioned to Stage II, then placed into a lower RH, the film never returned to Stage I growth kinetics, even when the RH is reduced dramatically [15]. To date, the exact mechanism of how the RH changes product morphology remains unknown. Another complicating factor for understanding the growth kinetics during Stage II is that the vacancy diffusivity in Cu_2S can vary greatly, with values reported in the literature ranging from $2x10^{-7}$ to $2x10^{-11}$ cm^2/s, depending on the source/production method for the sulfide. Given the aforementioned variations in both effective diffusivity and microstructure, we have chosen to model diffusion within this system using an engineering-level approximation based on a single experimentally-fitted effective bulk diffusion coefficient.

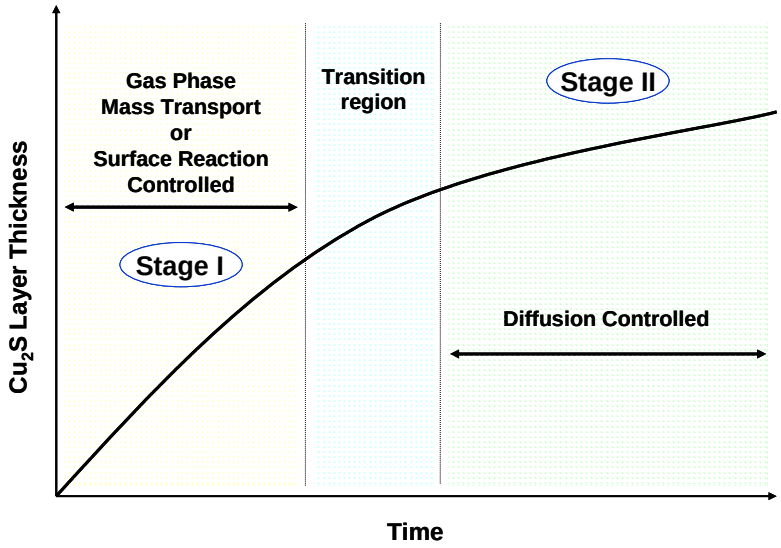

Fig. 1 Schematic representation of the Cu_2S growth rate on bare copper coupons exposed to an H_2S containing atmosphere. In Stage I, the growth rate is controlled by either gas phase mass transport or surface reaction, while for Stage II, the kinetics are dominated by diffusional transport through the bulk Cu_2S layer and grain boundaries within the Cu_2S layer.

2.1 Bare Coupon H_2S Experiments with Modeling Attempts

The rate of copper sulfidation, while in Stage I, has been experimentally observed to be a linear function of the H_2S concentration, with an activation energy of approximately 5-10 kcal mol^{-1}. During this stage, sulfide growth is controlled primarily by either gas phase mass transport or by partial surface reaction control [6]. Detailed experiments by Braithwaite et al. [11] have shown that the growth rate in this stage is roughly independent of the relative humidity level. This experimental observation is in stark contrast with many other atmospheric corrosion systems where the corrosion rate is typically negligible until a critical relative humidity is reached, at which point sufficient water is present on the surface to support electrochemical reactions. Experiments indicated that there is a small increase (50% from 0 to 80 % RH) in the Stage I growth rate with increasing relative humidity. However, corrosion rates are nearly at the mass transfer limit.

Initial modeling attempts for Cu_2S growth [8] had missed the relative fast reaction rates observed in Stage I. They missed it, because gas-phase mass transport interfered with the calculation of the sticking coefficient. Previously, we undertook a study to mitigate the mass transport resistance by constructing a stagnation point flow reaction and using a large and varying normal velocity to minimize the mass transport resistance[11, 16]. Numerical calculations were then carried out to model the predicted initial growth rates obtained from normal incidence reflectometry to obtain an estimate of the reactive sticking coefficient for the initial sulfidation rate. A reactive sticking coefficient of 10^{-3} fit the dependence of the growth rate

with inlet velocity (see Fig. 2). This is a very fast reaction and indicates very little practical kinetic resistance to the overall reaction (R1), which can be shown to be thermodynamically very favorable.

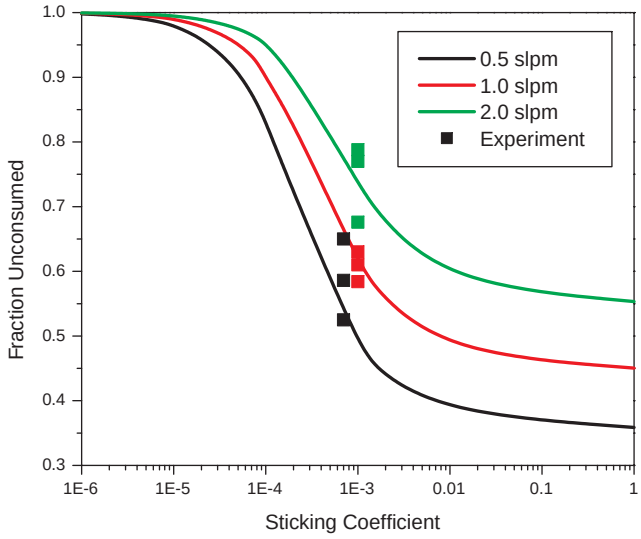

Fig. 2 Velocity dependence of the reactive sticking coefficient for copper sulfidation on a bare copper coupon in a stagnation point flow reactor [16]. Curves are numerical calculations as a function of the input reactive sticking coefficient. Squares are single experimental data points for 2, 1, and 0.5 slpm (standard liters per minute), respectively. A sticking coefficient value of around 1.0E-3 is shown to fit the observed experimental values well to within a factor of two.

$$H_2S + 2\,Cu + 1/2O_2 \rightarrow Cu_2S + H_2O \qquad \text{(R1)}$$

Rutherford Backscattering (RBS) experiments have verified the mechanism for growth of the copper sulfide film [11]. It was shown that the copper sulfide film grows at the sulfide-water film interface and not at the buried sulfide-copper interface. This conclusion is based upon the observation of a residual copper-oxide film and/or an added patterned gold layer which becomes buried beneath the sulfide layer as the sulfidation reaction progresses.

Once the sulfide layer has formed and grown to a certain thickness under Stage I, it transitions to Stage II. Experiments have indicated that when this transition occurs is a statistical process that is highly variable. While the time after which this transition takes place does appear to be a function of the relative humidity, with increased humidity accelerating the transition to Stage II, the actual “induction time” is widely variable for a given relative humidity, particularly for intermediate levels of relative humidity. However, at very low relative humidity, the onset of Stage II can be virtually eliminated, with experiments conducted at 0% RH demonstrating that the Stage I growth can persist even for sulfide film thicknesses in excess of 1 micron. TEM studies by Sullivan et. al. have pointed to a possible explanation for this transition to Stage II phenomena [12]. It involves the changing grain structure of the Cu_2S film as the film gets larger. At low relative humidities the grain structure is well formed, and roughly columnar in nature,

while at high relative humidities the grain size is considerably smaller, with poorly connected and voided grain boundaries. Sullivan et. al. [12] proposed that the difference in grain morphology at high and low RH suggests a natural mechanism for the observed reduction in sulfidation rate at long times for films grown at RH. They hypothesized that the poor connectivity between grains inhibits the solid state transport of Cu through the Cu_2S layer. In essence, the bottleneck is the inability for Cu to diffuse between grains of Cu_2S, and not the inability to diffuse Cu within grains. It is likely that the diffusion of Cu within the grains may still be rapid in the high RH samples, similar to what is seen in the low RH case (at least there is no data to contradict this) [12]. Thus, the thesis has been advanced that the rate limiting step in Stage II is the mass transport resistance of copper vacancies transit across the copper sulfide layer as they make their way between the water surface and the copper surface. This thesis is backed up by the growth rate observations, and by the general statistical variability of the growth rate experiments observed in practice. Also, experiments in which Stage II grain morphologies have been initially grown, and then the RH lowered have shown that the growth rate of Cu_2S never returns to Stage I rates [12].

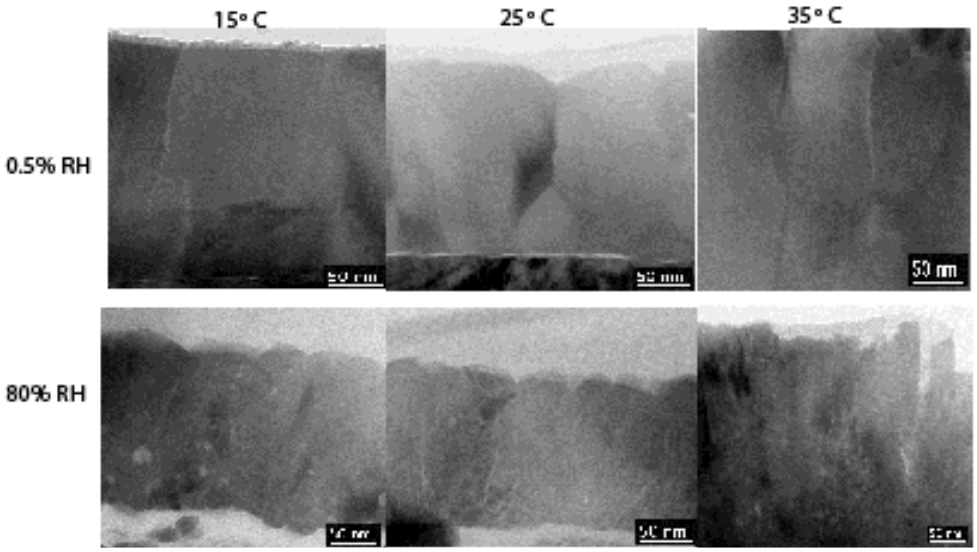

Fig. 3 Cross-section TEM images of Cu_2S films formed at low and high RH and a range of temperatures [12]. For a given RH, the morphologies are similar with the low RH samples exhibiting large grains that span the film and the high RH samples exhibiting small grain sizes and high porosity.

These observations partly resolve an outstanding issue concerning the resolution of the effective diffusivity of copper vacancies passing through the sulfide layer. It's been known that the diffusion coefficient needed to explain the Stage II phenomena by the onset of a solid-state mass transport effect is too high compared to measured diffusion coefficients from crystalline (or polycrystalline) chalcocite experiments. This is in accordance with the rate limiting step being identified with the mass transport of vacancies across grain boundaries and not with the diffusion of copper vacancies within crystalline chalcocite. Diffusion of copper vacancies within a grain is presumed to be sufficiently fast as to not be rate limiting.

Experiments by Braithwaite et al. [16] suggests that there may be an additional initial induction stage, "stage 0", in the growth evolution of copper sulfide films. Fig. 4 displays H_2S concentration data, acquired for various levels of the relative humidity level, for a flow rate of 1 slpm. In the graph, "Normalized H_2S Loss" corresponds to the loss of H_2S from gas stream as it passes from the inlet to the outlet of the reactor, assumed here to be due to consumption by the copper sulfidation reaction. The data was normalized via the first data point for H_2S effluent concentration, where presumably the H_2S sticking coefficient is so low that no loss of H_2S in the reactor occurs. There are several trends of note illustrated by the data in Fig. 4 . First, it can be seen that the transition to Stage II was only observed for the high humidity level cases (i.e., RH >60%) during the time window presented in the figure. At the lower relative humidities, there is a complex dependence of the rate of consumption of H_2S (and by inference, the rate of copper sulfidation) on the humidity level, with an apparent maximum observed at 60%. Also, the steady state H_2S consumption rate observed during Stage I appears to be a roughly linear function of the relative humidity, increasing as the relative humidity increases. This may be the result of enhanced destruction of the native oxide layer in the higher RH environment, or the high nucleation rate of new copper sulfide grains observed during Stage I in high humidity environments.

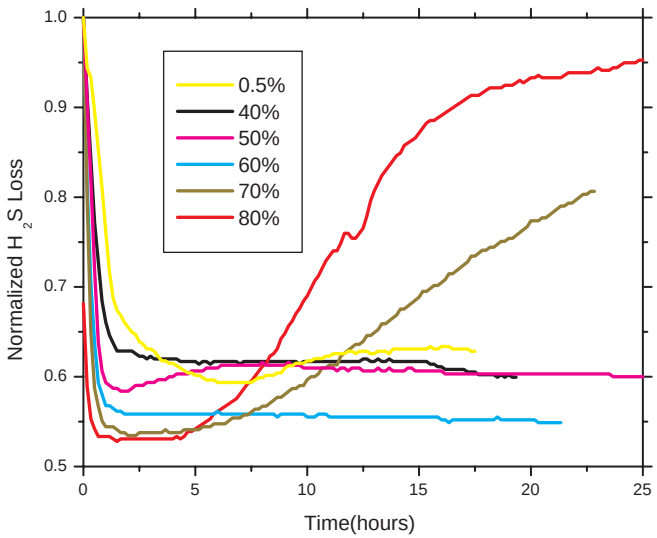

Fig. 4 Fraction H_2S lost versus time as function of varying humidity level in the stagnation point flow reactor

In addition, the data presented in Fig. 4 also shows that high humidity levels promote the onset of Stage II, and therefore lower sulfidation rates, at later times. Thus, the experiments in Fig. 4 clearly indicate that there is an induction period, or "Stage 0", representing the delay before the time independent, rapid consumption of H_2S by the sulfidation reaction (Stage I) is achieved. We presume that this delay is associated with the removal or the "compromising" of the native Cu_2O oxide layer. Earlier experiments by Barbour [13] has shown that the H_2S – Cu system may exhibit completely different behavior if the native Cu_2O oxide layer is replaced by the more resilient CuO oxide layer, grown by a plasma processing technique. In this case, sulfidation may not occur at all under some conditions.

One pathway that was not pursued in this work was to treat the full copper sulfide diffusion in a rigorous manner. For example, it's known that copper vacancies are the main ionic diffusing species in copper sulfides, and that the copper vacancies are mostly but not completely ionized [14]. K Chen [5] has undertaken a treatment of Cu_2S growth from H_2S using charged species (V- and h+), using the Gauss's equation to solve for the electric field within the Cu_2S. The diffusion of then negatively charged vacancy across the interfaces causes a narrow space-charge layer to be created at both the copper sulfide-air and the copper–sulfide copper metal interfaces that creates a net voltage drop across the copper sulfide proportional to the net growth rate. We have determined, however, that it is not necessary to pursue this level of detail because the overall mechanism doesn't involve a net electric charge transfer. Also, unlike localized pitting processes there isn't an inhomogeneous splitting of the surface between anodic and cathodic regions. This decision is also supported by Barbour's recent experiments (see Fig. 3) which demonstrated that the rate limiting step involves a very messy and complex diffusion process involving copper transport across grain boundaries.

This report details our work in obtaining a best fit to the current constitutive model for the atmospheric sulfidation of copper from a H_2S source. Since the copper sulfidation reaction model has been documented in previous references [3–6], this report will not attempt to re-derive the kinetic mechanism, and the readers are referred to the papers for detailed descriptions. We will, however, be attempting to fit kinetic rate constants and diffusion coefficients in the model to a selected set of experimental data. In the next section, a description of the model is given. Characteristics of the equations are also listed in the same section. This is followed by a description of the experimental data. The optimization methodology used for fitting the parameters is also presented. Finally, the results and discussion follow.

2.2 Model Used in Plated Copper Work

The kinetic model for copper sulfidation used in this work is similar to the one described by Larson [3]. A one dimensional schematic of the sulfidation process indicating material domains where reactions occur is illustrated in Fig. 5. The model used to describe the kinetics consists of three parts: the gas-solid surface reaction which produces copper sulfide, the diffusion of copper vacancies through the Cu_2S layer, and a solid-solid surface reaction involving the injection of a copper atom into the Cu_2S layer from the copper metal causing the annihilation of

the copper vacancy in the Cu_2S layer. This model is a gross engineering approximation to the complex physical mechanism briefly discussed in the last section.

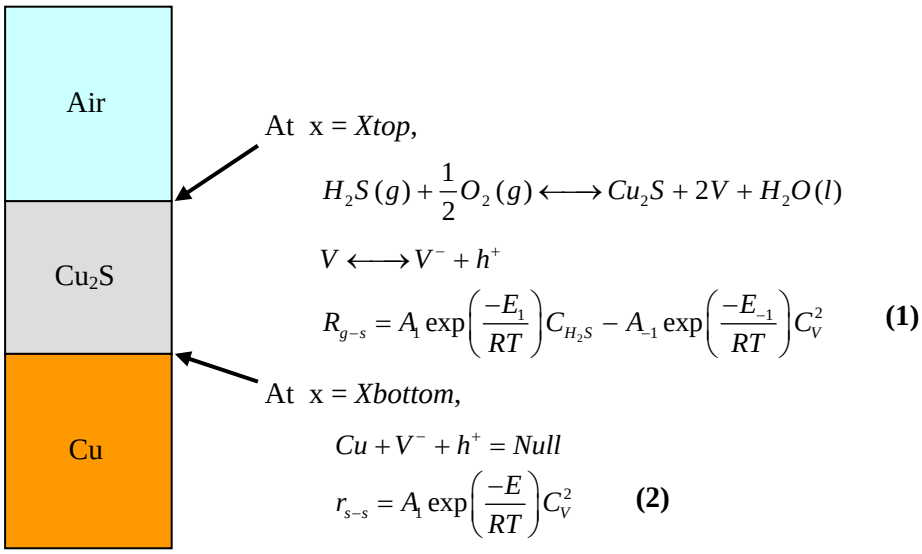

Fig. 5 Schematic of 1-D copper sulfidation corrosion model.

The H_2S reacts with copper to form copper sulfide. At $x = X_{top}$,

$$R_{g-s} = A_1 \exp(\frac{-E_1}{RT})C_{H_2S} - A_{-1}\exp(\frac{-E_{-1}}{RT})C_V^2 . \quad (1)$$

$R_{g\text{-}s}$ refers to the reaction rate for copper sulfidation at the air-Cu_2S interface (mol cm^{-2} s^{-1}). C_{H2S} is the concentration of hydrogen sulfide in units of mol cm^{-3}. C_V is the concentration of copper vacancies on copper lattice sites within the copper sulfide. Even though copper vacancy carriers, C_{V^-}, are comprised of vacancies with excess electrons, C_{V^-}, and electron holes, h^+, this model assumes a vacancy dissociation rate that is much slower and unfavorable than the time scale of the surface reaction. This reduces the combined quartic dependency of C_{V^-} plus C_{h+} down to a quadratic dependency in C_V, only. Electroneutrality is also assumed in this model; i.e., $C_{V^-} = C_{h+}$; hence, we ignore mass transfer contribution due to electrical potential.

There is a linear dependency on the H_2S concentration to yield Stage I growth initially. As the copper vacancy concentration increases within the corrosion layer, the rate of growth slows, capturing the slower growth rate observed experimentally in Stage II. Each of the forward and backward kinetic parameters in Eqn. (1) has an Arrhenius-like pre-factor. The units of pre-exponential factors are cm s^{-1} for A_1 and cm^4 mol^{-1} s^{-1} for A_{-1}.

The kinetic rate at the interface between the corrosion product and pure copper is defined by $R_{s\text{-}s}$. At $x = X_{bottom}$,

$$R_{s-s} = A_2 \exp(\frac{-E_2}{RT})C_V^2 . \quad (2)$$

The explicit dissociation of copper vacancies into charged vacancies and electron holes, as well as the electromigration effect of an induced electric potential, are ignored in this model. In other words, we do not independently track the concentrations of neutral copper vacancies, charged vacancies, and electron holes, while taking into account of electromigration forces induced by potential gradients. Under these conditions, it's expected that vacancies mostly exist in the charged state. However, the reaction rate expression for the vacancy elimination reaction, Eqn. (2), contains a quadratic dependence on C_{V}, which is due to the anticipated charged-vacancy and hole recombination, and the expected electroneutrality condition that the charged vacancies and holes are in equal concentrations almost everywhere except for a thin boundary layer at the surfaces.

The existence of an aqueous interfacial phase (i.e., partial or complete monolayer of water) at the gas-Cu_2S interface is also ignored. As mentioned above, the effects of relative humidity can be large, but the exact mechanism is still unknown. Experiments and related modeling have shown that the sticking coefficient for H_2S is surprisingly high and relatively unrelated to the humidity levels [16]. This model does not account for changes in growth rate due to changes in the relative humidity. Because the experimental data have been collected under a constant relative humidity, the sensitivity to RH is not accounted for in the model. Diffusion of uncharged species is employed, assuming electroneutrality throughout. A single experimentally-fitted effective bulk diffusion coefficient is used to represent the complex transport mechanism involving the structure of grain boundaries in the product layer previously discussed in the earlier section.

The diffusion of uncharged copper vacancies through the Cu_2S layer is written as a single-component diffusion equation, assuming electroneutrality.

$$\frac{\partial C_{\mathrm{V}}}{\partial t} - D_{\mathrm{V}} \frac{\partial^2 C_{\mathrm{V}}}{\partial x^2} = 0 \tag{3}$$

D_v is set to a constant in this model, though there is a storied literature concerning the dependence of the vacancy diffusion coefficient on the vacancy concentration of nonstoichiometric crystalline Cu_2S [17, 18]. Eqn. (3) and its corresponding boundary conditions at the gas-solid and solid-solid interfaces define the concentration distribution of vacancies within the Cu_2S layer. Due to the volumetric increase of the Cu_2S as the corrosion process progresses, the location X_{top} evolves in time and is part of the solution unknowns.

Boundary conditions for incorporating the reaction kinetics are summarized below:

At $x = X_{top}$,

$$J_V = -\nu_{\mathrm{V}}^{g-s} R_{g-s} + v_{mesh} C_{\mathrm{V}} \tag{4}$$

and

$$\frac{dX_{top}}{dt} C^0_{\mathrm{Cu_2S}} = R_{g-s} \tag{5}$$

At $x=X_{\mathrm{bottom}}$,

$$J_{\mathrm{V}} = -\nu_{\mathrm{V}}^{s-s} R_{s-s} + v_{mesh} C_{\mathrm{V}} \tag{6}$$

and $v_{mesh} = 0$ (7)

where J_v is the concentration flux of copper vacancies (mol cm^{-}2 sec^{-1}) based on a moving frame of reference, and v_{mesh} is the mesh velocity, or dX_{top}/dt. Constants v_V^{g-s} and v_V^{s-s} are the stoichiometric coefficients for copper vacancies in the surface reactions at either end of the domain, which is two at the gas-solid interface and negative one at the solid-solid interface. $C_{Cu2S}{}^{o}$ is the molar concentration of the copper sulfide lattice, consisting of both vacancies and regularly filled lattice sites, assumed to be equal to 3.52 x 10^{-2} mol cm^{-3}, the value for chalcocite. At t = 0, a constant copper vacancy concentration in a small but finite film thickness is assumed. The initial concentration and thickness values, $C_V{}^{o}$ and L^{o}, have been chosen to minimize the sensitivities to the growth. They are 10-12 mol cm^{-3} and 1 μm, respectively. Because there is no mesh movement at the Cu_2S-Cu interface, the mesh velocity is set to zero at $x = X_{bot}$.

The vacancy diffusion coefficient and the rate constants for the gas-surface reaction were obtained by fitting solutions of Eqns. (3) - (7) to a series of growth experiments conducted on flat copper coupons [19, 20]. A rough degree of success has been achieved in crudely correlating experiments in the Cu_2S sulfidation system, at least for constant relative humidity, despite the large degree of difficulty in modeling the actual growth mechanisms involved in the real system. Results from this analysis are presented in Section 3.5. Rate constants in the model must be reparameterized for different relative humidities, however. In the next section we describe the numerical procedure used to solve the equation system.

3.0 One Dimensional Copper Sulfidation (CS) Numerical Model

Eqns. (3) through (7) are applied to a one-dimensional growth domain and discretized into multiple control volumes. The control volumes exchange copper vacancies via the diffusional flux expression and the Lagrangian movement of the node positions, X_i. All of the mesh positions move as a fixed function of the top mesh position, X_{top}, which is moved according to a kinematic boundary condition established by the growth of the copper sulfide layer, Eqn. (5). An integral balance is carried out over each control volume in both the physical and time coordinate in order to form the difference equations, which are then solved by a predictor-corrector backward Euler method.

The code uses Cantera's infrastructure for solving time dependent implicit problems [21]. It employs a numerical Jacobian approach such that only a single residual routine need be written. This residual routine uses a control volume approach, identical to that utilized by most CVFEM codes, and employs a space-time substantial time derivative approach that is locally conservative even in the presence of the moving mesh. Fig. 6 displays a schematic of the discretization scheme with $N = 6$ mesh points. There are 2 unknowns per control volume, the mesh position of the centroid of the i^{th} control volume, X_i^n, and the concentration of copper vacancies in the mesh, C_V, at the centroid of the control volume. Control volumes are centered at the node positions. Nodes are numbered from 0 to *N-1*. The edges of the control volumes, I_i, are located midway between the nodes. The control volumes at the top and bottom of the domain, numbered $N-1$ and 0 respectively, are special cases. The top control volume extends from $\left(X_{N-1}^n + X_{N-2}^n\right)/2$ to X_{N-1}^n. The bottom control volume extends from X_0^n to $\left(X_0^n + X_1^n\right)/2$.

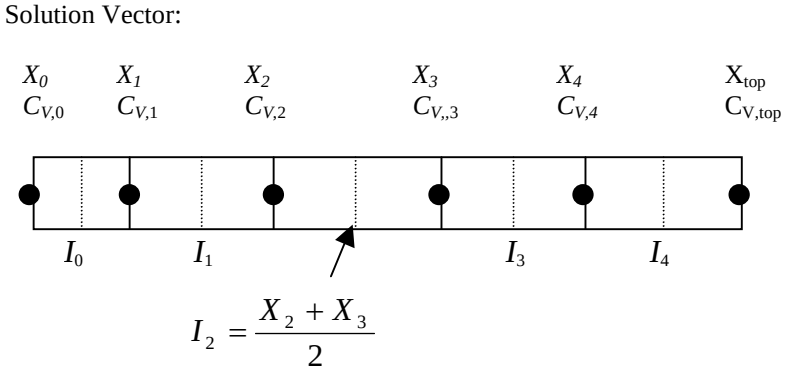

Fig. 6 Schematic of discretization scheme. Interfaces of control volumes are labeled with I_i. Centers of control volumes are labeled with X_i.

An integral balance is carried out over each control volume in both the physical and time coordinate in order to form the difference equations. The control volumes exchange copper vacancies via the diffusional flux expression and the movement of the node positions, X_i. All of

the mesh positions move as a fixed function of the top mesh position, X_{top}, which moves according to the kinematic boundary condition established by the growth of the copper sulfide layer. The equation for the interior mesh movement of node *i*, X_i, is given by Eqn. (8).

$$X_i - X_{bot}^0 = \frac{F_i}{F_{i+1}}\left(X_{i+1} - X_{bot}^0\right) \tag{8}$$

F_i is a fixed fraction of the distance of the initial position of node *i* between node 0 and node $N-1$. It varies monotonically between 0 and 1. In the initial implementation of this code F_i is uniformly distributed between 0 and 1. The expression for the movement of the top node, on which the movement of all of the other nodes is tied, is addressed below.

The diffusion of uncharged copper vacancies through the Cu_2S layer is written as a pure diffusion equation, see Eqn. (3), assuming electroneutrality. The discretization described in Fig. 6 requires that the concentration of vacancies be tracked as the layer moves through the domain pictured in Fig. 5, i.e., the copper vacancy concentration unknowns in Fig. 6 are substantial time derivatives and not partial derivatives, since their physical position moves with time. The substantial derivative creates a term similar to a convection term. The Reynolds transport theorem which relates the substantial derivative to the partial derivative is given by Eqn. (9).

$$\frac{D}{Dt}\int_{V(t)} C_V \, dV = \int_{V(t)} \frac{\partial C_V}{\partial t} dV + \int_{A(t)} C_V \left(\mathbf{v}_{mesh} \bullet \mathbf{n}\right) dA \tag{9}$$

After integrating Eqn. (3) over each control volume, Eqn. (9) may be applied to change the partial time derivative into a substantial time derivative, Eqn. (10).

$$\frac{D}{Dt}\int_{V_i(t)} C_V \, dV - \int_{A_i(t)} C_V \left(\mathbf{v}_{mesh} \bullet \mathbf{n}\right) dA + \int_{A_i(t)} \left(\mathbf{n} \bullet \left(-D_v \nabla C_V\right)\right) dA = 0 \tag{10}$$

This may be reduced to a partial differential equation on a moving mesh.

$$\frac{dC_V}{dt} - \mathbf{v}_{mesh} \bullet \nabla C_V + \nabla \bullet (-D_V \nabla C_V) = 0 \tag{11}$$

The key to understanding Eqn. (11) for the volumetric PDE is to understand that the unknowns C_V are actually the vacancy concentrations at the mesh grid points, and thus their time derivatives are substantial derivatives with respect to time and not partial derivatives with respect to time. However, the correct PDE equation involves the partial derivative with respect to time, only. Below we denote substantial time derivatives with vertical bars and a "mesh" subscript. Eqn. (3) is correct, irrespective of the complications induced by the movement of a mesh with variables defined on that mesh. A more complete analysis of the derivation of Eqn. (11), involving the invocation of the Reynolds transport theorem, does not have to be made, as nothing is actually moving in the frame of reference of the lattice. There is no convective component for vacancy transport in Eqn. (3), as the lattice is defined to be stationary. However, the substantial derivative creates a term similar to a convection term. The equation that relates the substantial derivative to the partial derivative is given by Eqn. (12).

$$\left.\frac{dC_{\mathrm{V}}}{dt}\right|_{mesh} = \frac{\partial C_{\mathrm{V}}}{\partial t} + \mathbf{v}_{mesh} \bullet \nabla C_{\mathrm{V}} \tag{12}$$

Then, a discretized formulation of Eqn. (10) may be constructed by assuming that the concentration within each control volume is constant, Eqn. (13).

$$\begin{aligned} &\frac{C_{V,i}^{n} V_i^{n} - C_{V,i}^{n-1} V_i^{n-1}}{\Delta t} + A_i^{n} F_{Cv,i}^{n} - A_{i-1}^{n} F_{Cv,i-1}^{n} \\ &\qquad - A_i^{n}\left(\frac{I_i^{n} - I_i^{n-1}}{\Delta t}\right) C_{V,i+1}^{n} + A_{i-1}^{n}\left(\frac{I_{i-1}^{n} - I_{i-1}^{n-1}}{\Delta t}\right) C_{V,i}^{n} = 0 \end{aligned} \tag{13}$$

where Eqn. (14),

$$F_{Cv,i}^{n} = -D_v \frac{C_{V,i+1}^{n} - C_{V,i}^{n}}{X_{i+1} - X_i}, \tag{14}$$

is the diffusive flux across the control volume boundary at I_i at $t = n$. In deriving Eqn. (13), the following formula for the convective flux through surface I was used.

$$\int_{A_i(t)} \left(\mathbf{v}_{mesh} \bullet \mathbf{n}\right) dA = A_i^{n} \frac{I_i^{n} - I_i^{n-1}}{\Delta t} \quad . \tag{15}$$

An upwind convection approximation is employed in that same term for the choice of C_V^{n}, in order to ensure numerical stability for moderate cell Peclet numbers. Eqn. (13) is written assuming that the mesh velocities are positive. However, the code can handle arbitrarily signed $\boldsymbol{v}_{mesh}$ within the context of the upwind convection approximation. Because of the implicit upwinding, there is no explicit CFL time constraint where the time step size exceeds the mesh velocity divided by the mesh size.

Up to now, the equations have been independent of the coordinate system, relying just on the implicit formulas for the interface areas, A_i^{n}, and the volumes, V_i^{n}, of the cells. Let's introduce the coordinate system by establishing a hemispheric shell, with initial inner radius of X_{bot}^{0} and outer radius of X_{top}^{0} as the model for the spherical coordinate domain. Then analogously, the cylindrical coordinate system will use a domain consisting of half a circular shell, with inner radius X_{bot}^{0} and outer radius of X_{top}^{0}, with a length in the third direction of *W*. The Cartesian coordinates will use a domain consisting of a square column with sides of length *W*, with the initial *x* positions extending from X_{bot}^{0} to X_{top}^{0}. Then, we may write out the expressions for the volumes and interface areas of the cell boundaries in the three coordinate systems.

Spherical: $$V_i^{n} = \frac{2\pi}{3}\left(\left(I_i^{n}\right)^3 - \left(I_{i-1}^{n}\right)^3\right) \qquad A_i^{n} = 2\pi\left(I_i^{n}\right)^2 \tag{16}$$

Cylindrical: $$V_i^{n} = \frac{\pi W}{2}\left(\left(I_i^{n}\right)^2 - \left(I_{i-1}^{n}\right)^2\right) \qquad A_i^{n} = \pi I_i^{n} W \tag{17}$$

Cartesian: $V_i^n = (W)^2 \left(I_i^n - I_{i-1}^n \right)$ $A_i^n = W^2$ (18)

The implementation of boundary conditions on the top and bottom of the domain will now be addressed. For some problems, a Dirichlet boundary condition on copper vacancies is applied at the bottom of the domain, Eqn. (19), replacing the usual conservation equation on that control volume for that unknown. Also, the coordinate unknown is fixed at the bottom.

$$C_V \left(x = X_{bot} \right) = C_{bot}^0 \; ; \quad X_{bot}^{\,n} = X_{bot}^{\,0} \tag{19}$$

On the top of the domain, we first assume a first order reaction for the injection of copper vacancies leading to the growth of the domain, Eqn. (20).

$$R_s^n = k_1 C_V \left(x = X_{top}^{\,n} \right) \tag{20}$$

The stoichiometry for creation of moles of solid is assumed to be one to one, i.e., one mole of C_V consumed for every mole of solid Cu_2S created. This will later be modified when the parameters and values are refined. The conservation equation for the top control volume, Eqn. (13), is modified to account for the extra reaction loss term:

$$\text{Residual}(C_V, N-1) \mathrel{+}= R_s^n A_i^n \, . \tag{21}$$

The rate of creation of Cu_2S lattice sites on a mol/s basis is given by Eqn. (22).

$$\text{Volume Creation} = R_s^n A_i^n \tag{22}$$

Using C_{Cu2S}, the concentration of Cu_2S lattice sites, which includes both filled and vacant copper sites, an equation for the movement of the top node can then be formulated,

$$C_{Cu2S} A_i^n \left(\frac{X_{top}^{\,n} - X_{top}^{\,n-1}}{\Delta t} \right) = R_s^n A_i^n \quad , \tag{23}$$

completing the specification of an initial time-dependent 1D boundary value problem. Typical numbers of nodes that used thus far vary from 10 to 100. Even for 100 nodes, and thus 200 unknowns, the typical run times for the code are about 10 seconds to grow a large film.

3.1 Coordinate Scaling Study

Initially, to understand the differences between coordinate systems, the unparameterized, nondimensional system will be solved. All reaction rates, diffusion coefficients, and initial and boundary value concentrations will be set to one. Additionally, we will set $X_{bot}^0 = 0$, and $X_{top}^0 = 0.01$. These initial conditions ensure that there will be a kinetically limited regime at early times. Fig. 7 contains the thickness vs. time for the 3 coordinate systems. All coordinate system exhibit the same growth rate for at short times, where mass transport resistance is not a factor. This was expected as the thin film on a spherical shell "looks the same" as a thin film on a flat plate or a cylinder. The spherical coordinate results exhibit the most mass transport resistance at late times. The thickness follows a roughly $L \; \alpha \; t^{1/3}$ trend at late times for the finer mesh. For an

unrefined mesh at longer times, the logarithmic dependence of the thickness vs. time trends upwards. This result is due to the lack of sufficient mesh refinement at late times, where the mesh didn't capture the steep drop-off in C_V that occurs at small radii. The result for the Cartesian coordinate case reproduced the expected $L \propto t^{1/2}$ case, roughly, with only 10 mesh points. The cylindrical coordinate case exhibited an intermediate amount of mass transport resistance between the spherical and Cartesian results with a logarithmic exponent of $L \propto t^{0.45}$.

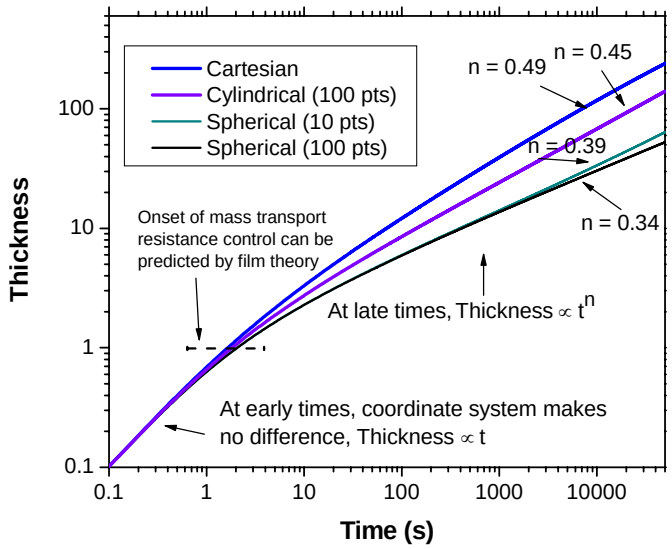

Fig. 7 Differences between coordinate systems for nondimensional growth problem with linear growth kinetics

The transition between kinetic control and mass transport control is well predicted by the "series resistance" model. In that model the process with the largest "resistance" is the rate controlling step. There are two resistances in the problem. The first is the kinetic resistance for the surface reaction at the growth end. The resistance is equal to $k_1 = 1$. The resistance for mass transport, disregarding differences in coordinate systems, is equal to D_V / L, where L is the film thickness. D_V is equal to one. Thus, when $L = 1$, the two resistances are equal and the reaction rate control will switch from one to the other. The transition between kinetic and mass transport control is well predicted for all three coordinate systems by the same simple model.

Thus, to summarize, implementing the model in a spherical coordinate system results in a greater amount of mass transport resistance towards increasing its radius than for a Cartesian coordinate system to increase its height at all times. However, the quantitative differences aren't necessarily that dramatic until the system is well into the mass transport regime. The limiting growth rate behavior is roughly $L \propto t^{1/3}$ for the spherical coordinate system.

3.2 Mass Conservation and the Copper Sulfidation Kinetic Mechanism

In this section the implementation of the boundary conditions will be discussed, and it will be proven that they are mass conserving even under non-dilute conditions where the vacancy concentrations may not be considered infinitely small. As discussed previously, the boundary at $x = X_{top}^{n}$ is moved according to the volumetric increase of Cu_2S produced during surface reaction, Eqn. (23). This is also referred to as the distinguishing condition in Goma's documentation [22,23], and is simply a restatement of Eqn. (23).

$$(\mathbf{n}\bullet\mathbf{v}_{mesh}^{g-s})C_{\mathrm{Cu_2S}} = r_{g-s} \tag{24}$$

n is the outward facing normal to the sulfide domain. $\mathbf{v}_{mesh}^{g-s}$ is the mesh velocity vector at the gas—copper sulfide interface, which we have defined in an earlier section as

$$\boldsymbol{v}_{mesh}^{g-s} = \frac{dX_{top}}{dt},$$

the time derivative of the top mesh point. $C_{\mathrm{Cu_2S}}$ is the molar concentration of the copper sulfide lattice, consisting of both vacancies and regularly filled lattice sites, assumed to be equal to 3.52×10^{-2} mol cm^{-3}, the value for chalcocite. The boundary condition on moving interfaces must also be adjusted in the non-dilute limit. Representing an elemental balance on Sulfur atoms, Eqn. (24) is correct even for moving boundaries. In other words, Eqn. (24) represents the number of lattice units (i.e., Cu_2S molecules) created, and it is exactly equal to the net gas phase reaction rate, since the Sulfur lattice is assumed to be fully occupied. However, an equation which would simply equate the surface reaction rate to twice the bulk diffusive flux of copper vacancies to the surface is incorrect, except in the dilute limit or except when $\boldsymbol{v}_{mesh}$ is zero. To see this, we construct a mass balance on Copper atoms, and we will see that it is equivalent to a mass balance on copper vacancies at the end. Since no copper enters the copper sulfide from the gas phase, there is a balance between the net flux of copper from diffusion (equal to the negative of the copper vacancy flux) and the growth rate of copper in the growing copper sulfide:

$$\mathbf{n}\bullet\left(2\mathbf{v}_{mesh}^{g-s}C_{\mathrm{Cu2S}} - \mathbf{v}_{mesh}^{g-s}C_{\mathrm{V}}\right) = \mathbf{n}\bullet J_{\mathrm{Cu}} = -\mathbf{n}\bullet J_{\mathrm{V}} \tag{25}$$

The second term on the left hand side of Eqn. (25) is due to the fact that not all of the newly created Cu lattice sites are populated with Cu atoms. J_{Cu} and J_{V} are the molar fluxes of copper and copper vacancies, respectively, in the copper sulfide lattice frame of reference due to diffusion. Plugging in Eqn. (24) into Eqn. (25) yields the corrected boundary condition, Eqn. (26).

$$2r_{g-s} = -\mathbf{n}\bullet J_{\mathrm{V}} + \mathbf{n}\bullet\mathbf{v}_{mesh}^{g-s}C_{\mathrm{V}} \tag{26}$$

Eqn. (26) represents the balance on copper vacancies in a moving mesh equation system. The second term in Eqn. (26) represents the creation of copper vacancies in the solid as it grows. Thus, the production of vacancies from the surface reaction is balanced both by the diffusion of the vacancies away from the interface and by the creation of copper sulfide material with copper vacancies in it. The latter term is the "non-dilute term" alluded to at the beginning of the section.

The boundary conditions, , applied at the copper sulfide-gas interface, Eqn. (27), $x = X_{top}(t)$, and the boundary conditions applied at the copper-copper sulfide interface, Eqn. (28) are defined as:

$$x = X_{top}, \qquad \mathbf{n}\bullet J_{\mathrm{V}} = -\nu_{\mathrm{V}}^{g-s} R_{g-s} + \mathbf{n}\bullet\mathbf{v}_{mesh}^{g-s} C_{\mathrm{V}} \tag{27}$$

$$(\mathbf{n}\bullet\mathbf{v}_{mesh}^{g-s}) C_{\mathrm{Cu_2S}} = R_{g-s}$$

$$x = X_{bot}, \qquad \mathbf{n}\bullet J_{\mathrm{V}} = -\nu_{\mathrm{V}}^{s-s} R_{s-s} + \mathbf{n}\bullet\mathbf{v}_{mesh}^{s-s} C_{\mathrm{V}} \tag{28}$$

$$(\mathbf{n}\bullet\mathbf{v}_{mesh}^{s-s}) = 0$$

where ν_V^{g-s} and ν_V^{s-s} are the stoichiometric coefficients for copper vacancies in the surface reactions at either end of the domain, which is two at the gas-solid interface and negative one at the solid-solid interface. R_{g-s} and R_{s-s} are given by Eqn. (1) and Eqn. (2). C_{Cu2S} is the molar concentration of the copper sulfide lattice, consisting of both vacancies and regularly filled lattice sites, assumed to be equal to 3.52×10^{-2} mol cm^{-3}, the value for chalcocite. At $t = 0$, a constant copper vacancy concentration in a small but finite film thickness is assumed. The initial C_{V} value, C_{V}^{o}, and initial film thickness, L^{o}, are designed so that they are not important to the final results. In addition, the $x = 0$ boundary condition set also includes boundary conditions position of the mesh. Because there is no mesh movement on the Cu_2S-Cu interface, the mesh velocity is set to zero.

To include the kinetics into the code, Eqn. (24) is written out to include the rate form for the surface reaction.

$$C_{Cu2S} A_i^n \frac{X_{top}^{\,n} - X_{top}^{\,n-1}}{\Delta t} = A_i^n r_{g-s} = A_i^n \left(k_1 C_{H2S}^{g} - k_{-1} \left(C_V \right)^2 \right). \tag{29}$$

And Eqn.(19) is replaced by the flux expression derived from Eqn. (28), Eqn. (30).

$$-\mathbf{n}\bullet J_V = 2 r_{g-s} A_i^n - \frac{X_{top}^{\,n} - X_{top}^{\,n-1}}{\Delta t} A_i^n C_{\mathrm{V}} \tag{30}$$

Note, the second term in Eqn. (30) cancels out the mesh convection and diffusive flux term in Eqn. (13), leading to a simple result for the C_{V} balance at the top node,

$$\frac{C_{V,top}^{n} V_{top}^{n} - C_{V,top}^{n-1} V_{topi}^{n-1}}{\Delta t} - 2 r_{g-s} A_{top}^{n} - A_{i-1}^{n} F_{Cv,i-1}^{n} + A_{i-1}^{n} \left(\frac{I_{i-1}^{n} - I_{i-1}^{n-1}}{\Delta t} \right) C_{V,i}^{n} = 0. \tag{31}$$

The flux C_{V} through the top domain is given solely by the reaction term and stoichiometric coefficient of C_{V} in the reaction. All mesh motion terms drop out.

3.3 Sample Calculation Using the Copper Sulfidation Model

The copper sulfidation model described in the previous section was exercised on a sample calculation. Below is a listing of the values used in the sample calculation. They comprise the base case. The first set of parameters is kept constant during the parameter study [16].

$$L^0 = 3.0\times10^{-6} \text{ cm}$$
$$X_{bot}^{\,0} = 1.0\times10^{-4} \text{ cm and } X_{bot}^{\,0} = 1.0\times10^{-6} \text{ cm}$$
$$E_1 = 6.30 \text{ kcal mol}^{-1}$$
$$E_{-1} = 6.30 \text{ kcal mol}^{-1}$$
$$A_2 = 9.97 \text{ cm}^4 \text{ mol}^{-1} \text{ s}^{-1}$$
$$E_2 = 0.0 \text{ kcal mol}^{-1}$$
$$C_{Cu2S} = 3.52\times10^{-2} \text{ mol cm}^{-3}$$

The second set is from run conditions, specifically from an experimental run on 9/14/01:

$$X_{H_2S}(g) = 1.41\times10^{-7}$$
$$P = 620 \text{ torr}$$
$$T = 298.15 \text{ K}$$
$$C_{H_2S}(g) = 4.70\times10^{-12} \text{ mol cm}^{-3}$$

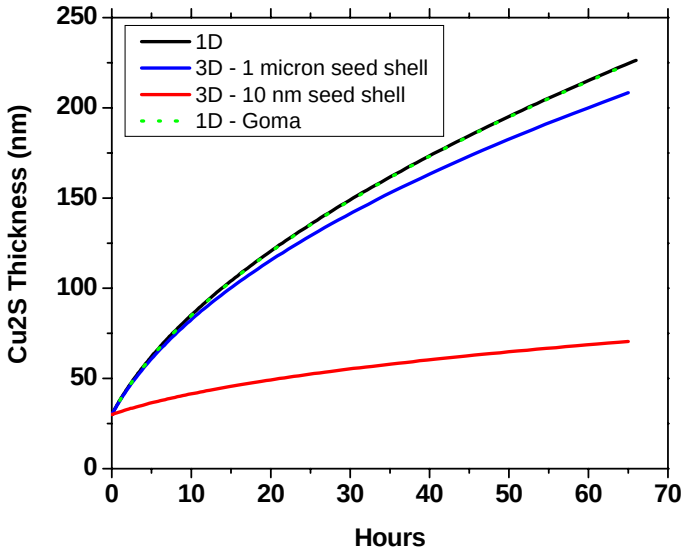

Fig. 8 Effects of the physical coordinate dimensionality on the copper corrosion model. Parameters from the fit to 09/14/01 data with 80% RH. The initial shell thickness was 30 nm in all cases. The Goma 1D model and our model coincided exactly.

The third set of parameters is the result of the fit to the specific experimental data on a run-per-run basis:

$$D_V = 2.85\times10^{-11}\ \text{cm}^{-3}\ \text{mol}^{-1}$$
$$A_1 = 2.71\times10^{5}\ \text{cm}\,\text{s}^{-1}$$
$$A_{-1} = 1.01\times10^{5}\ \text{cm}^{4}\ \text{mol}^{-1}\ \text{s}^{-1}$$

A plot of predicted thickness versus time is presented in Fig. 8 for both `cu2s_1d` and `goma` [23]. `goma` and `cu2s_1d` agree almost exactly for the 1D case demonstrating a verification example for `cu2s_1d`. The development of the equation set within goma, which employs a full ALE formulation, won't be described here, other to say that the equation set is very similar to the equations in Section 3.0.

The curves in Fig. 8 clearly display the original seed shell size, the radius of the inner hemisphere that makes up the initial domain, as being a defining parameter for the problem. If the seed shell size is significantly smaller than the final Cu_2S film thickness, and if growth is in the diffusion controlled regime, then the growth rate will have a spherical $L \propto t^{1/3}$ dependence (red curve in Fig. 8). However, if the initial seed size is of the same magnitude as the film thickness, then the behavior will resemble the Cartesian coordinate case with $L \propto t^{1/2}$ (blue curve in Fig. 8). Note that the direction of reactant diffusion has been reversed in this model in comparison to other models. The fact that the copper vacancies are diffusing into the original seed shell from their creation point on the gas copper-sulfide surface does not change the behavior.

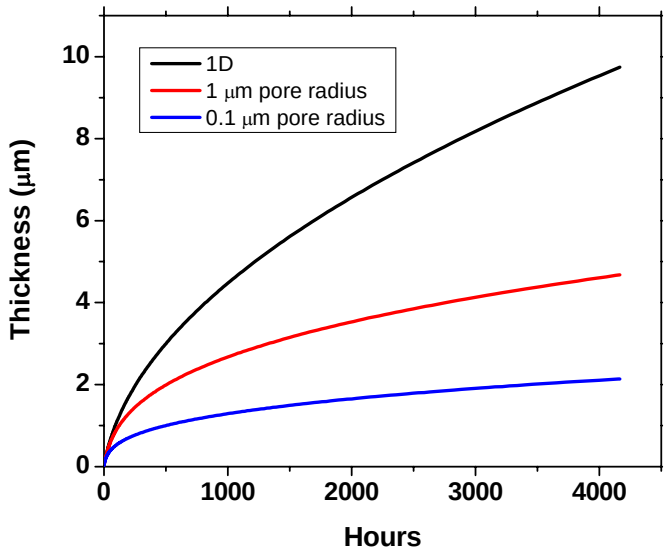

Fig. 9 Effects of the coordinate system on the copper corrosion model. 1D is in Cartesian coordinates. The red and blue curves are in spherical coordinates with differing inner shell sizes. Parameters from the fit to 08/31/01 data with 0.5% RH.

Even if diffusion is not the rate limiting process, the spherical geometry may have an effect. Two kinetic rate constants may be rate controlling: the reaction at the gas-copper-sulfide interface, and the reaction at the interface between copper sulfide and copper. The spherical geometry affects the relative area-averaged rates of these two reactions. The total flux is multiplied by the interfacial area where the reaction is taking place. For example, if the seed shell radius is 1 μm and the eventual final radius is 10 μm, then the relative kinetic resistance of R_{s-s} will be 100 times greater for the spherical case than for the Cartesian case due to the area effect.

This may increase the importance of the R_{s-s} reaction rate constant for the spherical case while it remains unimportant in the Cartesian case, a troubling point since the values for the two rates in the CS model were fit from experimental data which couldn't significantly distinguish between the two rates.

Lower relative humidity data were also modeled in 1D and 3D. Fig. 9 contains thickness results from using the fits to 08/31/01 data at 0.5% relative humidity [19]. Note the change in scale of the time and thickness axes. Generally, the onset of Stage II behavior is delayed at low relative humidities. However, once Stage II behavior has started, the effects of the physical coordinates are much the same as in the high RH case.

3.4 Inherent Model Characteristics

Based on the above set of reaction and diffusion equations, we can deduce certain characteristics of the growth behavior before presenting the numerical results.

A quasi-equilibrium is attainable on the gas-solid interface when the forward and reverse reaction rates in Eqn. (1) become equal.

$$R_{g-s} \cong 0, \quad C_{\mathrm{V}}^{equil} = \left[\frac{A_1}{A_{-1}} \exp\left(\frac{-(E_1 - E_{-1})}{RT} \right) C_{\mathrm{H_2S}}(g) \right]^{\frac{1}{2}} \tag{32}$$

Physically, the quasi-equilibrium condition represented by Eqn. (32) will be approached when downstream rate processes are slower than the initial reaction at the gas surface. One way for this to occur is if the diffusion of copper vacancies through the product copper sulfide layer is rate limiting; in the current models, we have identified this condition as Stage II growth, where the growth rate becomes sub-linear in the time coordinate. The quasi-equilibrium concentration in Eqn. (16) is dependent upon the square-root of $C_{\mathrm{H2S}}(g)$. Thus, the overall growth rate in Stage II predicted by this model is also sub-linear in $C_{\mathrm{H2S}}(g)$; in Stage I, it's linear, however. Experiments on this system have never unearthed a nonlinear $C_{\mathrm{H2S}}(g)$ dependence in any stage to our knowledge. However, much of the experimental work has been focused on Stage I, with many of the experiments having fixed the inlet $C_{\mathrm{H2S}}(g)$ concentration or at least restricted the range of $C_{\mathrm{H2S}}(g)$ to a factor of 2 or so. Experiments on Stage II, employing wide variations in $C_{\mathrm{H2S}}(g)$, focused on understanding the order dependence of in $C_{\mathrm{H2S}}(g)$, have not been done. More discussions on how to analyze the Stage I to Stage II transition given the current model will be given in the next section.

The current copper sulfidation model presented here has a total of three rate processes in series: reaction at the copper-copper sulfide interface, diffusion through the copper sulfide, and reaction at the copper sulfide-gas interface. They can be analyzed via a series resistance approach to determine what is the rate-controlling step [24]. Assuming a pseudo steady-state for all three processes, the rate of all three processes will be the same. The overall rate constant can be written as the inverse sum of linearized rate constant from each step, or referred to as "conductance". The rate-limiting process will then have the smallest relative value for conductance. For example, diffusional processes have conductances equal to the diffusion coefficient divided by the layer thickness. Interfacial reactions have conductances equal to their linearized rate constants on the side of the interface pertinent to the diffusional process.

A sample calculation of conductance, the relative flux resistance per area (with units of cm s^{-1}), for our model follows. $L = 6.6\times10^{-6}$ cm, $t = 597600$ s, $C_V = 1.56\times10^{-7}$ mol cm^{-3} at the copper sulfide-gas boundary, and $C_V = 1.44\times10^{-7}$ mol cm^{-3} at the copper—copper sulfide boundary, $A_1 = 1.05\times10^{3}$ cm s^{-1}, $E_1 = 6.45$ kcal mol^{-1}, $A_{-1} = 1.88\times10^{3}$ cm^4 mol^{-1} s^{-1}, $E_{-1} = 6.30$ kcal mol^{-1}, $D_V = 1.11\times10^{-10}$ cm^{-3} mol^{-1}, $A_2 = 9.97$ cm^4 mol^{-1} s^{-1}, $E_2 = 0.0$ kcal mol^{-1}, $C_{H_2S}(g) = 5.36\times10^{-12}$ mol cm^{-3}.

Copper-copper sulfide interface reaction:

$$\text{Rate} = k_2 C_{V_V}^2 = 9.97(1.44\times10^{-7})^2 = 2.067\times10^{-13} \text{ mol cm}^{-2}\text{ s}^{-1}$$

$$\text{Conductance} = 2k_2 C_V = 2.88\times10^{-6} \text{ cm s}^{-1}$$

Diffusion through the copper sulfide film:

$$\text{Rate} = \frac{D_V \Delta C_V}{L} = 1.11\times10^{-10}\,\frac{(1.56\times10^{-7} - 1.44\times10^{-7})}{6.6\times10^{-6}} = 2.02\times10^{-13} \text{ mol cm}^{-2}\text{ s}^{-1}$$

$$\text{Conductance} = \frac{D_V}{L} = 1.6\times10^{-5} \text{cm s}^{-1}$$

Copper sulfide—gas interface reaction:

$$\text{Rate} = 2\left(\begin{array}{l} 1.04\times10^{3}\exp\left[\dfrac{-6.45\times10^{3}}{RT}\right]5.36\times10^{-12} \\ -\left(1.88\times10^{3}\right)\exp\left[\dfrac{-6.3\times10^{3}}{RT}\right]\left(1.56\times10^{-7}\right)^2 \end{array}\right) = 1.90\times10^{-13} - 1.09\times10^{-15} \text{mol cm}^{-2}\text{ s}^{-1}$$

$$\text{Conductance} = 2A_{-1}\exp\left[\frac{E_{a,-1}}{RT}\right]C_V = 1.44\times10^{-8} \text{cm s}^{-1}$$

The fact that we get all of the rates for the subprocesses to be the same means we are doing the analysis correctly. The key to this analysis is in the relative values of the conductances for the subprocesses.

For this particular set of rate constants and physical conditions, it turns out that the initial surface reaction is rate-limiting. Thus, everything else in the problem is less relevant. The growth rate can be modeled via the forward direction of the copper sulfide-gas surface reaction. This feature also explains why the concentration of vacancies in the film is lower than the equilibrium concentration under these conditions, $C_V^{equil} = 1.53 \times 10^{-6}$ mol cm^{-3}. The initial reaction is so slow that copper vacancies are removed from the surface quickly through diffusion, hence lower concentration of C_v is expected. Of course, the good news is that this regime of the mechanism will exhibit linearity with respect to the H_2S concentration, as the forward reaction is linear in H_2S concentration.

3.5 Copper Sulfidation Data from the Stagnation Point Flow Reactor

The most recent data collected for copper sulfidation involves copper sulfidation measurements in a stagnation-point flow reactor. Since a detailed analysis of the reactor design and flow characteristics is described in a previous analysis that focused on the gas-phase mass transport in the stagnation-point flow sulfidation reactor, the readers are referred to that reference for details of the experimental set up [16].

Three sets of experimental data differing in the relative humidity (RH) value are used for parameter estimation runs: 0.5% RH, 20% RH, and 80% RH. In each experiment, copper sulfide film thickness, inferred by the amount of H_2S consumed in the reactor, is recorded as a function of time. The film thickness curves are plotted for each RH set in Fig. 10 to Fig. 12. Most of these curves are marked initially by a linear-in-time sulfidation rate, then transition into a slower sulfidation rate regime at later times which is sublinear-in-time. The linear-in-time regime is referred to as the Stage I growth while the sublinear-in-time growth rate regime is referred to as Stage II growth. The current constitutive model assumes that the Stage I growth is rate-limited by the forward reaction rate in Eqn. (1). The model then assumes that the Stage II growth is rate-limited by the diffusion of copper vacancies through the product copper sulfide layer. All of the experiments are carried out at an inlet mole fraction of H_2S near 150 ppb in the feed stream at 25^{o}C with a constant total flow rate of air of 1000 sccm.

The amount of scatter in the 0.5% relative humidity (RH) data in Fig. 10 is striking. To this date, there has been no explanation as to why there is much scatter in the data. The two runs carried out in the month of April, 2002, have much slower linear growth period than the ones carried out in 2001. The “08-14-01” run has similar Stage I behavior as the “08-31-01” experiment, but the transition to Stage II occurs at a much earlier time. In Fig. 11, the data for 20% also show different behavior between the two experiments. The “10-25-01” data follow a very linear growth rate during most of the experiment. The “08-22-01” data show faster initial growth rate and faster transition to Stage II growth (around 25 hours). In Fig. 12, both of 80% data show more consistency, but unfortunately the experiment carried out in March, 2002 stopped at 23 hours. Based on previous experiments that were done with different reactor design, Braithwaite and coworkers [11] made the following observations.

Stage I linear growth rate increases with relative humidity.

Stage I to Stage II transition occurs at a smaller sulfide thickness with higher relative humidity.

While inconsistencies in the data from the stagnation reactor are observed, these two characteristics seem to hold on average. Based on the most recent data, we have proceeded to estimate A_1, A_{-1}, and D_v.

Note some of the data exhibit a "nucleation stage," i.e., a delay before Stage I growth rate proceeds. The increase in the nucleation delay time has in the past been correlated with decreasing RH values [16]. This delay does seem to hold in the data of Fig. 10 to Fig. 12. A constitutive model for this feature was not included in the bare coupon numerical model, but has been included in the plated copper numerical model where the exposed Cu_2S surface area is much diminished and exists in isolated locations.

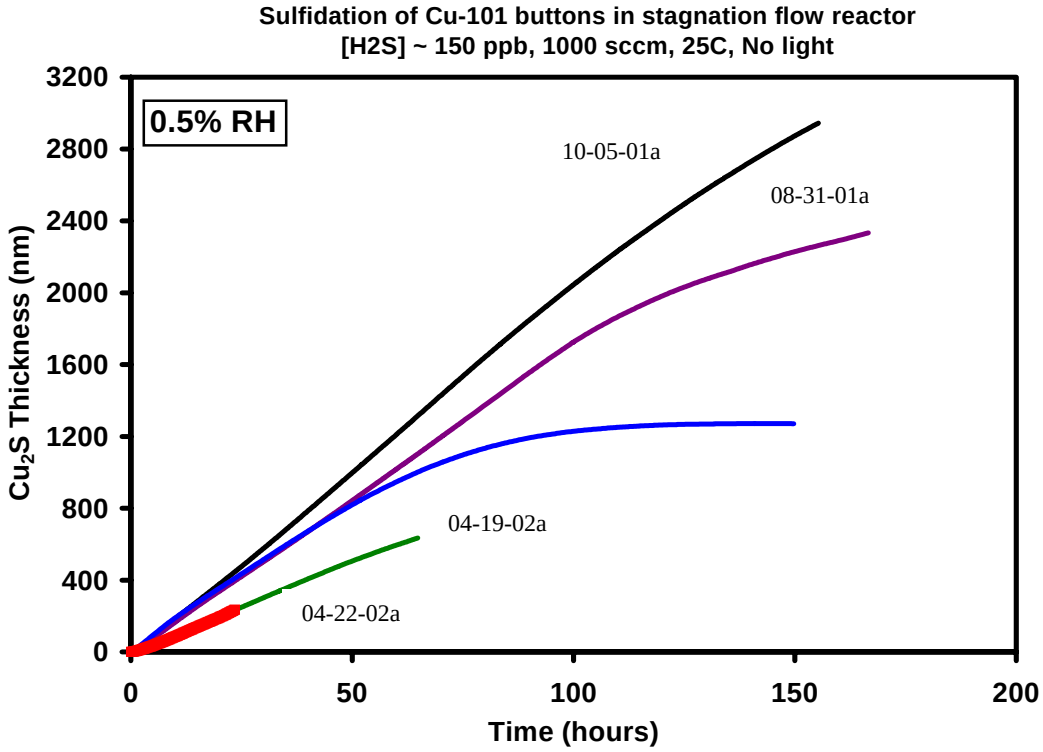

Fig. 10 Copper sulfidation data at 0.5% RH.

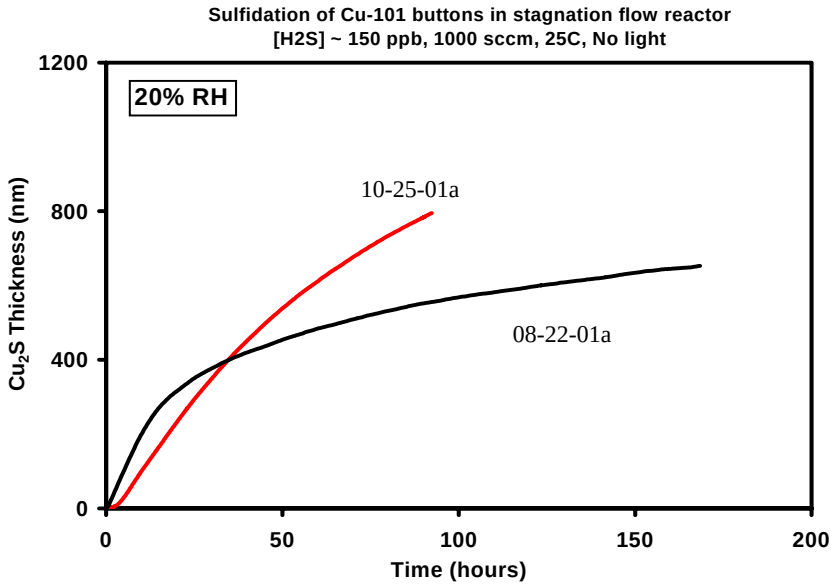

Fig. 11 Copper Sulfidation data at 20% RH

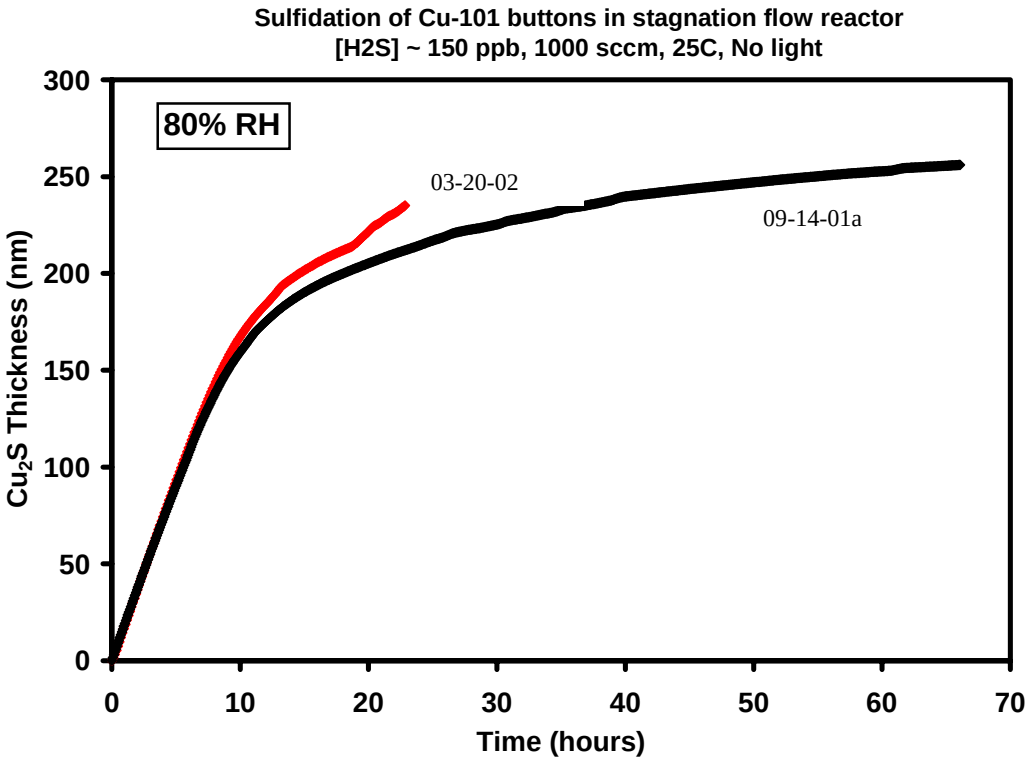

Fig. 12 Copper sulfidation data at 80% RH.

As mentioned before, the equations are set up and solved using the finite-element program GOMA. Successful interface between DAKOTA and GOMA for optimizations has been

demonstrated and documented previously, and the readers are referred to these documents for more details [25, 26].

The parameter estimation problem entails minimizing an objective function representing the difference between model predictions and experimental data. For this study, two different types of objective functions, $\Phi_{normalized}$ and $\Phi_{absolute}$, are used depending on the nature of the data.

$$\Phi_{normalized} = \sqrt{\sum_{i=0}^{ntime} w_i \frac{(h_i^{\exp} - h_i^{GOMA})^2}{(h_i^{GOMA})^2}} \tag{33}$$

$$\Phi_{absolute} = \sqrt{\sum_{i=0}^{ntime} w_i (h_i^{\exp} - h_i^{GOMA})^2} \tag{34}$$

h_i^{exp} are the experimentally measured Cu_2S thicknesses whereas the h_i^{GOMA} are the predicted Cu_2S thicknesses. w_i are weighting factors with which the data-to-model discrepancy may be weighted differently during Stage I vs. Stage II growth. The sampling time interval is hourly for both the data and the model.

Table 1 lists the values of non-fitted parameters in the constitutive model. The activation energies and pre-exponential factors listed in the table do not vary during the optimization runs; only A_1, A_{-1}, and D_v were fit. As discussed earlier, the same initial vacancy concentration and initial film thickness are used for all GOMA simulations.

Table-1 Values of Preset Constants

Relative Humidity & Experiment Date	Average C_{H2S} in the exit stream* (in ppb and mol cm^{-3})	T_{max} (hr)	Other constants
0.5% 08-14-01	177.0 ppb $6.150e^{-12}$ mol cm^{-3}	149	E_1 = 6300 cal mol^{-1} E_{-1} = 6300 calmol^{-1} A_2 = 9.97 $cm^4 mol^{-1} s^{-1}$ Temperature = 298K $C_v^0 = 1.523e^{-8}$ mol cm^{-3} $L^0=3.0e^{-4}$ cm
0.5% 08-31-01	129.4 ppb $4.496e^{-12}$ mol cm^{-3}	166	
0.5% 10-05-01	151.0 ppb $5.247e^{-12}$ mol cm^{-3}	339	
0.5% 04-19-02	144.0 ppb $5.003e^{-12}$ mol cm^{-3}	64	
0.5% 04-22-02	147.6 ppb $5.129e^{-12}$ mol cm^{-3}	23	
20% 01-25-01	182 ppb $6.11518e^{-12}$ mol cm^{-3}	90	
20% 08-22-01	214 ppb $7.178e^{-12}$ mol/cm^3	168	
80% 09-14-01	140 ppb $4.696e^{-12}$ mol/cm^3	66	
80% 03-20-02	117 ppb $3.924e^{-12}$ mol/cm^3	22	

*It was tested earlier that the parameter estimation problem was insensitive to including variations in H_2S concentration during each run.

Because film thickness is inferred by exit concentration of hydrogen sulfide, C_{H2S}(g), is known to vary throughout the experiment. Fig. 13 shows the recorded hydrogen sulfide concentration for 0.5% RH and 08/31/01 experiment. We have suspected that the transient variation will impact the goodness of the data fit; hence, several initial optimization runs (results not shown here) are

carried out with time-varying $C_{H2S}(g)$ (fitted to the data by a sixth-order polynomial, see Fig. 11). No improvement to the fit is observed, however. Hence, only an average H_2S concentration from all of the recorded values is used in all of subsequent optimization runs.

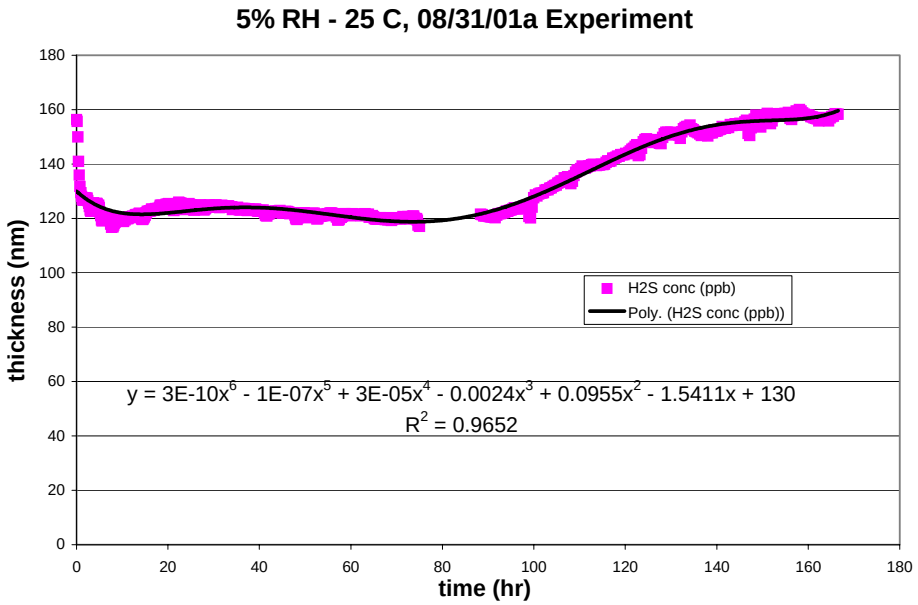

Fig. 13 Hydrogen Sulfide exit concentration for 0.5% RH, 08-31-01 experiment

Table-2 Initial and Final Values of the Fitted Parameters

RH	Expt Date	ln (A_1) – (cm/sec)		ln (A_{-1}) (cm^4/mol sec)		ln (D_V) (cm^2/sec)		Legend
		initial	final	initial	final	initial	final	
80%	3/20/2002	12.00	12.38	12.00	11.66	-25.00	-22.94	
	9/14/2001	18.00	16.89	8.00	12.87	-25.00	-26.01	091401fit_1
		12.00	12.51	12.00	11.53	-25.00	-24.28	091401fit_2
20%	10/25/2001	11.00	11.36	10.00	9.81	-23.50	-22.90	
	8/22/2001	12.00	13.05	12.00	11.00	-25.00	-24.45	082201fit_1
		20.00	18.85	11.00	11.99	-27.00	-27.00	082201fit_2
0.50%	4/19/2002	11.49	10.76	8.20	8.27	-23.00	-22.60	
	4/22/2002	11.49	10.64	8.20	8.25	-23.00	-23.33	042202fit_1
		8.00	10.50	10.00	9.76	-15.00	-15.00	042202fit_2
	8/14/2001	15.00	11.46	9	10.25	-20.00	-21.54	081401fit_1
		15.	10.55	10.25	7.62	-15.00	-15.52	081401fit_2
	10/5/2001	11.49	11.88	8.20	8.07	-23.00	-21.94	100501fit_1
	8/31/2001	8.00	11.88	8.50	8.36	-23.00	-22.26	

Table 2 lists the starting and converged values of the fitting parameters. Note that different sets of initial values are used on several data sets to check for other local optima. The values of parameters in the optimization have been rescaled as natural logarithms of the absolute parameter values to cover large orders of magnitude in parameter space.

Even though some of the final parameter values seem close to their initial guesses, the absolute value differences are larger, since these reported constants are exponents.

Fig. 14 shows the fit between the data and the model for 80% RH experiments. The results show poor fits in the linear regime for the 3/20/02 data and for the 9/14/02 data. The 3/20/02 and 9/14/02 data shows a quick transition to Stage II, and the model cannot predict similar behavior. Also, since the latter points are weighed more heavily in the objective function for these optimizations, the fit is particularly poor in the linear regime. This indicates that the model is lacking the necessary phenomenology which requires a fast transition from Stage I to Stage II. We have previously indicated that our expectation is that the bulk diffusional resistance model we are employing can only marginally capture the diffusion-across-grain-boundary mechanism experimentally discovered to be the rate limiting step. The lack of agreement displayed in Fig. 14 is an indicator of the errors involved in our engineering-level model. As indicated in Table 2, while the "091401fit_1" parameters have much higher A1 and A-1 and lower DV values, the fit to the data is essentially unchanged when comparing to the fit with "091401fit_2" parameters. This indicates a correlation between $A1$ and DV values.

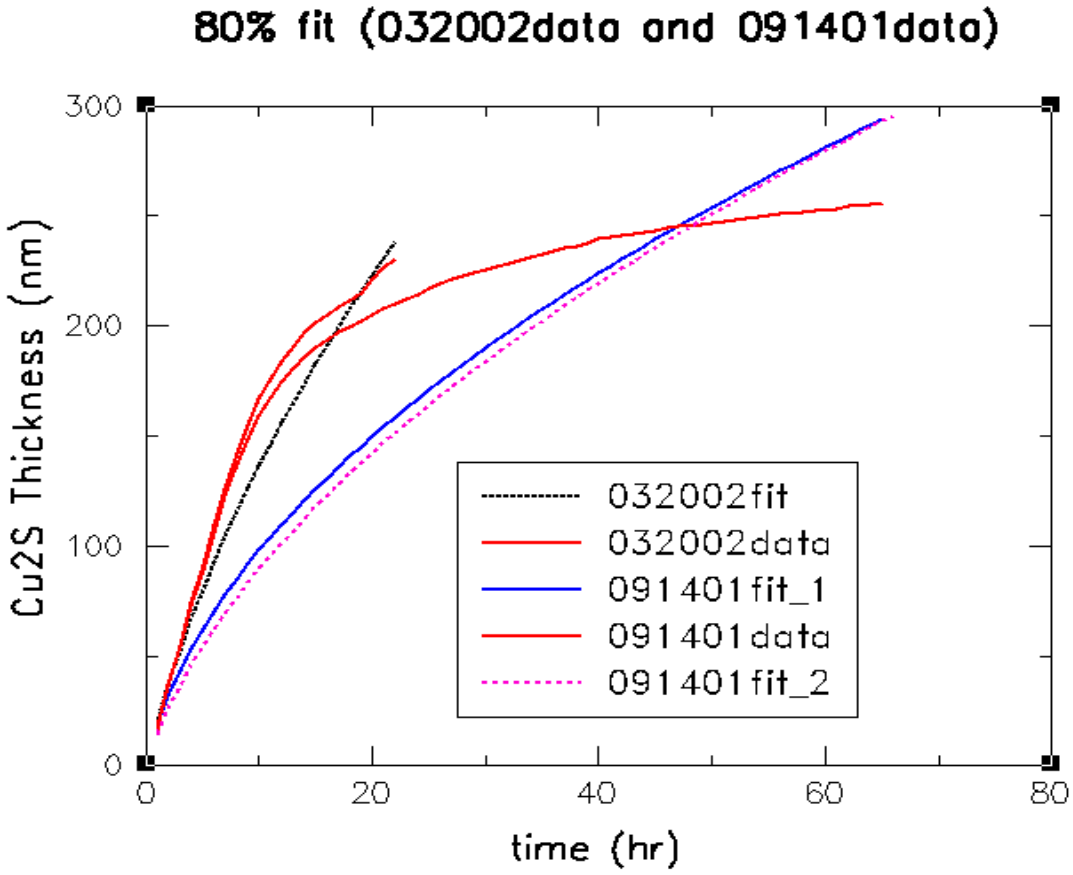

Fig. 14 80%RH data and model predictions based on fitted parameters.

Fig. 15 shows the fit between the data and the model for 20% RH data. The fit is excellent for the 10/25/01 experiment but poor for the 08/22/01 experiment. Compared to the 10/25/01 results, the 08/22/01 fit exhibits slower linear growth in order to match a faster transition from Stage I to Stage II. Again, the "082201fit_1" and "082201fit_2" fitted parameters were very different yet produced very similar growth behavior, indicating highly correlated A1 and DV values.

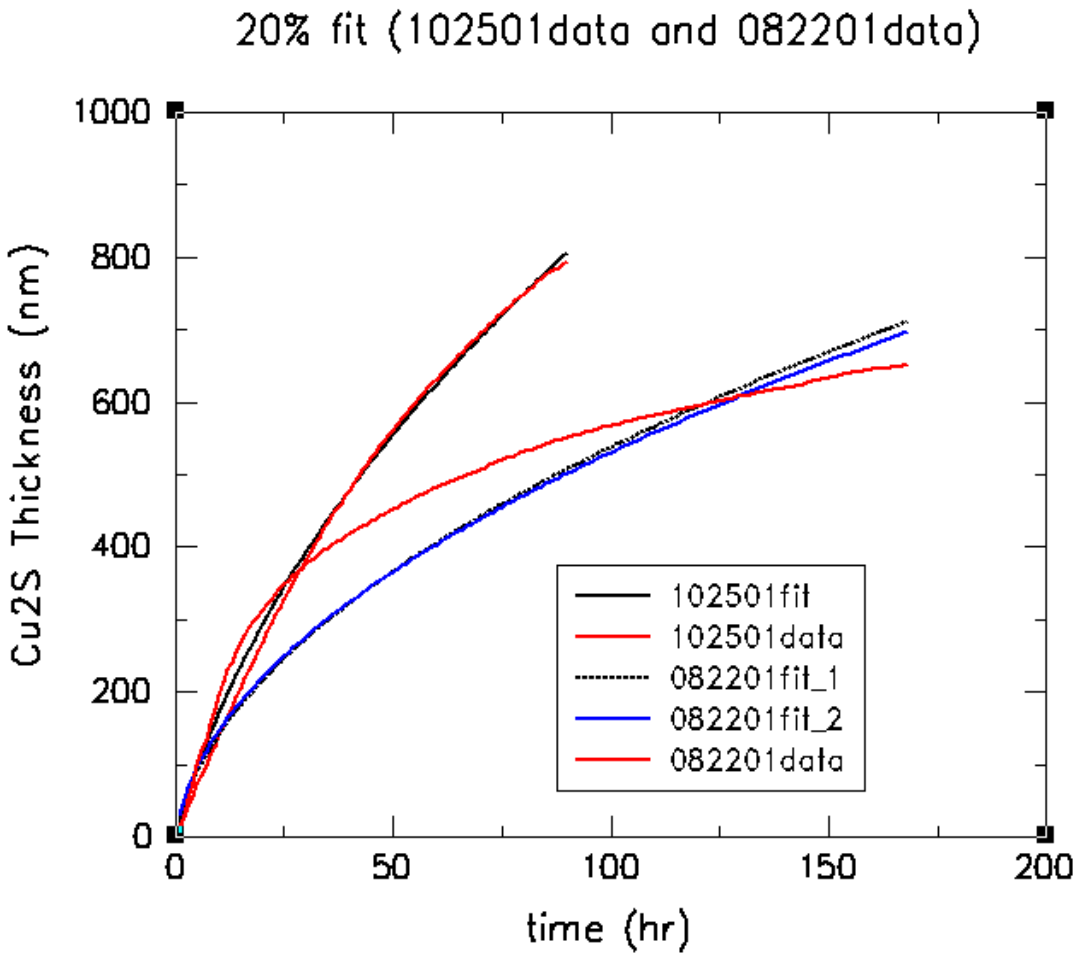

Fig. 15 20% RH data and model predictions based on fitted parameters.

Fig. 16 through Fig. 20 show the results of 0.5% RH data fit. The success of the fit is again mixed, depending on the data. The model predictions for all of experiments, with the exception of 04/22/02 and 08/14/01 data, show reasonable agreement with the data. Two model prediction curves are given for 04/22/02 data based on two sets of parameters: 042202fit_1 and 042202fit_2. Despite the similarity between two growth curves, these two sets of parameters have diffusivity values differing by four orders of magnitude (7.4×10^{-11} cm^2 s^{-1} in 042202fit_1 and 3.06×10^{-7} cm^2 s^{-1} for 042202fit_2). Since the experiment is carried out for less than 30 hours, the data is most likely a response of Stage I growth. Hence, the sensitivity of the layer thickness to diffusivity is quite small.

The data collected at 08/14/01 exhibit a fast transition into Stage II growth, and again, there is no unique set of parameters that can reasonably fit both regimes very well. The diffusivity for 081401fit_2 is three orders of magnitude higher than 081401fit_1 while the forward kinetics is three times smaller. When D081401fit_2 >> D081401fit_1, C_V will increase faster at the gas-solid interface and thus increase the reverse kinetics rate in Eqn. (1). This causes a poor fit in the Stage I growth curve.

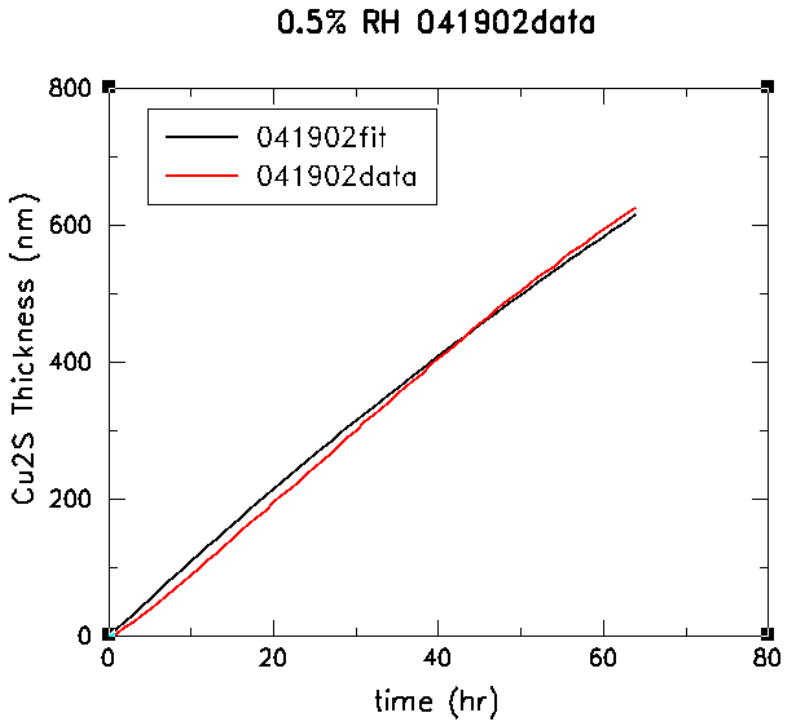

Fig. 16 04/19/02 experiment and model predictions.

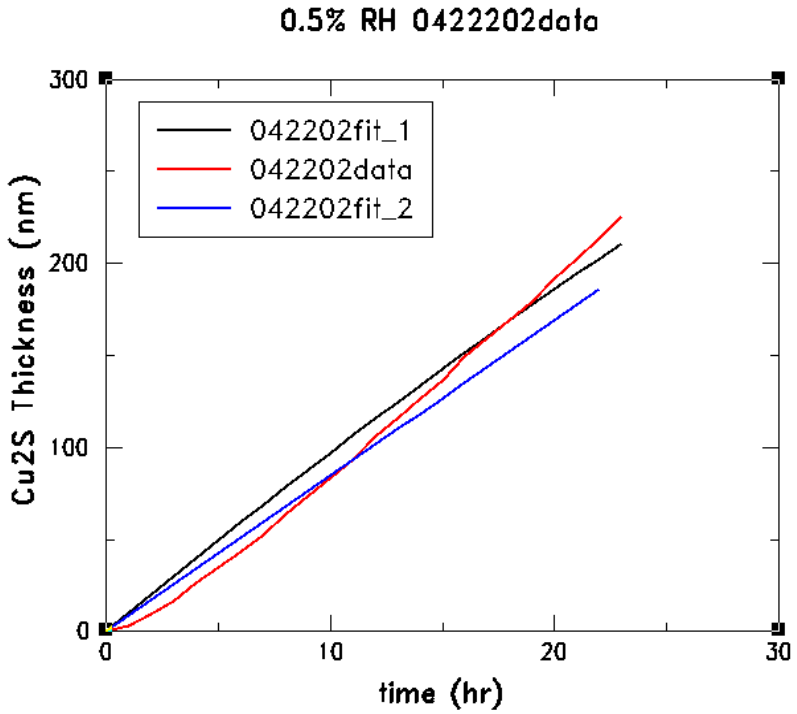

Fig. 17 04/22/02 experiment and model predictions.

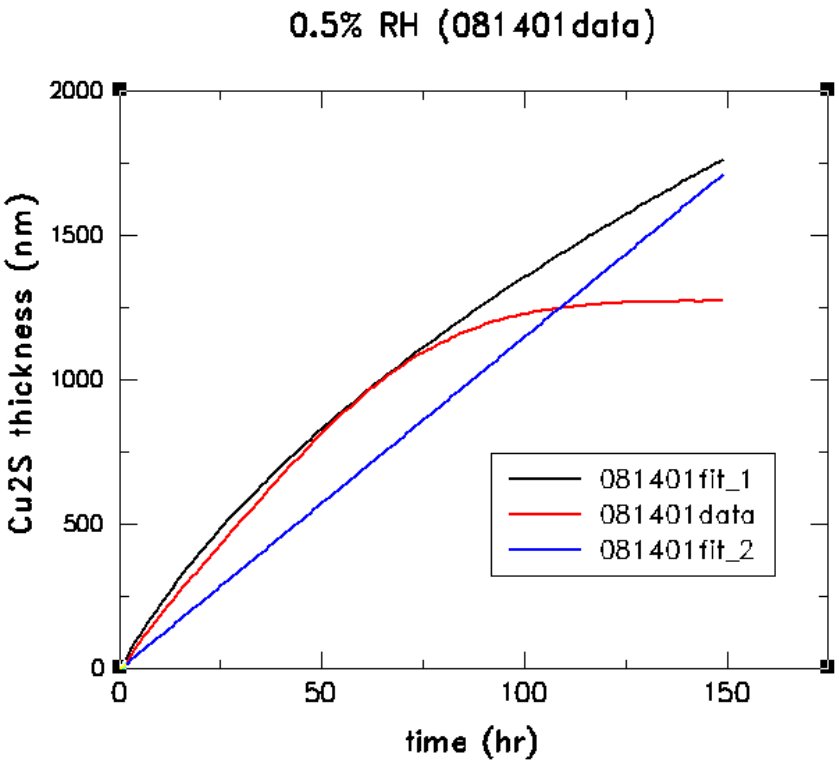

Fig. 18 08/14/01 experiment and model predictions

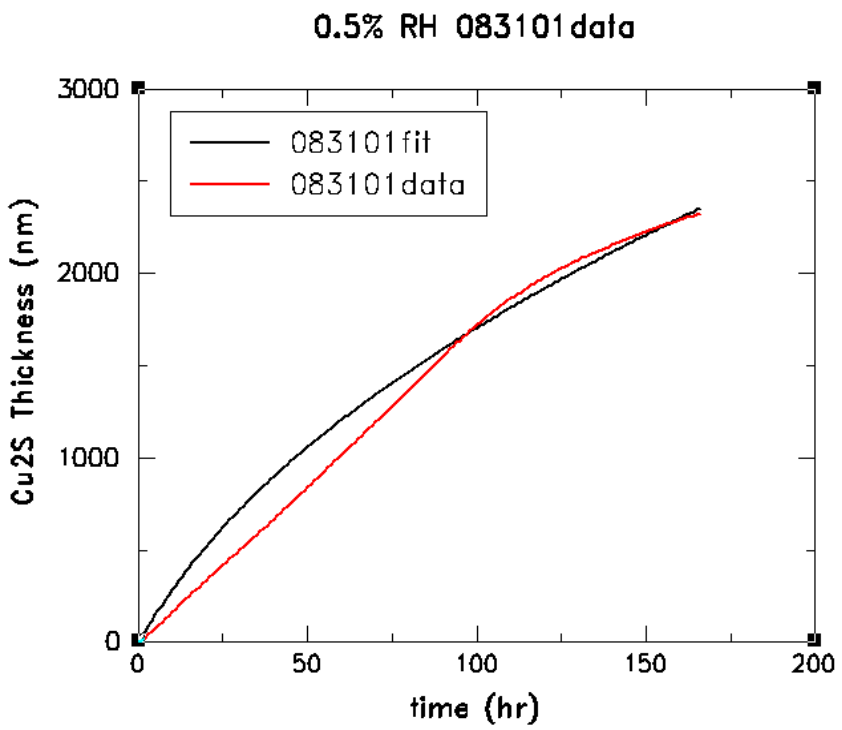

Fig. 19 08/31/01 experiment and model predictions

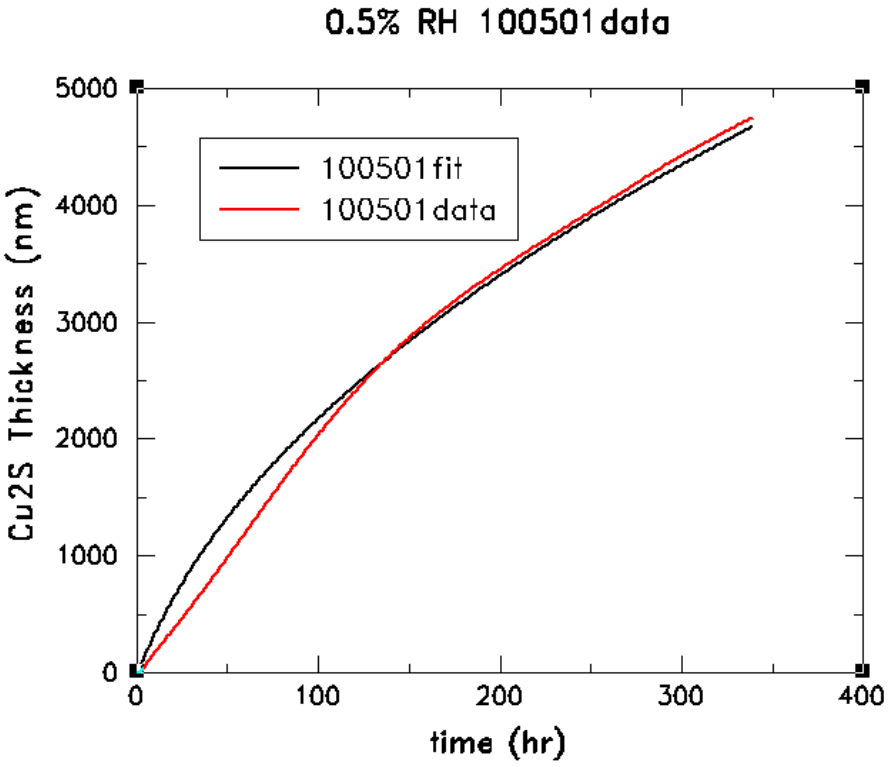

Fig. 20 10/05/01 experiment and model predictions

3.5.1 Discussion

When this work initially began, only two sets of data were used for parameter estimation: the data from 08/31/01 (0.5%) and from 10/25/01 (20%). It was quickly recognized that the current kinetics model cannot predict the transition from Stage I to Stage II growth. Attempts were made to modify the model by including a mass transfer resistance in the gas phase, but improvements in fits were not observed in both sets of data.

While the improvements in fit are seen using a different weighing function for both sets of data, the same weighting function cannot apply to all of data sets. The choice of weighting function is rather arbitrary and not automatic.

Different optimization schemes are also tested to check for opportunities of finding a better optimal solution. Nevertheless, the experiences we have with gradient-based DOT_BFGS or NOSOL_SQP and non-gradient-based PATTERN_SEARCH algorithms are similar. The intervals that each optimizer searches are usually very close to the initial point, despite a fairly wide upper and lower bound specifications as well as varying finite-difference interval size.

By expanding the experimental data sets to include other observations, the goal is to understand the scatter in the parameters. Table 3 lists the minimum and maximum values of each parameter. The forward reaction rate spans four orders of magnitude while the diffusivity spans five orders of magnitude. As mentioned before, the two parameters can offset each other and still yield very similar model predictions. Based on this observation, one may speculate that this deterministic model may not be suitable for modeling the copper sulfidation growth.

Table 3- Minimum and maximum parameter values for all of data sets.

	$\ln(A_1)$	A_1	$\ln(A_{-1})$	A_{-1}	$\ln(D_v)$	D_v
minimum	10.5	3.63E+04	7.62	2.04E+03	-27	1.87953E-12
maximum	18.85	1.54E+08	12.87	3.88E+05	-15	3.05902E-07

Diffusivity of vacancies in this model is assumed constant and is characteristics of molecular random walks. If molecular vacancy transport is a purely diffusion-driven process, one can roughly estimate the time it takes for traveling over Δh distance.

$$D_v \approx \frac{\Delta h^2}{\Delta t}$$
$$\log(\Delta h) \approx 0.5\log(D_v) + 0.5\log(\Delta t) \tag{35}$$

Fig. 21 and Fig. 22 show the log-log plots of experimental data from 10/25/01 at 20% RH and from 08/14/01 at 0.5% respectively. The curves in these experiments exhibit fast transitions from Stage I to II. Power law fits to the experimental data in the two regions are also shown on the plots. The slopes from both curves change from 1.24 to 0.34 for the 10/25/01 data as the curve shifts from Stage I to Stage II. Relative to a purely diffusion-driven dynamics, the slope in Stage I period indicates fast dynamics which cannot be

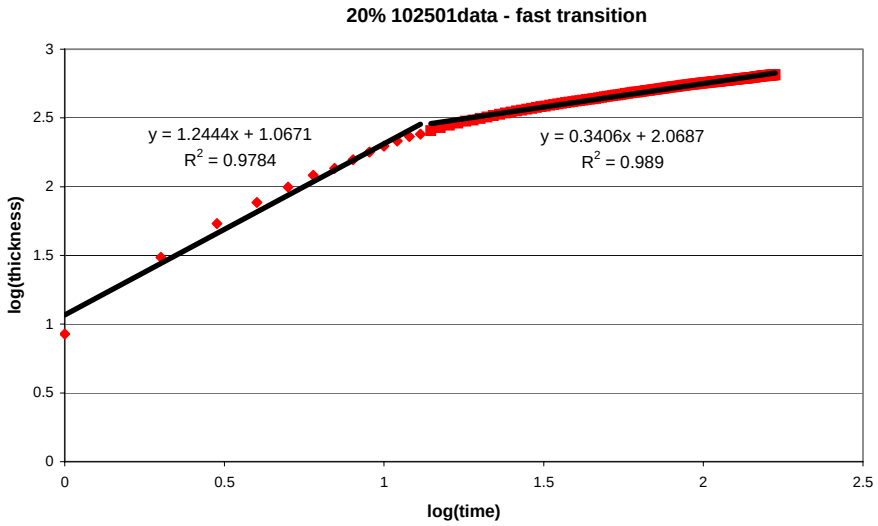

Fig. 21 Log-log plot of 10/25/01 data

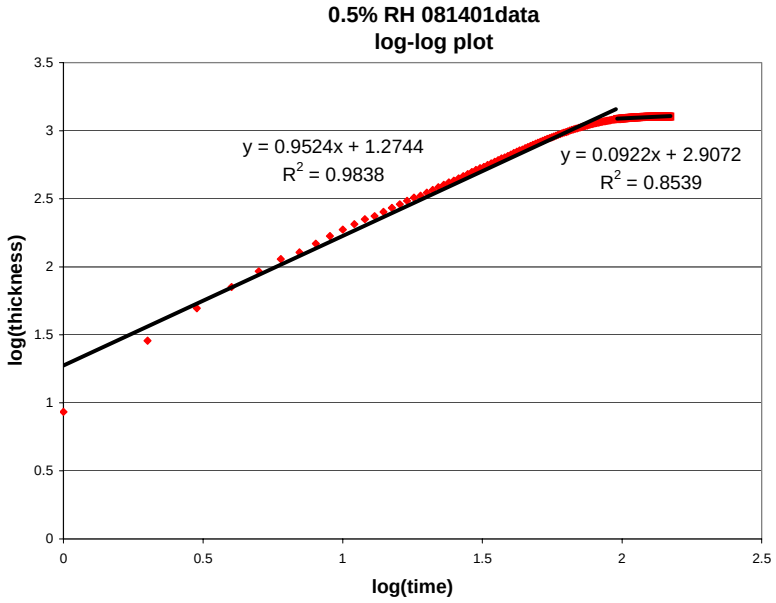

Fig. 22 Log-log plot of 08/14/01 data

modeled with a purely diffusion process. The time dependence in the Stage II growth exhibits a lower power law dependence on time that what diffusion rate-limited growth would yield, 0.5. A similar trend is observed in the 08/14/01 data, where the power law slope changes from 0.95 to 0.09 as growth goes from Stage I to Stage II.

Because Stage I and Stage II corrosions differ in film morphology, one may suspect a change in growth mechanism due to a change in morphology. The current model cannot capture the Stage II growth. One possible modification to the current model is creation of concentration-dependent diffusivity. Concentration-dependent diffusivity is observed in liquid phase polymer-

solvent systems where the diffusivity of solvent species is hindered by the presence of polymeric matrix (the so-called free volume effect) [29]. While corrosion chemistry is vastly different from that of polymer chemistry, one cannot rule out the possibility of such an association. Other than testing a concentration-dependent diffusivity, we may also consider a more complex interfacial chemistry between gas and copper sulfide by including dynamics within the aqueous surface layer.

3.5.2 Summary of Fits and Comparison of Results to Other Sandia-Generated Models

Table 4 provides a comparison between the parameters in the copper sulfidation models that have been generated/proposed recently at Sandia. For the current data study, we used the fits for one data set. The current model found a great deal of autocorrelation amongst between the model parameters. In other words, the data didn't help distinguish between sets of parameters very well. We think this is important. However, for the purposes of comparison to the other models, we've just shown one result from 10/25/01 at 20% RH.

Table 4 - Comparison of Parameters Between Models

Parameter	Current Model (10/25/01)	Larson [3]	Braithwaite [28]	Moffat [16]
k_1 (cm s^{-1})	2.06	1.21	3.1	10.8
D_V (cm^2 s^{-1})	1.13×10^{-10}	1.0×10^{-10}	3.0×10^{-8} to 1.0×10^{-9}	NA
k_{-1} (cm^4 mol^{-1} s^{-1})	0.437	0.16 [a]	0.086	NA
C_V^{equil} (mol cm^{-3}) [b]	5.33×10^{-6}	6.84×10^{-6}	1.49×10^{-5}	NA
k_2(cm^4 mol^{-1} s^{-1})	9.97	10.0	10	NA

[a] quartic rates converted to quadratic rates by multiplying by the square of C_V^{equil}.

[b] C_V^{equil} evaluated at a nominal value of 150 ppb H_2S, 640 torr, 25C

There is a lot of inbreeding between the models, so their apparent agreement should come as no surprise. However, it should be noted that this model, Larson [3], and Moffat [16] all used different experiment data, and all got about the same result, at least for some experimental runs. This study again makes the point that there is great variability/scatter in some of the experimental runs.

Let us calculate a representative sticking coefficient for the forward reaction rate constant, r_{g-s}. We will pick the 0.5% RH data run named 10-05-01a, whose data is presented in

Fig. 20. 150 ppb H_2S at 640 torr and 25 C corresponds to 6.40×10^{-12} mol cm^{-3} H_2S. The values in Table 1 lead to a rate constant of

$$k_1^* = \exp(11.88)\exp\left[\frac{-6.3\times10^3}{(1.987)(298)}\right] = 3.46\ \text{cm s}^{-1}\ .$$

The effusive flux rate of H_2S molecules under 25ºC conditions is $1.08\times10^4\ \text{cm s}^{-1}$ [16]. Thus, the sticking coefficient is equal to 3.2×10^{-4} under these conditions. A previous analysis focusing on mass transport in the gas phase had determined that the sticking coefficient for the copper sulfidation reaction was 1.0×10^{-3} within a factor of 10 [16]. Therefore, this study is roughly consistent with the results of the previous study. This is good considering the two studies were based on two different sulfidation data sets, and the accelerating effects of light on the sulfidation rate were not known at the time of the first study. Care was taken in the current experimental data set to reduce the room light. Whether light is the cause for the small but systematic (despite the large experimental scatter) lowering of the sticking coefficient in this study versus the previous study [16] is unknown to us. However, the trend in the data supports this hypothesis.

3.5.3 Limitations in This Analysis

There is an inconsistency in combining the quartic and quadratic dependencies in the reactions at the interfaces. In this analysis we utilize a quadratic dependency of the reaction on copper vacancies by invoking the presence of the uncharged vacancy at the gas-copper sulfide boundary while retaining the charged vacancy and hole combination at the copper sulfide-copper interface. The model may be refined in several relatively non-intrusive ways. For example, the use of uncharged vacancies may be relied upon throughout. Or, the model may be refit to employ holes and charged copper vacancies exclusively by refitting the rate constants to the quartic model. Copper vacancies would then be considered exclusively as charged. In reality, however, there is equilibrium between charged and uncharged copper vacancies that depends upon the ionization potential of the vacancy. In order to obtain an internally consistent treatment of the interfacial reactions, the process involving the ionization of the copper vacancy to a charged vacancy plus a hole will have to be treated correctly. This will involve tracking concentrations of both the charged and uncharged vacancy in the next model.

To summarize, in this study, parameters for the copper sulfidation corrosion model are estimated by fitting the model to selected sets of experimental data. The forward rate constant, reverse rate constant, and copper vacancy diffusivity are chosen for this exercise. These three parameters are obtained for three different relative humidity conditions: 0.5%, 20%, and 80%. It is shown that the current formalism cannot reproduce Cu_2S growth which transitions from Stage I to Stage II faster than the diffusion-limited rate, as it is observed in many experiments. The experimental data contain considerable scatter in both Stage I and Stage II regimes. This results in a wide range of fitted parameter values. The model can reproduce the linear growth region well, but the resulting $A1$ estimate span over four orders of magnitude. It is also known that the values of $A1$ and D_v can offset each other to produce similar growth behavior, indicating that multiple local minima exist for the optimization problem.

Agreement of the current model with experimental data in Stage II was generally scattered. Log sulfidation rate vs. log time plots indicated that experimental data had a 0.09 to

0.33 power-law time dependence in Stage II, while the model assumes a 0.5 power-law dependence. Thus, the model is inadequate in the Stage II regime. Additionally, the experimental data hinted at a statistically distributed onset of Stage II. The onset of Stage II within the model, however, is purely deterministic.

3.6 Adding the Growth and Diffusive Resistance through the Pore

Mechanistically, it is assumed that corrosion of gold-plated copper initially occurs at defects in the gold layer that allow contaminants to reach the copper surface. Corrosion products grow up through these defects, potentially resulting in blistering or rupturing of the gold layer leading to greater susceptibility to sulfidation of the copper substrate. For the corrosion of Cu from H_2S system, little or no signs of blistering have been observed experimentally, the system has been modeled as one where corrosion products grow up through the defect sites.

Once the corrosion product has exited from the pore it is modeled as a spherical flowerlet. Growth of the aforementioned spherical flowerlet on top of a pore can be modeled as two 1-D problems. Fig. 23 provides a schematic. Initially the Cu_2S will grow up through the cylindrical pore in one-dimensional geometry until it spills out on top of the plating into corrosion product bloom growth. Then, it can be modeled as one-dimensional hemispherical growth. At the intersection between the two coordinate systems, the copper vacancy fluxes must be equated. The boundary conditions on the inner sphere must be adjusted to take into account of the diffusion resistance of copper vacancies through the pore. Diffusion through the cylindrical pore in the gold layer is modeled via a simple one dimensional film theory model: C_V^{S1} is the concentration of vacancies at the bottom of the pore, at the copper – copper sulfide interface. C_V^{S2} is the concentration of copper vacancies at the top of the pore, and also at the spherical shell of the spherical domain. Then, the flux through the pore is equal to

$$A_{pore} j_{pore} = \pi \left(R_{pore} \right)^2 D_V \left(\frac{C_V^{S2} - C_V^{S1}}{h_{pore}} \right). \tag{36}$$

The variable A_{pore} is the cross-sectional area of the pore, J_{pore} is the diffusive flux, R_p is the radius of the pore, C_V^{S1} is the concentration of vacancies at the bottom of the pore, i.e., copper-copper sulfide interface. C_V^{S2} is the concentration of copper vacancies at the top of the pore, and also at the surface of the spherical shell of the spherical domain. The total vacancy flux must be equal to the diffusive flux into the spherical domain as well as the flux at the bottom of the pore; or Eqn. (37).

$$A_{pore} J_{pore} = A_{sphere} J_{sphere} = A_{bottom} J_V \tag{37}$$

This diffusive flux must be equal to the diffusive flux into the spherical domain, $2\pi \left(X_{bot} \right)^2 \left(\mathbf{j_v} \bullet \mathbf{n} \right)$. At the bottom of the pore, copper vacancies are injected into the copper using the previously described reaction, Eqn. (2). If we equate all three fluxes, we obtain a boundary condition for the inner radius of the spherical domain, Eqn. (38).

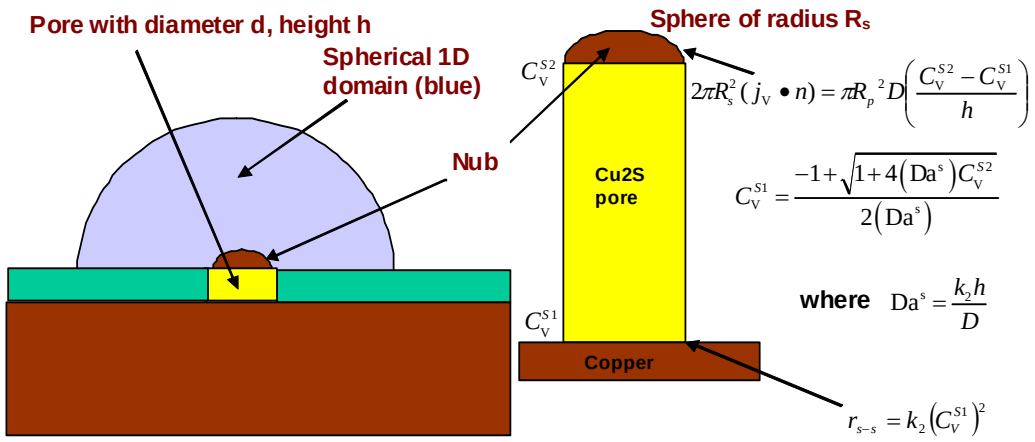

Fig. 23 Schematic of Cu_2S growth through a pore

$$2\pi\left(X_{bot}\right)^2\left(\mathbf{j_v}\bullet\mathbf{n}\right)=\pi\left(R_{pore}\right)^2 D_V\left(\frac{C_V^{S2}-C_V^{S1}}{h_{pore}}\right)=\pi\left(R_{pore}\right)^2 k_2\left(C_V^{S1}\right)^2 \tag{38}$$

The boundary condition, Eqn. (38), is implemented by solving a quadratic equation for C_V^{S1} so that Eqn. (38) only depends on C_V^{S2}.

$$C_V^{S1}=\frac{-1+\sqrt{1+4\left(\mathrm{Da}^s\right)C_V^{S2}}}{2\left(\mathrm{Da}^s\right)} \tag{39}$$

Da is defined as the dimensionless Damköhler number which characterizes the relative importance of the reaction rate and mass transport/diffusion.

$$Da=\frac{(A_2\exp(\frac{-E_2}{RT}))h_{pore}}{D_v} \tag{40}$$

The pore height, *h*, used in the formulas above is increased from the nominal pore height by $2/3\,R_{pore}$ to account for the extra volume in the starting spherical shell.

Modeling the corrosion product growth through the two regions (i.e., filling the pore followed by growth of the corrosion product bloom) can be combined into a single simulation if two calculations are run consecutively. In the first calculation, a one-dimensional geometry is used to grow a column of Cu_2S to a distance equal to the sum of the plating thickness and 2/3 the pore radius. The "2/3 pore radius" number is obtained by equating the volume of a cylindrical column with the volume of a hemisphere of the same radius. A linear interpolation between time step solutions based on the stopping criteria was employed to obtain the time to grow the initial column of Cu_2S up through the pore. Then, the code was started again in spherical coordinates mode, starting from a thin shell, with inner radius equal to the pore radius, with an initial time

equal to time to grow the initial column, and with an initial C_v equal to the previous C_v at the top of the column, and run until the end of the specified time.

Sample results are given in Fig. 24, where contrasting results for 3D flower growth are given both including and neglecting the diffusive resistance through the nub and the pore. The base case treats the copper layer as starting from the bottom of the spherical region, while the plating cases add in a "nub" region of height 2/3 the pore radius (0.66 μm in the case of Fig. 24) to the height of the Au plating thickness to account for diffusion through the "nub" spherical region (See Fig. 24) to the top of the Au pore. As can be seen from Fig. 24, the effects of the nub region can't be ignored.

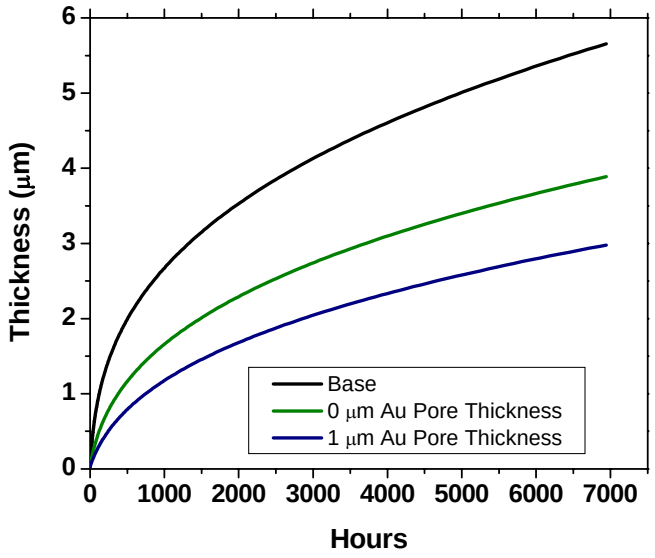

Fig. 24 Effect of plating thickness on the growth of the spherical flower growing out of a pore of radius 1 μm. Thickness on the axis refers to the thickness of the spherically modeled region. Parameter from fit to 8/31/01 data.

Fig. 25 contains results of this type of simulation as a function of the pore radius. The height of the protruding Cu_2S layer, *H*, above the plating is plotted as function of time. Note there is a constant delay time in all of the calculations equivalent to the time required for Cu_2S to grow up through and fill the pore. However, this delay time is fairly marginal for all of the cases, as the growth is fast when the Cu_2S layer is small. For the spherical coordinate case *H* is equal to the X_{bot} plus the thickness. For the initial Cartesian coordinate column, *H* is equal to 3/2 of the height of the layer above the plating. The 3/2 fudge factor is needed so that there isn't a discontinuity in height as the switch to integration in spherical from Cartesian coordinates is made.

After the Cu_2S layer emerges from the pore and begins to form a hemispherical deposit on the surface of the gold layer, the net rate of increase in the height of the suldide deposit is substantially moderated, due to combined influence of several effects. The first is the spherical

nature of the flower; there is an increase in large lateral area as the height above the pore increases. Thus, to increase the height above the plate, a large increase in Cu_2S volume is required. In addition, the copper needed to create that volume has to diffuse through a pore of fixed cross-sectional area. The second effect is the diffusional resistance increases as the hemispherical Cu2S deposit grows, due to the $L \alpha t^{1/3}$ dependence of spherical coordinates, discussed earlier in the memo. Thus, as the pore size gets smaller the height as a function of time gets smaller as well at a substantial clip.

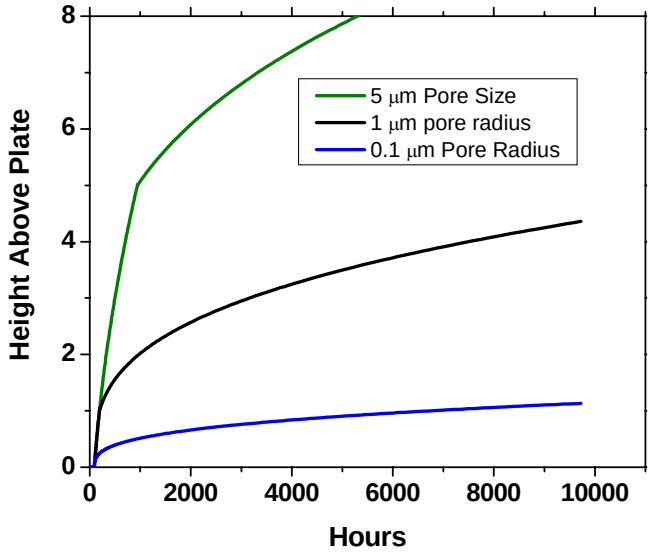

Fig. 25 Effect of the pore radius on the growth of corrosion blooms. The plating thickness is 1.0 micron. This is an intermediate step in the pore corrosion model. Note that the height above the plate is equivalent to the bloom radius. Parameters taken from 8/31/01 fits at 0.5% RH.

The model provides a complete solution to the source term for a corrosion product through an unloaded precious metal contact for the H_2S growth system. There is one reference in the literature that has addressed the same topic [7]. Sun et al. [7] have attempted to model the growth of flowers for the AuNi bilayer plating over Cu system in the Class II, MFG environment. In that study a one dimensional diffusion equation in Cartesian and cylindrical coordinates was used. However, a moving boundary approach was not implemented to locate the extent of the solid corrosion product

4.0 Source Term for Corrosion Product Films Due to Pores in the Gold Plating

4.1 Growing Probability Distributions of Pore Sizes

Through-deposit porosity is almost always present in thin electroplated gold films [27]. Additionally, it has been suggested in the literature that a Cl_2 + NO_2 mixed flowing gas environment can lead to actual corrosion of gold layer, generating additional defect sites in gold films [30, 31]. For the scope of modeling here, however, we will assume that quality of the plating is characterized by a constant-in-time average areal pore density, M_{pore}, which has units of number per cm2, and a pore-size probability distribution function, $P_s\left(r_p\right)$. The distribution of pores will be considered to have a Poisson form, i.e., their locations are independent of one another. Thus, the probability of there being *X* pores within a given area *A* of the surface is equal to

$$P(X) = \left(AM_{pore}\right)^X \exp\left(-AM_{pore}\right)/X! \quad . \tag{41}$$

And, the probability of there being one or more pores within the area, *A*, is equal to

$$P\left(N>1\right) = 1 - P(0) = 1 - \exp\left(-AM_{pore}\right) \quad . \tag{42}$$

The pore size, a crucial variable according to Fig. 25, will have its own normalized probability distribution, $P_s\left(r\right)$, where $\underline{r}$ is the radius of the pore, such that

$$\int_0^\infty P_s\left(r\right)dr = 1. \tag{43}$$

Thus, the average number of pores having radii between r_p^a and r_p^b on a given area of the surface is equal to

$$M_{pore}\int_{r_p^a}^{r_p^b} P_s\left(r\right)dr\,. \tag{44}$$

The areal pore density and pore-size distribution function are strong functions of the plating technique and thickness. It is hoped that in the future these distributions will be experimentally determined and married with this current analysis. However, for current purposes we must assume the pore distributions. It is assumed here that the log of the pore size distribution has a triangular shaped distribution with a minimum of 0.01 μm and a maximum size of 5.0 μm (and thus clustered around a size of 0.3 μm). It is further assumed that the areal density of all pores is 0.5 mm^{-2}, loosely based upon [Figure 3, 10], which shows an aged surface with a variety of corrosion product blooms, some of them in excess of 1 mm diameter, on a AuNi plated contact surface(0.38 μm Au / 1.26 μm Ni) after 6 days of Class II mixed flowing gas (MFG)

exposure. As will be discussed below, the bloom density from real films has been measured, and that analysis has been used to regress on the value of M_{pore} that fits the experiments.

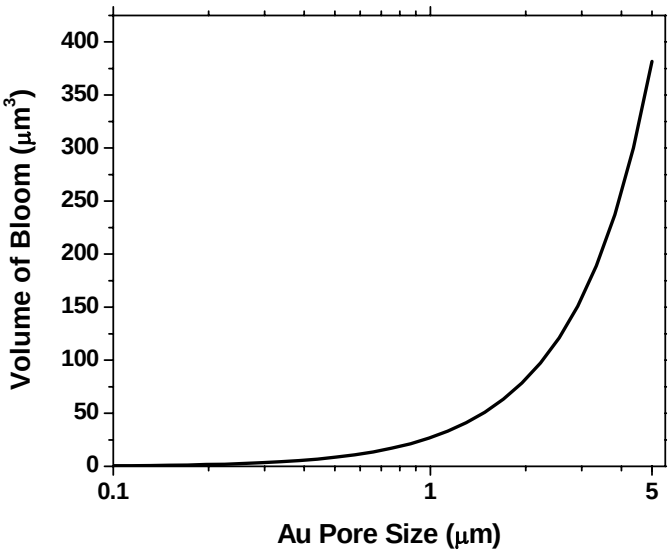

Fig. 26 Calculated corrosion product bloom volume as a function of the starting pore size for a 1 μm Au plating following exposure to 200 ppb of H_2S for 50 days.

Next, the pore model is integrated over a fixed time at a fixed H_2S concentration (200 ppb) to calculate the size and distribution of the resulting Cu_2S flowers. The total volume produced after 50 days exposure as a function of the pore radius is shown in Fig. 26. The volume curves are extremely skewed towards the high pore radius cases. They are by far the most important sources for the corrosion product. Finally, the distribution of pore flower sizes may be calculated. This is obtained from the 1 to 1 mapping function, $h_b = F(r_p)$, which maps r_p into h_b, the height of the bloom after growth, and $P_s(r_p)$. The determination of *F* has been the focal point for Section 3. Given an areal density of pores between r_p and $r_p + dr_p$ that is equal to

$$M_{pore} P_s \, dr_p ,$$

as described above, then the areal density of blooms between the heights, h_b and $h_b + dh_b$, is equal to

$$M_{pore} P_b \, dh_b = M_{pore} P_s \left(r_p\left(h_b\right)\right) \frac{dr_p}{dh_b} dh_b = M_{pore} P_s \left(F^{-1}\left(h_b\right)\right) \frac{dh_b}{F'} \tag{45}$$

The resulting areal density probability function, $M_{pore} P_b \left(h_{bloom}\right)$, is shown in Fig. 27 for the 200 ppb H_2S, 50 day growth case. The smallest pores have all grown to a radius of ~0.5 μm, while the largest pores (5 μm radius) have grown to greater than 5 μm in size. The clustering of original pores around the 0.2 μm size has caused the final bloom heights to cluster around the 2

μm level. The integral of $M_{pore} P_b \left(h_{bloom}\right)$ over all bloom heights is equal to the total area density of pores, 500 cm-2, which was a specified input variable.

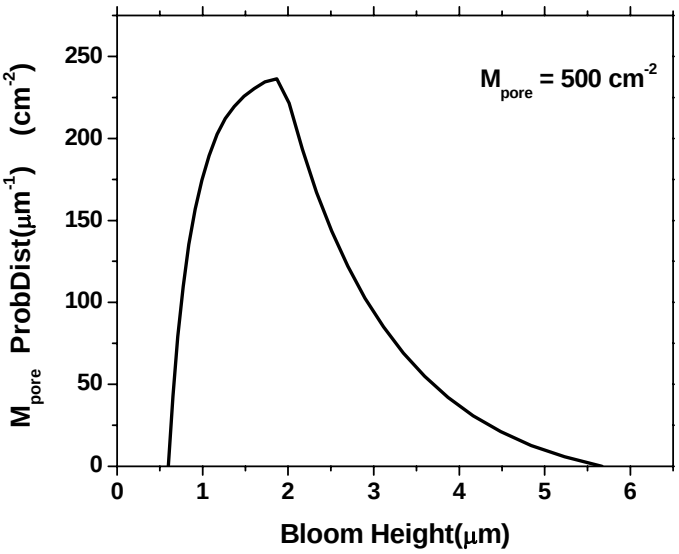

Fig. 27 Predicted area probability density of corrosion blooms as a function of their bloom height.

This distribution represent the sole source terms for the electrical resistance model. The oxide thickness is fairly low, but there always exists an organic coating of ~100Å on these surfaces. In MFG environments used in accelerated aging studies, an additional allied feature to the growth of a bloom is observed, the growth of a meniscus-like material along the gold contact itself, that is much larger in radius, but much thinner than the bloom. This meniscus is called the halo region [32], and has been observed to exhibit a large contact resistance (< 10 Ohms) as well, at least for late times with large blooms. In some cases this creep corrosion is the dominant mode for corrosion product growth [33, 34, 35]. The mechanism for this type of corrosion is not known presently. Without a detailed model for the thickness, the transport, the chemical/electrochemical reactions, and the mineral precipitation from this layer, the halo region must be treated here in an ad hoc fashion. Thus, initially, the halo formation phenomena will be accounted for in our contact resistance model by adding an extra ~10% of the volume growth due to blooms into the estimate of the uniformly distributed surface corrosion products. The correlation between the total amount of creep corrosion and the quality of the Au plating is thus grossly taken into account.

4.2 Corrosion Initiation at a Defect in the Gold Layer

While the corrosion kinetics have been approximated by a deterministic model, other factors, such as the distribution of defects (e.g., pores) in the gold layer that are susceptible to

atmospheric corrosion, have been addressed by a statistical approach. Given an initial pore density M_o^d (number cm^{-2}), upper and lower limits of pore radii, i.e. r^L and r^U, and a normalized probability distribution $P_o^d(r)$, we carry out multiple single-pore growth calculations to achieve a statistical population of corrosion product blooms. In the absence of experimental discovery, we have assumed that the distribution of pore radii is a logarithmically distributed hat function, where b is the normalization constant.

$$M_o^d \int_{r^L}^{r^U} P_o^d(r)dr = number\ of\ \ pores\ between\ r^L\ and\ r^U. \tag{46}$$

$$\int_0^\infty P_o^d(r)dr = 1, P_o^d(y) = \begin{cases} b4y & y < \frac{1}{2} \\ b4(1-y) & y > \frac{1}{2} \end{cases}, y = \frac{\ln(r) - \ln(r^L)}{\ln(r^U) - \ln(r^L)} \tag{47}$$

Given this type of model we should expect probability distributions representative of Fig. 27. As a function of time, the total number of blooms will approach a limiting value as each get big enough (> 2 μm) for direct observation via a microscope. However, the number density that's actually observed is presented in Fig. 28. The observation were taken in a 1.18 μm plated Au on Cu surface in a 70% RH, 30°C, 10 ppb H_2S environment.

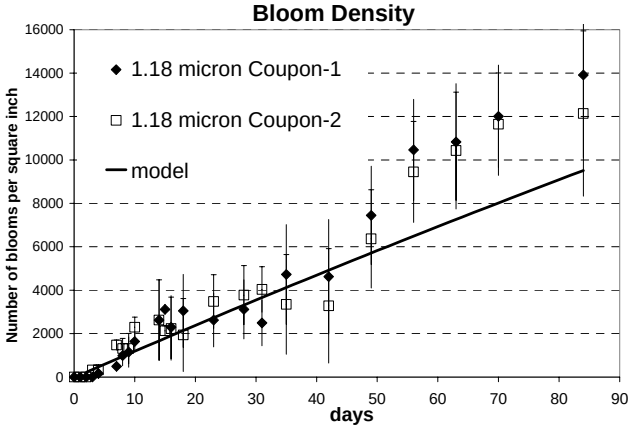

Fig. 28 Corrosion product bloom density as a function of time.

The time dependence of the corrosion product bloom density, which is basically linear in time, can be explained by an induction period for the start of growth. An induction period had previously been seen for corrosion growth from H_2S on bare copper coupons whose length was dependent on the relative humidity [11]. The cause of the induction period was attributed to the need to break down the native copper oxide layer or at least significantly puncture it before the sulfide growth could occur on top of the film. The induction period was longer for lower relative humidities, suggesting that the presence of a thin water layer may aid breakdown of the native oxide layer. This is in contrast to the relative independence of the corrosion rate with respect to the humidity level after the native oxide layer has been compromised. These observations of

induction periods for the growth on bare copper motivated our thinking for plated copper, where the area at the bottom of a pore might provide an extremely limited quantity of nucleation sites for the breach of the protective copper oxide film.

Therefore, we have incorporated an induction mechanism into the corrosion model, due to these observations that the bloom density increases as a function of time. We assume that the onset of growth of Cu_2S occurs with a finite areal probability, λ. λ has units of $cm^{-2}\ s^{-1}$. Thus, the onset of growth within the pore is greatly retarded for smaller pores due to an initialization rate proportional to the surface area.

Let $P_{uninit}(t, A)$ be the probability of a pore of size *A* being uninitiated at time *t*.

$$\frac{dP_{uninit}(t)}{dt} = -\lambda A P_{uninit} = -R_{init}(t) \tag{48}$$

$$P_{uninit}(t, A) = \exp[-\lambda A t],\ P_{uninit}(0) = 1. \tag{49}$$

λ is an adjustable parameter which dictates the time constants for the onset of growth. $R_{init}(t)$ is the rate of initiation of pore corrosion in pores of cross sectional area, *A*.

Because of this initiation process, even though the pores of same size grow at the same rate, their starting times may be different. Let $N(t, A, L)$ be the number of pores with initial area, *A*, having a height *L* at time *t*. Let n_0^A be the initial number of pores with cross-sectional area binned around *A*. *L* is a combination height coordinate. It spans the two calculations that comprise the pore growth model. The first calculation is based on 1-D Cartesian coordinates, while the second calculation is based on 1-D spherically symmetric coordinates. *L* is a continuous coordinate representing the height of the corrosion product above the plating material. Below the plating surface, *L* is equal to the height of the corrosion product layer in the pore. Above the surface of the plating layer, *L* transforms into the radius of the bloom product when the volume of a hemisphere of radius is equal to the volume of a cylindrical plug of radius r_{pore} and height L_o (i.e., $L_0 = \frac{2}{3} r_{\text{pore}}$). In this way the volumes are matched when transforming the growth model from 1-D Cartesian to 1-D spherically symmetric coordinates. Eqns. (50) and (51) describe the relationship between *L* and r_{bloom} for the spherical problem, and between *L* and *h* for the initial 1-D problem.

$$L = L_0 + r_{bloom} - r_{pore} \text{ for } L > L_o \tag{50}$$

$$L = h_{pore} - \gamma \text{ for } L < L_o \tag{51}$$

Let $G(A, L)$ be the time-independent growth rate of the corrosion product. It is a function of the initial area of the pore, *A*, and the height of the layer, *L*, at time *t*. We assume the ambient gas above the pore remains constant with time, and there are no "loading effects" in the reactor. The equation for the evolution of the distribution, $N(t, A, L)$, and its initial conditions may be described by Eqns. (52) and (53). These two equations are combined with a source term for passivation and solved via the method of characteristics [36].

$$\frac{dN}{dt} + \frac{d(GN)}{dL} = 0 \tag{52}$$

$$G(-\gamma, A)\, N(t, -\gamma, A) = n_o^A R_{init}(t, A) \quad and \quad N(0, L > -\gamma, A) = 0 \tag{53}$$

The solution to each of these equations is described in the following section.

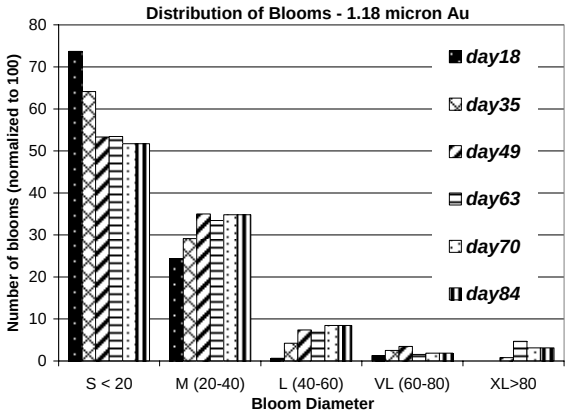

Fig. 29 Normalized size distribution of bloom sizes of 1.18 μm-plated copper. The bins are in units of microns.

4.3 Corrosion Site Passivation

While the number density of corrosion product blooms is observed to increase with time, the size-distribution of blooms remains relatively constant. This is illustrated in Fig. 29 which shows the corrosion product bloom size distribution at six discrete times for the same run conditions as Fig. 28. Note that the overall average bloom radius does not increase with time. This, combined with direct experimental observation (not presented here) indicates that a given corrosion site does not grow indefinitely. While the specific mechanism responsible for this phenomenon is unclear, there are several potential plausible explanations. One such explanation is that the coalescence of Kirkendall voids at the copper/copper sulfide interface has effectively cut off the bare copper surface within a corrosion site from the hydrogen sulfide in the gas phase, resulting in the cessation of copper sulfide formation, and hence the "death" of the corrosion site. This is supported in part via experimental observation of what appears to be void coalescence at the copper-copper sulfide interface, as illustrated in Fig. 30. Another plausible explanation is that the mode of copper sulfide formation has transitioned from Stage I to Stage II growth as observed experimentally for bare copper surfaces (illustrated schematically in Fig. 1), resulting in a dramatic reduction in reaction rate at corrosion site which would appear experimentally as though the corrosion site had "died".

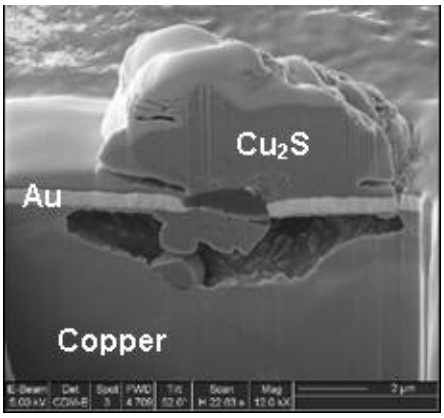

Fig. 30 FIB cross section of a single corrosion site and associated copper sulfide bloom.

In order to capture this phenomenon (i.e., corrosion site death) within the model, a probability-for-passivation source term is added to the time evolution equation, Eqn. (52). The variable *N* is redefined to be equal to the concentration of currently active pores.

$$\frac{dN}{dt} + \frac{d(GN)}{dL} = -R_{pass}(t, A) \tag{54}$$

We assume that there is a finite probability of passivation that is proportional to the total volume of copper removed from the underlying substrate, or proportional to the volume of copper sulfide created in the product layer, divided by the radius of the pore.

$$R_{pass}(t, A) = \beta \frac{V(L, A)}{r_{pore}} N_V\left(t, V(L), A\right) \tag{55}$$

β is the proportionality parameter. *V(L)* is the volume of copper sulfide created in the corrosion product layer. $N_V\left(t, V(L), A\right)$ is the number distribution of pores with product volume, *V*, at time *t*, that has an initial area *A*. It is related to $N(t, L, A)$ by a change of variables,

$$N_V\left(t, V(L), A\right) dV = N(t, L, A) \frac{dL}{dV} dV \tag{56}$$

$V(L)$ is the volume of copper sulfide created in the corrosion product layer. It is an analytical, monotonically increasing function that depends on the current height of the bloom, *L*, and the initial area of the pore, *A*.

$$V(L) = \begin{cases} (\pi r_{pore}^2)(L + \gamma) & \text{for} \quad L < L_0 \\ V_{plug} + \dfrac{4\pi}{6}\left(r_{bloom}^3 - r_{pore}^3\right) & \text{for} \quad L > L_0 \end{cases} \quad \text{where} \begin{array}{l} r_{bloom} = L - L_0 + r_{pore} \\ V_{plug} = (\pi r_{pore}^2)(L_0 + \gamma) \end{array} \tag{57}$$

r_{bloom} is the radius of the bloom. γ is the thickness of the plating. At $L = L_0$, the growth model changes from a 1-D Cartesian coordinate representation of growth in a cylindrical plug, to a 3-D spherical coordinate representation of growth in a hemisphere representing the bloom.

We again use method of characteristics [36] to solve for *G* and *N*, to yield

$$G(L,A)\,N(t,L,A) = \begin{cases} n_o^A R_{init}(t-\psi,A)K & t > \psi \\ 0 & t < \psi \end{cases}, \tag{58}$$

where $\psi(L,A) = \int_{-\gamma}^{L} \frac{dL}{G}$ and $\ln(K) = \int_{-\lambda}^{L} -\beta \frac{V}{rG} dL$.

We define $G(L,A)$ as a piecewise constant function of time.

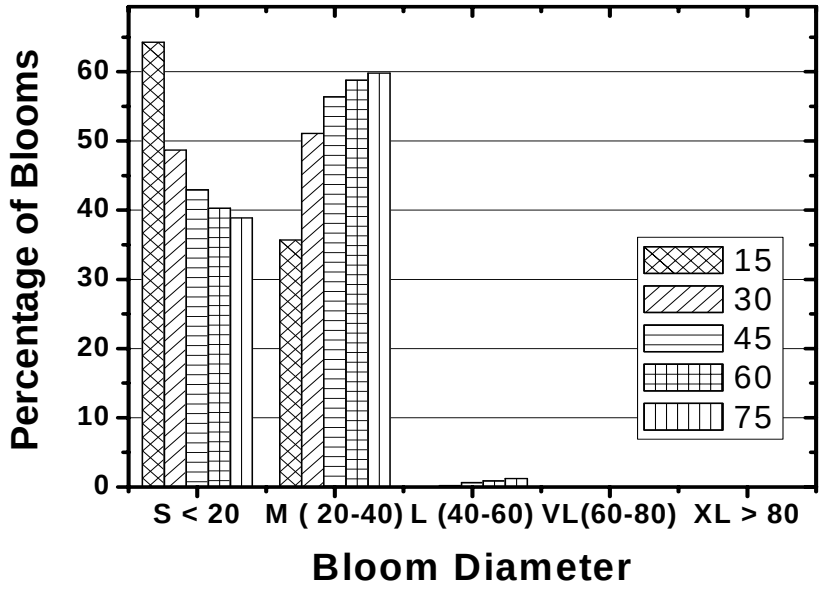

Fig. 31 Normalized, binned distribution of blooms from numerical model. The bins are in units of microns.

Fig. 31 displays the resulting number distribution binned as per the experimental data. While the addition of the passivation term has allowed the numerical model to generate the time-invariability of the bloom-size distribution seen in Fig. 29, several features of numerical model results in Fig. 31 are not in agreement with experiment. The numerical model demonstrates an inordinately high percentage of middle sized blooms compared to experiment. Both extremely large blooms and a sufficiently high number of small blooms do not show up in the numerical model. This may have to do with the simplistic treatment of the phenomena used in describing the death rate in Eqn. (55), where all bloom sites are treated equally.

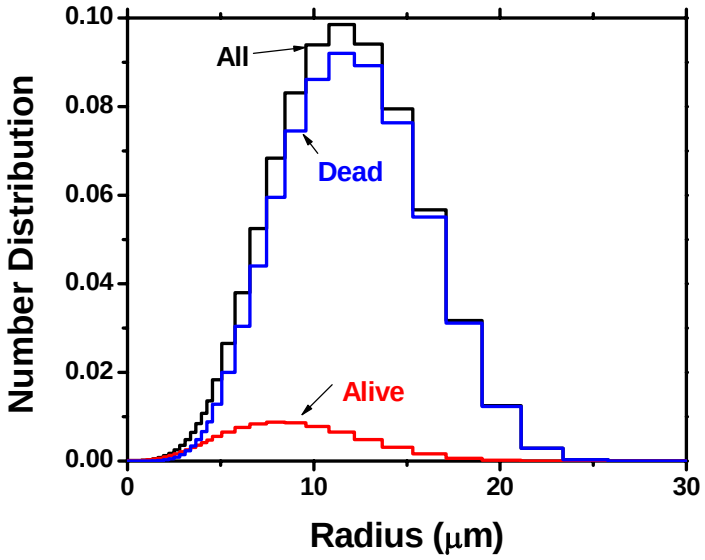

Fig. 32 Predicted bloom distribution function at day 45. The number distribution of actively growing and "dead" corrosion site distributions is shown.

Fig. 32 gives more detail about the bloom distribution predicted at day 45. With the exception of small corrosion product blooms (i.e., below 5 μm), the population is dominated by dead corrosion sites, i.e., corrosion sites that have ceased growing. As the corrosion product volume at a single corrosion site increases, the probability of corrosion site death also increases, leading to sharp decrease in the number of corrosion product blooms over 20 μm. Additionally, a small number of pores (relative to the experimental data) die at the small sizes due to the their small volumes . No attempt however has been made to tweak the dependence of Eqn. (55) on *V*, due to the speculative nature of employing these formulations.

4.4 Solving the Discretized Time Dependent Evolution Equation

Taking a step back, we will describe some of the issues with solving the discretized form of Eqn. (58). A form of the growth rate, $G(L, A)$, discretized in both the L and the A coordinate, must be stored for the model. The final time limit provides an upper bound of bloom size for given a value of A. This may be used to create a limiting value of L in the data structure for G, needed for the model. The growth of the corrosion product layer is determined as a series of backward Euler first order time steps. These steps may be used to as a natural way to create a

piecewise, constant representation of the growth rate as a function of *L*. Basically, we define the growth rate on the interval $L_{n-1} < L < L_n$, $G(L_n, A)$, as being equal to the following equation:

$$G(L_n, A) = \frac{L_n - L_{n-1}}{\Delta t_n} \quad . \tag{59}$$

A discretization of the pore radius dimension is also done. Therefore, $G(L_n, A_j)$ represents a two dimensional matrix of values. $G(L_n, A_j)$ is constructed in the first computer program, `cu2s_1d_mps`. The two dimensional matrix of values is supplied as input to the second of the three programs, named `cu2s_pore`, that makes up our electrical contact resistance model. Along with $G(L_n, A_j)$, the time or equivalently ψ is recorded with L_n for every radius A_j.

If $G(L, A)$ is a piecewise continuous, constant function of *L*, then for a given *A*, assuming that $G(L_{n-1} < L \le L_n, A) = G(L_n)$ is a constant:

$$\ln(K(L_n)) = \ln(K(L_{n-1})) + \int_{L_1}^{L_2} -\beta \frac{(\pi r_{pore}^2)(L+\gamma)}{r_{pore} G} dL$$

$$\ln(K(L_n)) = \ln(K(L_{n-1})) - \beta \frac{(\pi r_{pore}^2)}{r_{pore} G(L_n)} (L_n - L_{n-1}) \left(\frac{(L_n + L_{n-1})}{2} + \gamma \right) \text{ for } L < L_0 \tag{60}$$

And therefore,

$$\ln(K(L_n)) = \ln(K(L_{n-1})) - \beta \frac{(V_{plug})(L_n - L_{n-1})}{r_{pore} G(L_n)} - \frac{\beta \pi}{6} \frac{\left(r_{B,n}^4 - r_{B,n-1}^4 - r_{pore}^3 (r_{B,n} - r_{B,n-1})\right)}{r_{pore} G(L_n)} \tag{61}$$

$$\text{for } L > L_0$$

Eqn. (60) and Eqn. (61) provide the necessary formulas for obtaining the degree of Kirkendall voiding that occurs during each of the sections, L_{n-1} to L_n, that comprise a piecewise continuous representation of the corrosion growth rate function, $G(L_n)$. $K(L_n)$ is provided as a function of L_n and therefore as a function of time by the program `cu2s_1d_mps`.

The integrations used in the program `cu2s_pore` are depicted in Fig. 33 for a single bin representing pores with cross-sectional area, A_j. The pink curves represent the same trajectory of pore corrosion growth but displaced by the starting times for growth. The pink curves are piecewise linear, because the growth rate is approximated as a piecewise constant function, Eqn. (59). In order to find the distribution of heights *L* at time *t*, we bin the *L* coordinate using control volumes at the time t, represented by the heavy blue line. The middle of the control volumes is represented by the blue X's, while the sides of the control volume are represented by the dashed green curves. Since no growth trajectories cross the purple curves, events which happen on the $L = -\gamma$ line at $t = 0$ between purple curves representing the sides of the control volumes propagate themselves into the control volume at time *t*. This represents an integral condition for the conservation of events, and can be derived from the equation:

$$G(L, A_j) N(t, L, A_j) = n_o^{A_j} R_{init}(t - \psi(L, A_j), A_j) K(L, A_j) \,, \tag{62}$$

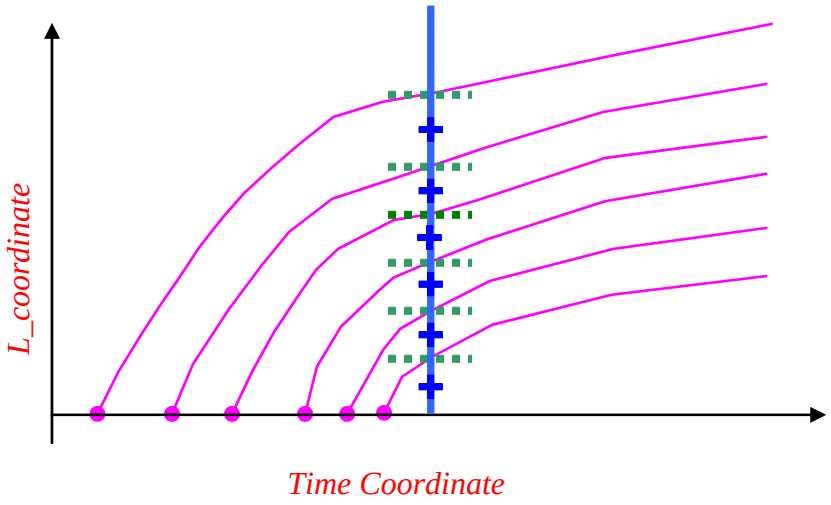

Fig. 33 Schematic of integration in the L and the time coordinate for a single initial pore size, A_i. Probability distribution bins in the L coordinate centered at the blue X's are bounded by green dashed lines. The green dashed lines can be traced back to starting times on the $L = -\gamma$ line.

using a suitable integral control volume approach. This feature is used within `cu2s_pore` to derive an integration approach which conserves the probability distribution function. A key input to the procedure is an estimate of the number and distribution of pore sizes. The model can accept various distribution forms for the pore size distributions. The distribution really should be an experimental input. However, absent of experimental discovery, for our sample calculations, we have assumed that the distribution of pore radius is a hat function in the $\log\left(r_{pore}\right)$ coordinate, within minimum and maximum values of 0.1 μm and 5 μm.

The calculation depicted in Fig. 33 is carried out for each initial pore size in the original binned pore probability distribution in order to derive the number of live pores at the current time, Eqn. (62). Additionally, each control volume calculates the probability density of dead pores for control volumes that correspond to lower bloom sizes at each time. In that manner, the probability distribution of dead bloom presented in Fig. 32 is calculated. After the probability distributions for live and dead pores are calculated for each individual radius, the areas, A_j, are calculated at the current time, and the individual distributions are combined into a total distribution of live and dead pores at the current time for the current control volume representation.

There is a subtle coordinate transformation between L and r_{bloom}. In the previous pages we referred repeatedly to the coordinate L. The explicit definition for this coordinate was given in Eqn. (50) and Eqn. (51) in terms of the independent variables of the two subproblems, h and r_{bloom}. However, for purposes of analysis and presentation, a new coordinate is needed which is based upon r_{bloom}, can represent the results of both the Cartesian and spherical coordinate subproblems, doesn't depend on r_{pore}, and can be mapped on a 1 to 1 basis into L. The coordinate transformation, which depends on r_{pore}, is given below.

$$r_{bloom} = L - L_o + r_{pore} \qquad \text{where } L_o = \tfrac{2}{3} r_{pore} \text{ for } r_{bloom} > r_{pore} \tag{63}$$

$$r_{bloom} = \tfrac{3}{2} L \qquad \text{for } 0 < r_{bloom} < r_{pore}$$

$$r_{bloom} = L \qquad \text{for } r_{bloom} < 0$$

Within the program the results are first calculated in the *L* coordinate at different values of r_{pore}. Then, the resulting probability distributions are transformed into the r_{bloom} coordinate, and all r_{pore} results are binned together, to produce a final probability distribution in the r_{bloom} coordinate. The final distribution of pores is written to an ASCII file to be utilized in the electrical contact resistance model.

One additional manipulation is carried out on the distribution of pores. The pore distribution is divided into two types; those that are treated as small and combined into a uniform corrosion film, and those that are treated as large blooms and are treated in a statistical manner in the electrical contacts program. The cutoff size for distinguishing between these distributions is given by the following formula.

$$V_{bloom} > f\,\sigma\left(A_{hertz} + l_{wipe} D_{hertz}\right) \tag{64}$$

If a bloom occupies an area larger than a fraction, *f*, of the product of the Hertzian contact area, A_{hertz} and diameter, D_{hertz}, and surface roughness, σ, then the effect of the bloom is treated in a different manner. The bloom fraction cut off, *f*, is an adjustable parameter in the model, nominally set to 0.1. This choice of *f* reflects bloom population in a subset of "small" and all of "medium and above" categories. If the bloom area exceeds *f*, then parts of the Hertzian contact area will be unavailable for direct contact except via conduction through the corrosion product bloom due to steric hindrance. Wipe, with length l_{wipe}, serves to greatly increase the area over which the bloom product may be "wiped" below the thickness where it would preclude close contact between the two surfaces. This empirical model serves to adjust the degree of a tail end distribution on CPD plots for electrical contact resistance.

The total volume of small blooms is assumed to comprise a uniform surface corrosion product layer and is used as input to contact resistance model. This total volume is also augmented by 10% of the total volume of all types of blooms. The modification was needed so as to not create situations where the contact resistance for some parts of a CPD curve to be less at late times.

5.0 Electrical Contact Resistance Model

In the previous section, an evolution model for the growth of copper sulfide blooms is created and simulated to compare with the experimental measurements of bloom morphology. The results from that model must now be linked to a contact resistance model so that the impact of corroded surface topology on the electrical contact process may be gauged.

There are numerous theories on electrical contact resistance. In particular, Greenwood's work on electrical contact theory spawned numerous theoretical developments [37]. The key element of Greenwood's work is the recognition that two levels of constriction exist when two rough metal surfaces make contact – the first level being the superficial contact area and the second level being the contacts through micron-sized asperities.

Our approach follows much of Malucci's extension of Greenwood's formalism to aging surfaces [38, 39, 41]. The model is presented below by first describing the macroscopic process of contact of a probe (or tine) with an aged surface, obtaining the macroscopic diameter of the contact and the distribution of pressures within the contact. Next the rough theory for what happens at the micron-sized level in the contact given that both contacting surfaces have roughness associated with them is described; there are a variable number of contact points, called asperities, where actual contact between the two surfaces take place. The equations used in the code for calculating the number of such asperities and the actual area of contact versus the nominal area of the contact as a function of the load on the probe are then presented. Lastly, the theory for the electrical contact resistance that is used to model contacts between aged surfaces is described. Current must only flow through this limited number of asperities. Within each asperity contact, the process of creating the contact may or may not have wiped off the aged film that encases the surface, causing true metal-to-metal contact through that asperity. The total resistance through the contact is then calculated based on the sum of these phenomena.

The two contributions that make up the total electrical contact resistance. R_{ECR}, namely the apparent contact resistance R_{int} and the resistance due to asperities R_{spots} have the following forms.

$$R_{ECR} \equiv R_{spots} + R_{\text{int}} \tag{65}$$

$$R_{\text{int}} = \frac{\rho}{D} \tag{66}$$

$$R_{spots} = \frac{1}{\sum_{N} \frac{1}{R_i^{spot}}} \tag{67}$$

R_{int}, the resistance due to apparent contacting area, is based on Holm's formula for contact resistance [41]. ρ is the resistivity of copper. D is the diameter of the overall cluster of asperities, and is obtained from the Hertz stress formula for the actual diameter of contact between a sphere and a plate under elastic deformation. R_{spots} is calculated via a sum of parallel resistances of the resistances of each individual asperity. R_i^{spot}. N is the total number of

asperities. Note, if all asperities have diameters, *d*, and are clean metal-to-metal contacts, then Eqn. (65) reduces to the following formula, which is known as the Holm formula.

$$R_{ECR} \equiv \frac{\rho}{D} + \frac{\rho}{Nd} \tag{68}$$

Interference effects between asperities, which are close to one another, are known to exist, altering the basic formula represented by Eqn. (65) - (67) (see ref. [42] for treatment of this phenomena). However, they are ignored in the present analysis, because the addition of the corrosion films to the electrical contact analysis will make their influence minor in their real effect.

5.1 Contact between Two Rough Surfaces

To start off the analysis, we assume that a probe (or tine from a connector), with radius R_{probe} is pressed into a contacting surface to create a macroscopic contact. The contact force is given in Newtons and usually expressed in terms of the gram equivalents based on gravity. *D* is the diameter of the macroscopic contact and is obtained from the Hertz stress formula for the actual diameter of contact between a two spheres of material 1 and 2 under elastic deformation [43]; i.e.,

$$D = 2.\left(\frac{3FR^*}{4E^*}\right)^{1/3} \qquad A_n = \tfrac{1}{4}\pi D^2 \tag{69}$$

where

$$R^* = \left[\frac{1}{R_1} + \frac{1}{R_2}\right]^{-1} \qquad E^* = \left[\frac{1-\nu_1^2}{E_1} + \frac{1-\nu_2^2}{E_2}\right]^{-1}$$

F is the force applied on contact. A_n is the area of the contact. E_1 , E_2 , ν_1 , and ν_2 are the elastic moduli of the contacting metals, and R_{probe} is the radius of contacting probe. Typical values for *E* for gold are 125 GPa and ν =0.42. Thus, with a probe radius of 0.5 cm, and a contact load of 50 gm, the nominal contact diameter may be calculated to be 69 μm. Within the overall cluster of asperities, *D*, the load is not uniform, being higher in the center of the probe and lower at the edge [Eqn. 18, ref. 39].

In Malucci's treatment, the force of one surface on another, *F*, is assumed to be radially distributed via the following formula for the local pressure:

$$P = \left(\frac{1.5F}{A_n}\right)\left(1 - \left(\frac{r}{r_0}\right)^2\right)^{1/2} . \tag{70}$$

Effectively what this means is that there will be more total contact in the middle of the probe than at the edge.

This analysis of the Hertz stress and associated pressure distribution may be considered the macroscopic model for the contact process of the probe with respect to the surface. However, the macroscopic model needs to be married to a microscopic model for contact between the two surfaces, which are rough, from which the actual number of contact points, i.e., asperities, may be generated as well as the actual (vs. nominal) contact area.

The number of asperities within the contact area is calculated from the following principles. We first derive an implementation for the statistics of two rough surfaces impinging on each other, driven together by a normal force. As the force between the surface increases, both the number of contacts, i.e., asperities, and the overall area of the contact increases. At high force levels the number of asperities actually will begin to decrease as the contact area continues to increase, due to the plastic flow and coalescence of the asperities.

Let's introduce $W^1(h)$, the probability density function for the profile height for a single surface. The independent variable, *h*, is the height of the surface above a zero baseline. As with all density functions, the integral of the function over all heights must be equal to one, i.e.:

$$\int_0^\infty W^1(h)\,dh = 1 \quad , \tag{71}$$

which implies that the units of $W^1(h)$ is inverse length. In general $W^1(h)$ is a complicated function determined by exhaustive profilometry. However, Malucci, motivated by a rough binning exercise carried out on actual profilometer data, approximated $W^1(h)$ by the following half-sine function,

$$W^1(h) = \frac{\pi}{2h_o}\sin\left(\frac{\pi h}{h_o}\right), \tag{72}$$

where h_o is the characteristic surface roughness.

What we are really interested in, however, is a probability density function for the distances between two rough surfaces that approach each other, $W(Z)$, where we have dropped the superscript 1 to denote a density function involving 2 interfaces. Define $Z = h + h'$ as the distance between the zeros of two rough surfaces as they approach each other. The range of *Z* is $0 < Z < 2h_o$, assuming both surfaces have the same roughness. It can be shown that, assuming each surface has the form given in Eqn. (72), that the resulting convolution results in

$$W(Z) = \begin{cases} \dfrac{\pi}{8h_o}\left(\sin\left(\dfrac{\pi Z}{h_o}\right) - \dfrac{\pi Z}{h_o}\cos\left(\dfrac{\pi Z}{h_o}\right)\right) & : 0 < Z < h_o \\ \dfrac{\pi}{8h_o}\left(\sin\left(\dfrac{\pi d}{h_o}\right) - \dfrac{\pi d}{h_o}\cos\left(\dfrac{\pi d}{h_o}\right)\right), \quad d = 2h_o - Z & : h_o < Z < 2h_o \end{cases} \tag{73}$$

Note, that $W(Z)$ yields the percentage of the real contact area, A_r, compared to the nominal contact area, A_n, through a simple integral.

$$A_r = A_n \int_{\varepsilon}^{2h_o} W(Z)\,dZ \tag{74}$$

Here, ε is the distance between the reference-plane zeroes of the two surfaces' individual density functions, $W^1(d)$, and is defined as the actual macroscopic distance between the two contacting surfaces. This means that the actual area of contact, A_r, may be parameterized as a function of A_n and the separation distance, ε. Fig. 34 contains a plot of Eqn. (74) assuming the distribution in Eqn. (73).

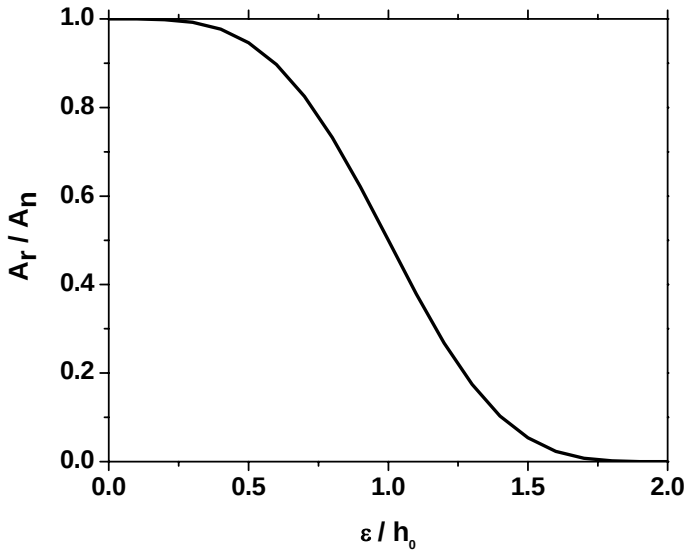

Fig. 34 Ratio of the real contact area, A_r, to the nominal contact Area, A_n as a function of the normalized distances between surfaces.

The next step is to derive a spot density, *n*, of asperities. This essentially involves understanding how A_r is broken up into chunks. The concept of an average slope m of the asperities must be added to the above discussion to derive the areal density of intersections of $W(Z)$ with any single value of *Z*. Essentially, what the *m* (which is dimensionless) represents, is a measure of the size of each individual feature on the surface. Malucci [39] eventually derives Eqn.(75).

$$n = \frac{1}{27}\left(\frac{A_n}{A_r}\right)\left(mW(e)\right)^2 \tag{75}$$

Several authors have reported statistical derivations of this quantity [44, 45, 46], and they derive a very similar formula that only varies by a numerical constant out front. Note that *n* has units of # / length^2, which is the correct unit for an areal density.

In order to apply Eqn. (75), $W(e)$ must be expressed as a function of A_r / A_n. Note Eqn. (74) expresses A_r / A_n as a function of *e*, so it's just a matter of eliminating *e* from the equations to yield, via a fitting process from Malucci [39], the approximate relation:

$$W(e) = W(h_o)\left(\left(\frac{4A_r}{A_n}\right)\left(1-\frac{A_r}{A_n}\right)\right)^{3/4} . \tag{76}$$

Now, Eqn. (75) is a function only of A_r / A_n. The missing piece is a relation expressing the value of *e* as a function of the local pressure *P*. In other words as the local force increases, the two surfaces will be pressed together on the micron scale. Again, several authors have addressed this question previously [47, 48], and the following empirical formula has been adopted by Malucci:

$$\frac{P}{H} = \frac{A_r / A_n}{1 - A_r / A_n} \quad . \tag{77}$$

Here, *P* has been normalized to *H*, the microhardness. Eqn. (77) does a good job fitting data for *P/H* > 0.4 in ref. [48]. In the low pressure limit, Eqn. (77) is almost a tautology, because it equates to the definition of the microhardness material property, *H*.

To see how this result carries out in practice, we may combine the Hertzian formulas for the macroscopic deformation given previously, Eqns. (69) and (70), with the above formula to derive representative numbers for our application. Using numbers characteristic of our probe for loads from 20 to 100 gm, yields Fig. 35, which relates the A_r / A_n value and P_o / H value to the force on the probe. P_o is the local pressure at the center of the probe.

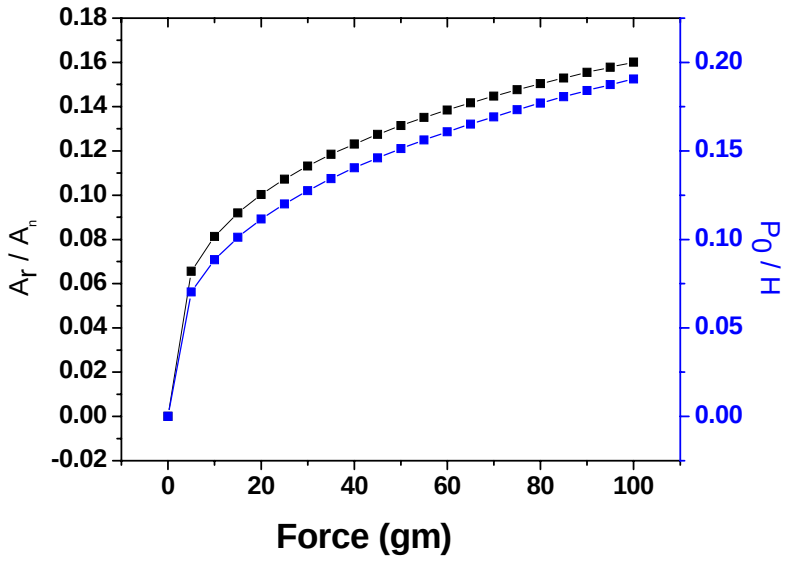

Fig. 35 Ratio of the real contact area, A_r, to the nominal contact Area, A_n as a function of the weight on the probe of radius 0.5 cm. *H* = 1.2 GPa, *E* = 125 GPa

Correlation of *e* vs *F* may also be obtained by comparing Fig. 34 and Fig. 35 together. A_r / A_n are in the 0.10 to 0.16 range, which means that $\varepsilon / h_o \approx 1.3$ for our application. In general, therefore, the surfaces are pressed together on the microscopic level to a very limited amount, such that contact occurs through isolated asperities.

Then, we integrate the density of spots, Eqn. (75), over the entire macroscopic contact point assuming a circular distribution of pressures equal to

$$P = \left(\frac{1.5F}{A_n}\right)\left(1-\left(\frac{r}{r_0}\right)^2\right)^{1/2} , \tag{78}$$

using the formula for *N*, the total number of asperities:

$$N = \int_0^A n 2\pi r dr \ . \tag{79}$$

The end result for the number of asperities is Malucci's Eqn. (24) in ref. [39]. This equation is used in the program, contactRes, as the basis for our calculation of *N* in the routine `calcNumberAsperities()`.

$$N = K\left(\frac{F}{H}\right)\frac{\left\{\frac{1}{3}\left(\frac{P_o}{H}\right)^{3/2} - \left(\frac{P_o}{H}\right)^{1/2} + \tan^{-1}\left(\frac{P_o}{H}\right)^{1/2}\right\}}{\left(\frac{P_o}{H}\right)^3} \tag{80}$$

P_o is the maximum Hertz pressure for the contact, calculated from Eqn. (78) with *r* = 0. *F* is the contact force. *K* is a constant equal to $(16/9)\left[m\,W(h_o)\right]^2$. In the calculations, we assumed that the microhardness of the surface, *H*, is equal to 170 ksi or 1.2 GPa, a common number assumed for Gold. Then, for a 10 g to 200 g load, the normalized pressure, P_o / H , is calculated to vary from 0.1 to 0.36, and a plot of *N* vs. load is presented in Fig. 36.

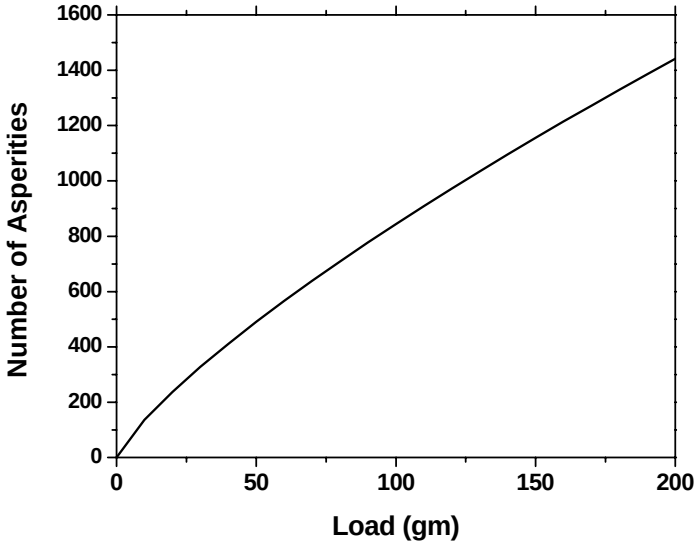

Fig. 36 Number of asperities as a function of the applied load, assuming H = 170 ksi, $m / h_o = 2.78 \times 10^4 \text{inch}^{-1}$.

One input to the model through its dependence on K is the ratio of the average slope of the surface, m, to the surface roughness of the film, h_o. We employed a value m / h_o of $2.78 \times 10^4 \text{inch}^{-1}$ a value used in Malucci's paper, since we do not have independent information for its value. Essentially, however, the number of predicted asperities is proportional to the square of m / h_o through Eqn. (80).

An additional important parameter for the electrical contact resistance model is the average Interference, I. This is defined as the average height of the "overlap" of the surfaces, when the surfaces do overlap. With a little bit of thought, the following integral may be derived for I.

$$I = \int_{\varepsilon}^{2h_o} (Z - e) W(Z) dZ / (A_r / A_n) \tag{81}$$

The average Interference is used in the electrical contact resistance model for aged surfaces derived below. Eqn. (73) may be plugged into the integral, and the integral in Eqn. (81) may be calculated numerically. However, within the program, we fit I to the results from Fig. 11 Ref. [39] with a linear curve.

In the above analysis we have assumed that Hertzian contact theory applies to rough surfaces. Greenwood and Trip [40] demonstrated that this was a false assumption. They found that while for higher loads Hertzian contact theory applied to rough surfaces, for lower loads the effective pressure distribution was much lower and extended to much further distances than Hertzian theory predicts on rough surfaces. The application of Greenwood and Trip's theory

would modify the equations of this section, especially Eqn. (70), perhaps leading to different predictions for the electrical contact resistance's dependence on load. However, as will see in later sections, when there are corroded surfaces, the main electrical contact resistances are due to corrosion-film layers on top of the rough surface, thereby masking a lot of subtle details concerning contact between "clean rough" layers. For this reason, we have not pursued Greenwood and Trip's analysis.

5.2 Electrical Contact Resistance Model

We divide the problem into two parts. In the first part we describe the electrical contact resistance model based on the assumption that there exists a uniform corrosion product layer that provides an extra layer of resistance at each of the micron-sized asperities created during the contacting process. In the second part, we describe modifications to this micron-sized asperity model due to larger scaled blockages of the contact from the corrosion-product bloom and halo growth (i.e., creep corrosion films) that are observed. It has been shown that electrical contact may be severely hindered or essentially terminated if the probe lands on a bloom or halo [32]. Therefore, the micron-sized asperity model must be modified to account for these issues in a statistical way.

The uniform corrosion-product resistance model is based on a sum of constriction resistances formulation initially introduced by Greenwood and Holm [41, 45]. Two contributions that make up the total electrical contact resistance R_{ECR}, namely the apparent contact resistance R_{int} and the resistance due to asperities R_{spots} have the following forms.

$$R_{ECR} \equiv R_{spots} + R_{\text{int}} \tag{82}$$

The constriction resistance due to the macroscopic Hertzian contact area, R_{int}, handles the increased resistivity within the metal due to the small macroscopic size of the nominal contact area [41].

$$R_{\text{int}} = \frac{\rho}{D} \tag{83}$$

ρ is the resistivity of copper, while D is the Hertzian contact diameter given by Eqn. (69).

Within the overall constriction, current flows in a parallel manner through each of the numbered asperity, from 1 to N, where each asperity has its own resistance, R_i^{spot}. Therefore, the formula for R_{spots} is given by the parallel resistance formula, Eqn.(84).

$$R_{spots} = \frac{1}{\sum_N \frac{1}{R_i^{spot}}} \tag{84}$$

The resistance of each asperity is taken from Malucci's work [38, 39, 41], [43, 49], where parallel resistance pathway is envisaged for each asperity, i, between direct metallic contact and between conduction through a partially conductive oxide/sulfide interfacial film.

$$\frac{1}{R_i^{spot}} = \frac{1}{R_i^{spot\_metallic}} + \frac{1}{R_i^{spot\_film}} \tag{85}$$

Resistance, if there is direct metallic contact, is given by

$$R_i^{spot\_metallic} = \frac{(1-C)\sqrt{X_i X_i^{'}} + C}{d_i \sqrt{X_i X_i^{'}}} \rho \ , \tag{86}$$

while resistance for the *i*th asperity from an interfacial film is given by

$$R_i^{spot\_film} = \left(\frac{\sigma_i}{A_i} + \frac{\rho}{d_i} \right) \left(\frac{1}{1-\sqrt{X_i X_i^{'}}} \right) = \left(\frac{4\sigma_i}{\pi d_i^2} + \frac{\rho}{d_i} \right) \left(\frac{1}{1-\sqrt{X_i X_i^{'}}} \right) \ . \tag{87}$$

d_i is the diameter of the i^{th} contacting asperity. C is a numeric constant set to 4/3. The fractions of exposed metal on both sides of the i^{th} asperity are defined as X_i and $X_i^{'}$. Malucci provides much of derivations for d_i, N, X_i and $X_i^{'}$ which we also utilize in our model [38, 39, 41],. Let's go through these in detail.

Within the code we set each value of d_i to the following statistically varying quantity

$$d_i = 2 d_{avg}^i P[0,1] \tag{88}$$

where $P[0,1]$ is a transformed deviate uniformly distributed over the interval from 0 to 1. d_{avg}^i is the average diameter of a single asperity, calculated from the following formula:

$$\frac{N\left(\frac{1}{4}\pi {d_{avg}^i}^2\right)}{A_n} = \left(\frac{A_r}{A_n} \right) \ . \tag{89}$$

A_r / A_n is obtained from Eqn. (77), N is obtained from Eqn. (80), and A_n is obtained from Eqn.(69).

The most crucial and probably most uncertain submodel is the one for X_i and X_i', the fractions of clean metal exposed on contact asperities. The product of X_i and X_i' is an estimate of the chance for metallic contact to occur on the i^{th} asperity. Obviously, this product is a function of the degree of contact at the i^{th} asperity, and is therefore a function of the degree of pressure exerted between the surfaces on a microscopic level. It's also assumed that there exists a uniform corrosion film on top of each surface. During the contacting process this film must be "wiped" away in order for there to be metal-metal contact. The degree of "wiping" is handled by assuming that there exists a zone in the asperity where there is a general mixing of the metal and the corrosion product due to the contacting process. The end result of the mixing is a power law distribution of the fraction of the oxide, F, within the zone of mixing.

$$F(y) = F_0 (N+1) \left(1 - \frac{y}{h_i} \right)^N \tag{90}$$

h_i is the largest depth of oxide penetration for the i^{th} asperity, which we will assume to be derived from a statistical distribution of the average interference parameter, *I*, calculated in Eqn.(81). F_o is the fraction of oxide at the surface of the mixing layer. *N* is the power law distribution within the mixing layer; We have followed Malucci and set *N* to a default value of 4, which was used in the original paper. However, we also have fit *N* to experiment. The overall fraction of oxide at the top of the mixing layer, F_0 , is given by Malucci's formula [ref. 41, Eqn. 41].

$$F_{0,i} = 1 - \left(1 - \frac{t_i}{h_i}\right)\left\{\frac{\left(1 - \frac{t_i}{h_i}\right)^2 + 3\left(\frac{a}{h_i}\right)^2}{1 + 3\left(\frac{a}{h_i}\right)^2}\right\} \approx t_i / h_i \ , \tag{91}$$

which is essentially equal to t_i / h_i (with the additional terms due to his attempt to take into account of the finite size of each asperity [Eqn. 5, ref 41]). The value t_i is the corrosion film thickness for the i^{th} asperity, the calculation of which is described below. The value of h_i is the deformation of the particular asperity, i.e., the amount of "overlap" that occurs when the surfaces are contacted. Eqn. (91) may be derived by integrating Eqn. (90) over the mixing region to yield the total amount of oxide, which must equal t_i.

$$\int_o^h F(y)dy = F_o h = t_i \tag{92}$$

Finally, the fraction of the surface which is covered by oxide may be determined from Eqn. (90) to be

$$X_i = F_{0,i}(N+1)/(WipeFactor) \tag{93}$$

WipeFactor, which has a default value of 25, is a factor we have added to account for the reduction in the covering corrosion films due to a wiping motion of the contact. It is this quantity that is used in Eqn. (86) to calculate the resistance in the i^{th} asperity. In obtaining F_o a statistical value of h_i is obtained from the following formula

$$h_i = 2I(P[0,1]) . \tag{94}$$

Resistance from the film term, $R_i^{spot\_film}$, was used by Malucci in references [43] and [49] to account for large resistances (0.01 to 0.1 ohms observed in systems with aged non-metallic metals) observed in some systems. In Eqn. (87), σ_i is the film resistivity for the i^{th} asperity, while A_i is the area of the i^{th} asperity.

We relate the film resistance for the i^{th} asperity, σ_i , in Eqn. (87) to the calculated total corrosion film thickness, t_{corr} , by first translating the film resistance to a film thickness for the i^{th} asperity, $t_{film,i}$ and a corrosion film resistivity:

$$\sigma_i = \rho_{film} t_{film,i} \tag{95}$$

In Malucci's work, σ was statistically determined via a probability distribution between a low value of σ^L, based on the tunneling resistance σ^L and a high value σ^U. Equivalently, we use a probability distribution, $P_o^{\sigma_i}$, based on a hat function for the natural log of the film thickness, $t_{film,i}$ Eqn. (96), is used, because the resulting CPD function of the film resistivity is found to provide the best fit to experimental data.

$$\int_0^\infty P_o^{\sigma_i}(y)dy = 1, \quad P_o^{\sigma_i}(y) = \begin{cases} 4y & y < \frac{1}{2} \\ 4(1-y) & y > \frac{1}{2} \end{cases}, \; y = \frac{\ln(t_i) - \ln(t^L)}{\ln(t^U) - \ln(t^L)} \tag{96}$$

We use the numerically calculated t_{corr} to generate t^L and t^U via the formula,

$$t_{corr} = \left(t^U t^L\right)^{1/2} \quad . \tag{97}$$

by defining

$$t^L = \max(10\text{Å}, 0.28 t_{corr}) \text{ and } \quad t^U = \frac{\left(t_{corr}\right)^2}{t^L}. \tag{98}$$

We then use Eqn. (96) to calculate t_i, which is used in Eqn. (91) to calculate the fraction of the surface which is covered by metal, Eqn. (93). The resistance results are fairly sensitive to the multiplicative factor, 0.28, in Eqn. (98) . This factor determines the fraction of asperities which have a significantly lower corrosion product on them; these asperities are the ones that will predominately determine the resistance of the entire contact. We adjust t_i slightly before using it in Eqn. (95) to account for the deformation by reducing the predicted depth of the corrosion layer via the formula,

$$t_{film,i} = \max\left(t_i - \frac{h_i}{N+1}, 0\right), \tag{99}$$

which takes the reduction of the thickness due to the wiping deformation of the asperity contact into account. Eqns. (91), (93), and (99) also contains within them the reasonable assumption that there can not be metal-to-metal contact if the local interference of the asperity, h_i divided by the power law mixing exponent, *N+1*, is less the actual value of the corrosion film, t_{corr}^i, at the asperity.

Note, that for contact resistances above 0.005 ohms a very small percentage of contacts are due to direct metal-to-metal contacts. Therefore, the model formulation of the contact resistance through asperities covered with an unbroken interfacial corrosion film becomes the significant issue. For this film resistance model, the contact resistance is roughly dependent on the actual contact area. And, from Eqn. (77) and Eqn. (89), the actual contact area is inversely dependent on the load.

The resistivity of the corrosion film, ρ_{film}, is an important parameter in the above formulation. Both cuprous oxide, and copper sulfide have significantly small resistivities, and shouldn't be considered as insulators at the film thicknesses encountered. Both may be considered as p-type semiconductors whose resistivities are variable and temperature dependent,

but typical room temperature numbers are 100 and 10^{-2} Ohm cm for cuprous oxide and copper sulfide. ρ_{film} is an input to the model.

5.2.1 Taking Large Blooms into Account

In order to derive the contact resistance model, we first divide the calculated bloom distribution into small and large blooms. The total volume of small blooms is assumed to comprise a uniform surface corrosion product layer and is used as input to Malucci's model. If a bloom occupies an area larger than a fraction, *f*, of the Hertzian contact area, then the effect of the bloom is treated in a different manner. These blooms will exclude part of the contact area. The bloom fraction cut off, *f*, is an adjustable parameter in the model, nominally set to 0.2. This choice of *f* reflects bloom population in a subset of "small" and all of "medium and above" categories. If the bloom area exceeds *f*, then parts of the Hertzian contact area will be unavailable for direct contact except via conduction through the corrosion product bloom due to steric hindrance.

We apply a Monte Carlo approach to randomly sample the population distribution of large blooms on the surface to see if a probe has landed on a bloom. When the probe lands on a large bloom, heuristic rules are applied to quantify its impact to the overall electrical contact resistance. To take the halo region into account, each "large" bloom excludes an area equal to a factor of *haloExclusionFactor* times its own area from forming an electrical connection; this added correction where of *haloExclusionFactor* is nominally set to 4, an effect which we attribute to the creep corrosion around each bloom, i.e., the halo effect, is needed to fit experimental data.

The statistical procedure is carried out in the following way. The Hertzian area of the contact, A_{Hertz}, is broken up into a 10 x 10 grid. First, we look over each bin in the binned normalized probability distribution for blooms (see Figure A-1) at the current time. From this distribution and the overall number density of blooms at the current time, N_{blooms} we calculate the number density of blooms in the j^{th} bin. N_{blooms}^{j}, which has units of # per cm^2. We then roll a dice $P[0,1]$ for each block in the grid to determine whether a bloom of that size is centered in that grid box. Assuming Poisson statistics, the normalized probability for this to occur one or more times is equal to

$$P = 1 - \exp(-\theta) \qquad \text{where } \theta = \frac{N_{blooms}^{j} A_{Hertz}}{100} \ . \tag{100}$$

We then mark a block of grid boxes, equal to the size of the bloom, around the center grid box as being covered by the bloom/halo and therefore unavailable for the asperity based contact discussed in the previous section. We treat the boundaries of the 10 x 10 grid as being periodic. So, if a bloom center appears on the edge of the 10 x 10 grid, it blocks grid points on the other side of the grid also. If the bloom is larger than the Hertzian area, as is often the case when we add in estimates for the effect of the halo, we first go through the process of increasing N_{blooms}^{j} by a ratio of the bloom area to the contact area before rolling the dice in Eqn. (100) in order to not undercount large blooms. In effect we are creating an equal area of small blooms by this process.

The end of this process results in a percentage of the Hertzian contact area being blocked by large blooms. We add in conduction through the large bloom in parallel to conduction through the asperities, using the approximation:

$$R_{spots} = \frac{1}{\sum_{N} \frac{1}{R_i^{spot}} + \sum_{N'} \frac{1}{R_{BB}}} \text{ where} \tag{101}$$

$$R_{BB} = \frac{\sigma_{bloom}}{A_{bloom}} \quad , \tag{102}$$

and R_i^{spot} is calculated from Eqn. (84). R_{BB} is the resistance of current due to conduction through the excluded area of the contact created by direct contact of the probe with the bloom/halo. σ_{bloom} is the surface film resistivity of the bloom, estimated to be $\sigma_{bloom} = \rho_{film}(1\,\mu m)$, where $1\,\mu m$ is an estimate for the thickness of the halo region.

6.0 Experimental Procedures

6.1 Materials

For the aging experiments presented in this report, the coupons consisted of oxygen free copper coupons (UNS C10100) mechanically abraded to one of three surface finishes – 240 grit (Ra of 823 ± 126 nm), 600 grit (Ra of 262 ± 10 nm) or 1 micron diamond paste (Ra of 9 ± 2 nm). Once the desired surface finish was applied, each coupon was cleaned/degreased utilizing an alkaline cleaner, then pickled in a 10% HCl solution and sealed in a nylon bag. Next, the samples were shipped to a commercial electroplater (Nu-Metal Finishing in Santa Clara, CA) and an ASTM B488 type I (99.7%), Code C (Knoop hardness 130-200) bright gold deposit was applied utilizing industry standard plating procedures. The plating vendor cleaned the specimens again with an alkaline cleaner, followed by an acid dip in 25% HCl, then deposition of a copper strike followed by either gold or nickel and then gold.

In addition, the corrosion behavior and contact resistance of gold plated copper was examined with and without the presence of a nickel underplating. One set of coupons had 1.2 µm gold with no Ni underplating, while a second set of samples had a 1 µm gold with a nominal 2.5 µm Ni underplating

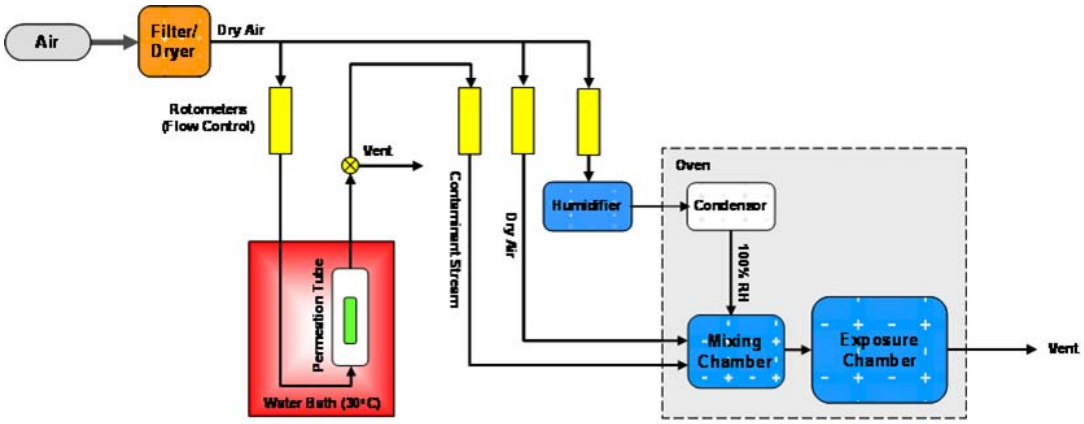

Fig. 37 GES Atmospheric Corrosion Testing Exposure System . Nominal operating conditions were10 ppb H_2S, 70% RH, and 30C.

6.2 Exposure Conditions

Samples were exposed to a specified gas composition using a Gas Exposure System (GES), illustrated schematically in Fig. 37. This system uses mechanically adjusted rotometers to control the flow of dry air, humid air (100% RH) and contaminant concentration to achieve a

well-defined gas stream. The contaminant (i.e. H_2S) was supplied via a commercially available permeation device that emitted H_2S at a known rate. A well defined flow rate of dry air was passed through a temperature controlled chamber containing the permeation device, resulting in a source stream of known contaminant concentration. While this system does not utilize a feedback control loop to maintain the composition within the system, the total surface area of active material within the exposure chamber was kept very small relative to the availability of moisture and gaseous contaminant, and as such it can be assumed that the flow rates of reactants were sufficiently large to prevent any significant loading effects within the chamber. Samples were exposed to a mixed flowing gas stream consisting of air containing 10 ppb H_2S at 30^{o}C and a relative humidity of either 70% or 10%. Samples were monitored periodically during the exposure period to document the size distribution of the corrosion product blooms, the number density of corrosion sites, and the electrical contact resistance of the aged surface.

6.3 Electrical Contact Resistance Measurements

Contact resistance data was collected using manual and automated techniques. All measurements were made using the four-point probe method and a Keithly Model 580 micro-ohmmeter in dry circuit mode (the maximum source voltage is 20 mV) at the lowest available current range, 100 mA. Both techniques also utilized a 3 mm diameter hemispherical gold plated copper-beryllium probe and a Honeywell Sensotec load cell with a range of 0-250 grams. A single set of measurements were obtained from each such area, and no region was evaluated more than once (i.e., each resistance measurement was made on a portion of the surface which had not been previously tested).

For the manually acquired data (including the 2004 data set), resistance measurements were made at 30 random sites within a predetermined region of each sample utilizing an applied load of nominally 30g.

In 2007, a LabView 8.2 program was developed to take advantage of the Newport Corporation high-precision linear stages (X,Y and Z) used for the contact resistance platform and integrate the stages with the micro-ohmmeter and load cell. The program executes a slow velocity Z-scan which raises the sample/stage through a short vertical distance where it comes into contact with the stationary probe. The start and end point of the scan can be selected to obtain contact resistance data over a range of loads (e.g. 0 to 100 g). The X and Y stages can also be controlled to provide mapping capability on the sample. For the data shown in this report, a scan rate of $2x10^{-4}$ mm/s was used, which for a load range of 0 to 100 g, results in a total scan time of approximately 1 to 2 minutes. Data has also been collected at slower scans rates of $2x10^{-5}$ (10 minute scan) and $2x10^{-6}$ mm/s (1 hour scan). Preliminary results for these scans (data not shown) indicate that slow scan rates, which would allow for a greater relaxation time, do not significantly change the measured contact resistance. The program automatically generates and saves an ASCII output file that includes the scan time in seconds, x and y position, load and resistance.

For most of the data sets, a single point contact was made for the contact resistance measurement. In a separate set of experiments to collect baseline (pre-exposure) data, the sample was brought into contact with the probe and then wiped across the surface over a distance of 2.5 mm under an attempted nominal load of 30g.

7.0 Results

In this section we will first show results from attempting to match a 2004 data set for the electrical contact resistance of a 1.2 μm Au plated copper sample using the 2005 numerical model. This exercise provided validation for the basic premise behind the pore corrosion model for describing the electrical contact resistance. The exercise demonstrated that you could match the pore size distribution function, both in terms of the number density of blooms, Fig. 28 containing numerical and experimental data, and the normalized size distribution of blooms (see Fig. 29 containing the experimental data and Fig. 31 containing the numerical data) while at the same time roughly matching the trends in the resulting electrical contact resistance (see Fig. 38).

Differences between the numerical and experimental results provided a task list of areas where additional information was needed such that a better understanding of the system could be established, and the model adjusted accordingly. The results of this analysis, which focused primarily on evaluating the contact resistance measured for an unaged surface (i.e., no exposure to an H_2S containing environment), is presented later in this section. Section 7.4 then presents results of matching more recent experimental data with the current numerical model.

Fig. 38 shows the experimentally observed electrical resistance data for the 2004 tested coupons. At each time interval, a series of 30 resistance measurements were taken on each sample as described in Section 6. As shown in the figure, there is an appreciable tail associated with each cumulative probability distribution after the first week, indicating that the few large-size blooms contribute to the most resistance increase in the population. The median resistance value remains relatively unchanged throughout this study. While a notable increase is observed in bloom density, as shown in Fig. 29, the tail in the distribution does not increase beyond five weeks. The apparent restriction of the corrosion product blooms to a certain size (i.e., the size of large blooms does not appear to continually increase with time) is likely the result of the experimentally observed corrosion site passivation process discussed in Section 4.3.

The 2005 simulation results are overlaid upon the experimental data. Table 5 summarizes the constants used for the simulations. Due to the large number of constants in this model, we have combined some from the literature and some determined by fitting the modeling results to our earlier experimental bare-copper coupon studies described in Section 3.5. From this comparison study arose several key points regarding modeling sensitivities. In order to match the total bloom site density distribution provided in Fig. 28, the total pore site density input into the model, M_0^d, and the initiation rate, λ, (note the values of M_0^d and λ are highly correlated) had to be adjusted to obtain the magnitude measured from the experiments. The upper and lower pore size limits, r_{pore}^U and r_{pore}^L, input to the numerical model then determined the final distribution of electrical contact resistances; r_{pore}^U and r_{pore}^L were fit to both the pore size distribution, Fig. 31, and to the experimental contact resistance. The final upper and lower pore sizes differed by a factor of 43, and their values were tightly constrained by the requirements of fitting both the pore distribution and the final contact resistances.

However, at the end of the process, we found that the film contribution from small blooms raised the ECR distribution in the entire population as the coupon ages, which is not what was observed in the experiment. Hence, either we overstated the contribution of small

blooms in our simulations even though the bloom cut off fraction is only set at 0.01, or there was some other systematic effect that was not being accounted for. In addition, to reproduce the large tail in the CPD electrical contact resistance, we had to increase the effective geometric interaction area of large blooms by adding in the presence of "halos" in the blooms. These halos have been shown to increase electrical contact resistances [32].

Table-5 Key model parameters used for the calculations

Sub-model	Value	Source
Growth Kinetics	$A_1 = 2.0\times10^{8}\, cm/\sec$ $A_{-1} = 4.2\times10^{3}\, cm^4/mol/\sec$ $A_2 = 2.0\times10^{2}\, cm^4/mol/\sec$ $E_1 = E_2 = 6.3\, kcal/mol$ $D_v = 7.0\times10^{-9}\, cm^2/\sec$	Adjusted to fit bare coupon data [11]
Pore Density & Distribution	$M_0^d = 3\times10^4,\ r_{pore}^L = 0.07$ $r_{pore}^U = 3.\ \mu m$	Adjusted to fit Fig. 28 and Fig. 29
Initiation and passivation	$\lambda = 1\, cm^{-2}\sec^{-1},\ \beta = 0.03$	Adjusted to Fig. 28 and Fig. 29
Material properties	$E_{Au} = 125\, GPa$ $H = 170x10^3\, psi$ $\rho_{Cu} = 1.7x10^{-6}\, ohm\ cm$ $\rho_{Cu_2S} = 1.0\, ohm\ cm$	[41]

Comparing the results from the simulation with experimental data, it can be seen that the model roughly predicted the ECR for the first week. Beyond that time, the increase in resistance due to growth of the corrosion product film and blooms surpasses the experiments, yielding distributions higher than observed quantities. One positive point however, is that the predicted high-end tail of the numerical distribution roughly corresponds to the high-end tail of the experimental distribution. In other words, while we were getting the 50% CPD trend wrong, we were matching the trends in the high-end CPD curve.

The failure to match the time dependence was partly due to the initial conditions that we had to assume in order to match the zero time baseline contact resistance, and therefore this issue brought us to understand that we needed to look more closely at the baseline data, i.e., the cumulative probability distribution one obtains on Au-plated copper before sulfidation actually begins. The thinking emerged that if we can't understand and model the zero time behavior, then modeling the late time behavior after sulfidation occurs is problematic and necessarily not as rigorous as it needs to be.

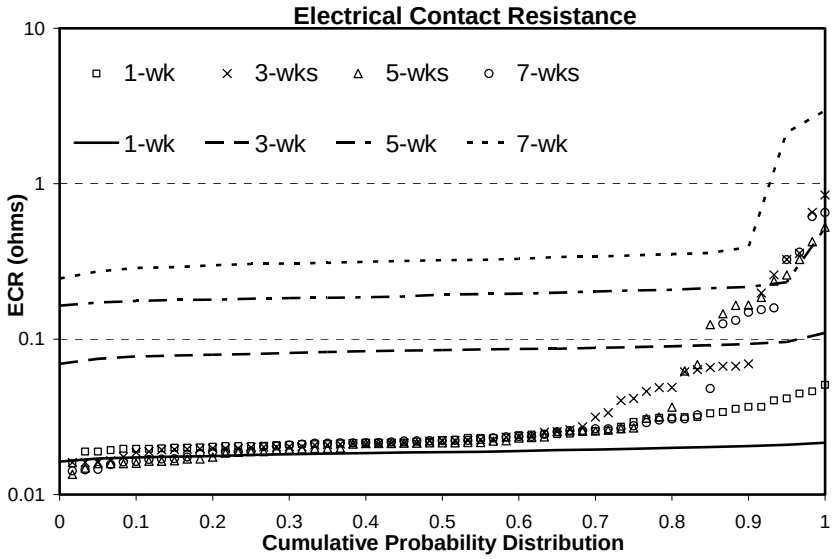

Fig. 38 Electrical contact resistance for 1.2 μm coupons. Data points are experiment. Lines are predictions from the initial model.

7.1 Matching Baseline Data

On looking at Fig. 38, we observed several problems with matching the initial distributions. As a baseline before corrosion even occurs, we would like to make sure that the CPD curve for the experiment and modeling can match. Additionally we would like to make sure the match extends to trends that involve changing the applied load. The model must be able to capture the electrical properties of an unaged interface (i.e., prior to the onset of sulfidation) in order to establish the proper baseline. Fig. 39 contains more recent data on the CPD curve for the baseline contact resistance of 1.2 micron Au-plated copper (no Ni underplating, 600 grit). Essentially, the experimental results have not changed; there is a large plateau region in the baseline around 0.01 to 0.02 ohms and there exists a tail region in the CPD region, as well, even though there is by definition no corrosion product on the coupon at this point. Note, if the probe is not cleaned, then there certainly could be corrosion product present, on the probe – similarly, there could be dust or other debris on the surface which could yield the large resistance tail to the distribution.

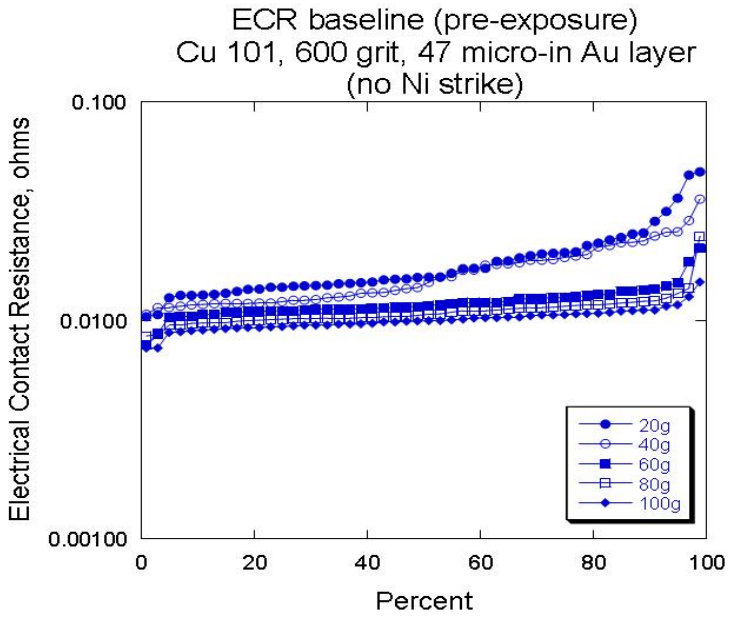

Fig. 39 Typical experimental CPD curve for the baseline data as a function of load applied. Sample was 1.2 μm Au on Cu (600 grit) coupon.

The first issue to tackle is the total absolute value of the baseline resistances. We will demonstrate that the contact resistance to be expected from metal-to-metal contact are actually at least an order of magnitude below the nominal value of 0.02 Ω indicated in Fig. 38, and while there is surprising scatter in literature data with little actual comment or discussion of the issue, many researches have obtained contact resistance data in the 0.001 Ω range or lower on clean systems.

The formulas for electrical contact between a probe and a plate (see Section 5.2) may be simplified greatly if there are no corrosion films. The following equation may be used:

$$R_{ECR} \equiv R_{spots} + R_{\text{int}}$$

where

$$R_{\text{int}} = \frac{\rho}{D} \qquad \text{and} \qquad R_{spots} = \frac{1}{\sum_{N} \frac{1}{R_i^{spot}}}$$

The resistance of each asperity may be greatly simplified when there is metal-to-metal contact so that the following formula is applicable.

$$R_{ECR} \equiv \frac{\rho}{D_n} + \frac{\rho}{nd_i} = \frac{\rho}{D_n} + \frac{\rho}{n^{1/2}\left(\frac{A_r}{A_n}\right)^{1/2} D_n} = \frac{\rho}{D_n}\left(1 + \left(\frac{A_n}{nA_r}\right)^{1/2}\right) \tag{103}$$

n is the number of asperities. A_n is the nominal contact area given by the Hertz formula. A_r is the actual total contact area, which can be obtained by summing up all of the individual contact areas, d_i from the *n* asperities. In Eqn. (103), we have used the following formulas.

$$A_n = \frac{\pi}{4} D_n^2 \qquad A_r = n\frac{\pi}{4} d_i^2$$

At least the first part of Eqn. (103) is quoted in numerous places (e.g., ref [42]) and stems from Greenwood's original formula. The second part is my manipulation to demonstrate the constitutive parameters that must be supplied to provide a quantitative result for Eqn. (82). The Hertzian diameter is approximated by the following simplified form of Eqn. (69).

$$D_n = 2.2\left(\frac{FR_{probe}}{E}\right)^{1/3}, \tag{104}$$

where *E* is the elastic modulus of the contacting metal, and R_{probe} is the radius of the probe, and *F* is the force on the probe. A typical value of *E* for gold is 125 GPa. Thus, with a probe radius of 0.15 cm and a contact load of 50 gm, the nominal contact diameter may be calculated to be 39.7 μm or 39.7×10^{-4} cm. Now, these numbers combined with a resistivity value obtained by averaging copper and gold resistivities,

$$\rho = 1.7\times10^{-6} + 2.25\times10^{-6} = 1.975\times10^{-6} \text{ ohm cm},$$

yields a value for the geometric contact resistance, R_{int}, of

$$R_{\text{int}} = \frac{\rho}{D} = \frac{1.975\times10^{-6}}{39.7\times10^{-4}} = 5.0\times10^{-4} \text{ ohms}. \tag{105}$$

Eqn. (105) effectively puts a floor on the lowest possible resistance for a given probe size. Then, the two constitutive models for *n*, the number of asperities, and A_r / A_n, the ratio of the actual contact area to the nominal contact area, determine the actual contact resistance value, which is higher than Eqn. (105) but not by much.

We may use Eqn. (77) to simplify Eqn. (103) further and obtain representative numbers for the relative sizes of the two terms in Eqn. (103). *P* is equal to the force divided by the nominal contact area given by the Hertz formula. Let's go through a calculation for a 50 gram load:

$$P = \frac{F}{A} = \frac{(50gm)\left(980\frac{cm}{\sec^2}\right)}{\pi\left[39.7\times10^{-4}\right]^2} = 0.1\,G\text{Pa}$$

From Yovanovich [50], the microhardness is typically 3 to 4 times larger than the bulk hardness of a material. Typical values of microhardness for metals and steel are 3-4 G Pa. Therefore, typical values of A_r / A_n is 0.025.

Typical values of *n* are a couple of hundred (see Fig. 36). The functional dependence of *n* is dominated by the value of the ratio of the surface roughness to the mean absolute asperity slope. This is true for both Malucci's treatment and for Yovanovich's treatment [50]. If *n* is a couple of hundred or even 10, then the second term in Eqn.(103) will not be larger than the first term for our operating conditions.

The 0.02 to 0.1 ohm resistances that the Sandia data exhibits are outliers in terms of what is normally reported in the literature. Below is a sampling of literature values for unaged contacts. All of them are significantly below the Sandia values. No reports of unaged contacts with resistances above 0.01 ohms were found. Most reported resistances are at least a factor of 10 below the Sandia numbers. Below is a bulleted list of representative numbers for contact resistances for unaged contacts:

- (Takanao and Mano, 1968 [51]) have the following value in their Fig. 3 and Fig. 4 plots on p. 52 for the contact resistance as a function of load: (copper wire on copper wire)
  50gm 0.0008 to 0.0015 Ohms
  200gm 0.0008 to 0.001 Ohms
  (Note, they go through a cleaning procedure and a roughening procedure to about 0.2 micron CLA.
- (Abbott 1978 [52]) have the following value displayed in their Figure 6 for an electroplated Au on silver cross-rod system.
  10gm 0.002 – 0.004 Ohms
- (Antler, 1996 [53]) displays the following range of values in their Fig. 3, 7, and 8 for a cumulative probability distribution plot of an unaged contact
  50 gm 0.003 – 0.007 ohms (hard to be precise about these numbers)
- (Abbott, 1987 [54]) displays a CPD lot for his unaged contacts in his Fig. 3, obtained with a gold probe with a radius of 0.16 cm:
  100 gm 0.0013 – 0.002 ohms
- (Martens, Pecht 2000 [55]) present a comprehensive treatment of the unaged electrical contact resistance. They report data for a range of loads for two different probe diameters, 1.0 mm and 6.36 mm (ours is 3.0 mm). For the smaller probe diameter they obtain:
  25 gm 0.0029 - 0.0045 ohm
  50 gm 0.0020 – 0.0030 ohm
  75 gm 0.0014 – 0.0022 ohm
  For the larger probe they obtain:
  25 gm 0.0053 - 0.0065 ohm
  50 gm 0.0039 – 0.0048 ohm
  75 gm 0.0031 – 0.0039 ohm
- (Law et al., 1991 [56]) obtained the following contact resistances on their unaged Nickel/phosporus plated surfaces:
  10 gm 0.002 – 0.0025 ohm
  20 gm 0.0015 – 0.0020 ohm
  50 gm 0.001 – 0.0011 ohm

- (Malucci 1995 [43]) has one plot of a CPR for the ECR of an unaged contact, Fig. 10. Gold on Gold results produced
  100 gm 0.0011 – 0.0019 ohm
- In (Malucci 1993 [41]) and (Malucci 1999 [57]), there are multiple figures of CPD curves for unaged contacts. All of these start with having low values in the 0.001 to 0.002 ohm range. There are even some points below 0.001 ohms (0.0004 ohms in his Fig. 6).

Given the literature study and numerical support for the expectation of a much lower electrical contact resistance from metal-to-metal contact, we undertook to understand our results more by carrying additional experiments. We also developed of an automatic way to sample the contact resistance at a series of different loads on the probe, enabling us to generate a lot of data. The load dependence is a crucial tool for understand the physical mechanism behind the contact resistance.

Fig. 40 and Fig. 41 contain results form an attempt to model baseline results from a 1.2 μm Au plated copper sample run, whose data is plotted in Fig. 41 also.

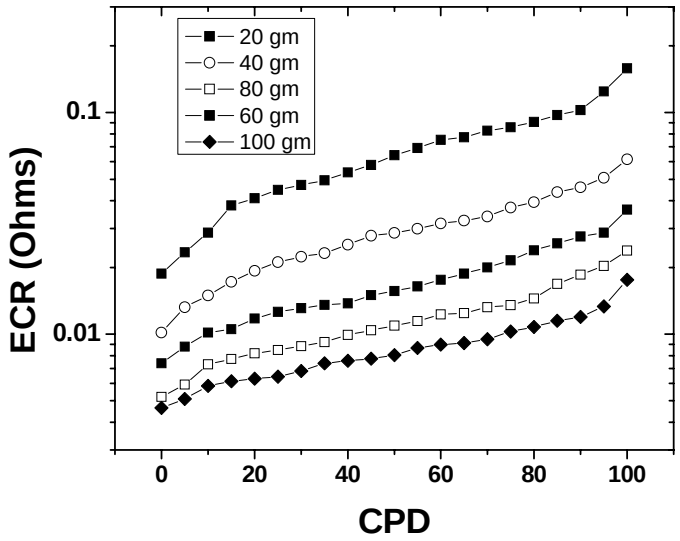

Fig. 40 Numerical model's CPD curve for the baseline. `mdivh0` = 1.094E4, `Contact Surface Roughness` = 2.6E-5 cm, `Mixing Power Law Exponent` = 13, `minimum corrosion film thickness` = 2.2E-6, `Corrosion film resistivity` = 0.19

The figure caption in Fig. 40 contains some of the input parameters that were necessary to model the experimental data in Fig. 41 (see Appendix A for a complete definition of these parameters) . The goal was to fit the experimental points at a load of 30 gm, while attempting to do the best we could at the other loads. In order to fit the absolute magnitude of the electrical contact resistance, we had to postulate the existence of an initial corrosion layer that was a significant fraction of the

assumed surface roughness, such that most of the metallic contact within the contacting asperities was blocked.

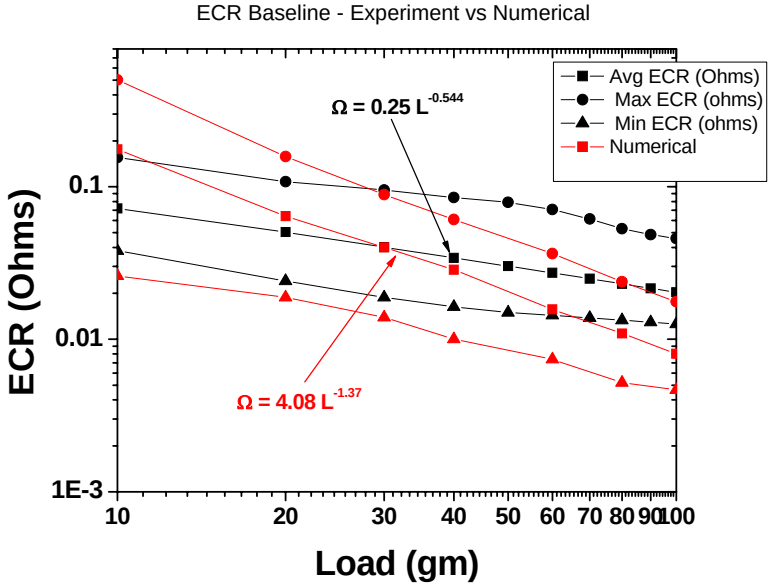

Fig. 41 Numerical vs experimental. Experimental data from the baseline raw data_10RH_1.2 um Au-2 run 8/2007

When we did this, however, the model produced an ECR dependence on the load that was greater than $L^{-1.0}$. This parameter regime is indicative of a varying amount of metal-to-metal contact, and has been seen by other researchers such as Malucci [41] and Timset [58] when making contact to aged surfaces with significant corrosion product layers. . Malucci modeled that scenario assuming a varying fraction of metal-to-metal contact, similar to what we have done using Eqn. (86). The basic problem is that the experimental data has a $L^{-0.5}$ dependence, and as previously shown, this is indicative of metal-to-metal contact in unaged contacts.The absolute ECR, however, is far higher than the value obtainable from metal-metal contacts.

The numerical model has a $L^{-1.3}$ power law dependence at this high an ECR value, and the results cannot be changed. In fact, a $L^{-1.0}$ dependence has frequently been used as an ad hoc indicator of contamination on the surface layer (see Timset [58]). The $L^{-1.0}$ dependence may be derived from Eqn. (87) assuming that all asperities have unpunctured interfacial contaminant films, resulting in

$$R_i^{spot\_film} = \left(\frac{\sigma_i}{A_i} + \frac{\rho}{d_i} \right) \tag{106}$$

Assuming there are *n* equal asperities, then

$$R_{ECR} = R_{\text{int}} + R_{spots} = \frac{\rho}{D} + \frac{\sigma_i}{nA_i} = \frac{\rho}{D} + \frac{\sigma_i}{A_r} \tag{107}$$

Then, using Eqn. (77)

$$R_{ECR} = \frac{\rho}{D} + \frac{\sigma_i H}{A_n P} = \frac{\rho}{D} + \frac{\sigma_i H}{F} \tag{108}$$

If the resistance is dominated by the second term in Eqn. (108), then the resistance will be inversely proportional to the load and proportional to the interfacial contact resistance, σ_i

What this boils down to is that beyond 0.002 or 0.003 ohms for our particular parameter regime, the contact resistance must be dominated by a corrosion product layer, or surface film effects. The physical parameters don't offer any other solutions. The numerical model adds this interfacial film resistance, and gets the $L^{-1.3}$ power law dependence expected for the film resistance (it's greater than 1.0 due to the fact that there is enhanced metal-to-metal contact as the load is increased). However, the experimental number has a contact resistance and a low $L^{-0.5}$ power law dependence. This combination cannot be replicated by the numerical model.

Therefore we undertook to understand why the electrical contact resistance was higher than the 0.001 Ω range and to understand how we could manipulate the conditions to get it lower. We attempted to understand cleaning procedures. We explored the effects of surface roughness. We tried adding wipe to the experimental technique. And we discounted the effects of conduction path lengths within the probe and the coupon due to an order of magnitude analysis and the effects of the "other" connection to the coupon needed to create the circuit for the resistivity measurement. The following sections explore results from these studies.

7.2 Surface Roughness: Baseline Model vs. Experiment

A key issue between numerical and experiment has emerged, that of the predicted numerical vs. experimental dependence between experiment and theory of the surface roughness. The main effect that surface roughness has is on the deformation of each asperity. The larger the surface roughness, the more each asperity deforms in the perpendicular direction for a given load; currently, this is modeled as a linear effect within the numerical code. The more each asperity deforms, the impact which any surface film has in terms of hindering metal-to-metal contact is reduced. Eqn. (91) is the main governing equation within the numerical model. In Eqn. (91), the fraction of metal-to-metal contact established is based on a direct ratio of the corrosion film thickness to the amount of deformation experienced within a single asperity, which in turn is linearly related to the surface roughness.

The numerical model may be analyzed for the dependence of its results on the input surface roughness parameter. The results are presented in Fig. 42. Two input corrosion film thicknesses are plotted in Fig. 42, one with 1.0E-7 and one with 7.0E-7 cm thicknesses (note the values were motivated by Auger-sputtering results presented later). The pre-plating specification on the copper surface roughness of 600 grit is indicated in the figure in blue for comparison purposes. For each curve a high and low parameter regime is indicated. For high surface roughness, the 1.0E-7 and one with 7.0E-7 cm corrosion-film thicknesses produce the same

average contact resistances, as the effects of the corrosion film are entirely mitigated by the large relative surface roughness. The high surface roughness values are limited by the Hertzian-constriction resistance. Metal-to-metal contact is achieved in the high surface roughness regime.

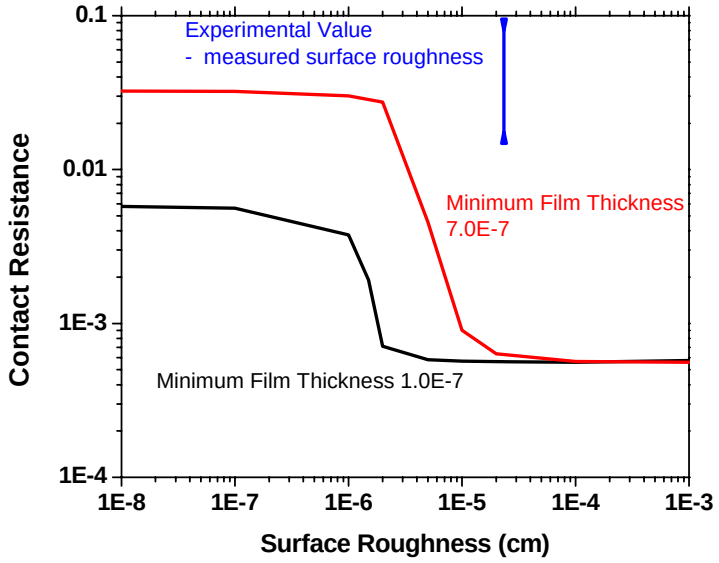

Fig. 42 Numerical model's prediction of the average contact resistance on the surface roughness for two different corrosion film thicknesses: 50 gm load assumed. Experimentally measured surface roughness is indicated in the plot in blue for reference.

At low surface roughness a higher plateau in the contact resistances is reached. The value of the plateau is a linear function of the corrosion film thickness multiplied by the assumed resistivity of the corrosion product, which we have set to 0.19 ohm cm in the figure. . Typical values for the resistivity of the corrosion film vary between 1000 ohm-cm for Cu_2O to 0.01 ohm-cm for Cu_2S. Given its uncertainty, this parameter should therefore be considered as a fitting parameter. In the low surface roughness plateau regime, the corrosion film is never punctured by the contacting process (i.e., direct metal-to-metal contact is prevented). The previous section contained an analysis of this regime and resulted in Eqn. (108), which employed an interfacial contact resistance, σ_i . That analysis holds for conditions on the lhs of Fig. 42. σ_i is equal to a statically evaluated corrosion film thickness, t_i , Eqn. (99), multiplied by the corrosion film resistivity. Note, the red curve is a factor of 7 higher than the black curve within low input surface roughness regime because the input corrosion film thickness is a factor of 7 higher.

As part of the process of understanding the baseline results, the polishing finishes on copper coupons was varied (prior to plating), and the type of noble plating was varied. Three different surface polishing grits were used in order of increasing smoothness: 240 grit, 600 grit, and 1 micron. Then, two surface plating morphologies were applied - in one case, a single layer of Au 1.2 microns thick was deposited. The second morphology included a nominal 2.5 micron

Ni layer beneath the 1.0 micron Au layer. In Fig. 43 , results from an optical interferometry analysis of the plated coupons is presented.

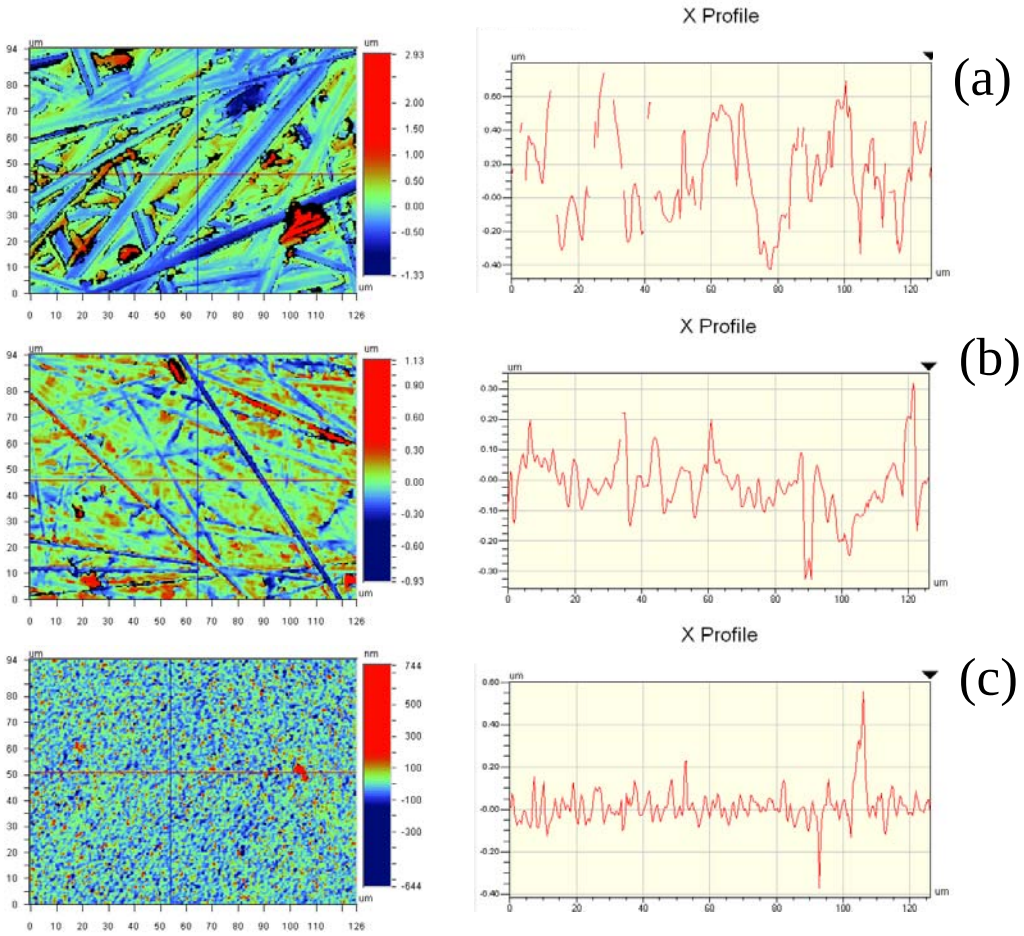

Fig. 43 Optical interferometry results on samples with different surface roughness preparations carried out on the bare Cu before electroplating : a) 1.2 micron Au on 240 grit; (b) 1.2 micron Au on 600 grit; (c) 1 micron Au on 1 micron

On the left side of Fig. 43 are pictures of the surface. On the right are profileometry results in the x direction. Table 6 contains the results of averaging the surface roughness of three 3 points on each coupon. It should be noted that the Au/Ni bilayers produced 15 to 30% rougher films for nominally the same copper-coupon surface treatment.

Table-6 Surface Roughness (cm)

1.2 micron Au on Copper			1 micron Au / Ni bilayer on Copper		
1 micron	**600 grit**	**240 grit**	**1 micron**	**600 grit**	**240 grit**
	1.08E-05	2.52E-05	4.40E-06	1.39E-05	2.51E-05
	1.11E-05	1.99E-05	4.50E-06	1.44E-05	2.60E-05
	1.09E-05	2.53E-05	4.80E-06	1.38E-05	2.27E-05
	1.09E-05	**2.35E-05**	**4.57E-06**	**1.40E-05**	**2.46E-05**

The coupons were tested for their electrical contact resistance as a function of load. The results are presented in Fig. 44.

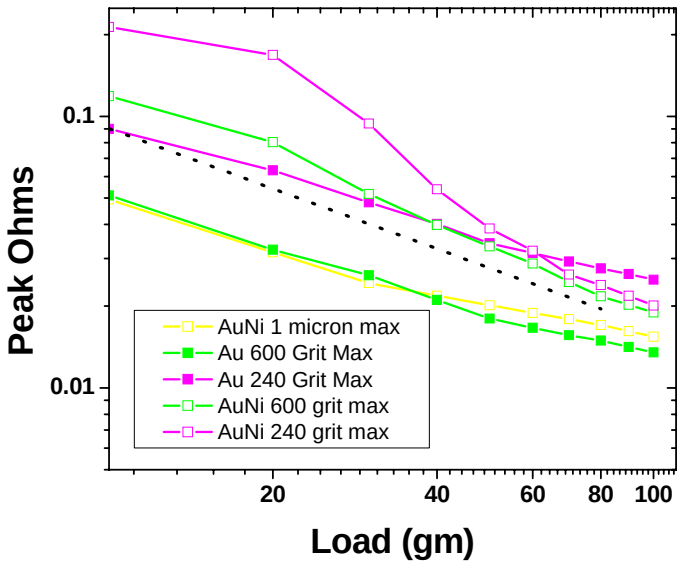

Fig. 44 Experimental measured peak contact resistances as a function of applied load for Au-plated copper and AuNi bilayer-plated copper. The bilayer consisted of 1 micron Au on top of 2.5 micron Ni on top of Cu. The dotted line is an $L^{-0.66}$ dependence for comparison.

The experimental results turned out to exhibit opposite trends from the numerical model. In general the more reduced the initial surface roughness was, the lower the contact resistance turns out to be. Also, for a constant initial surface roughness, the AuNi layers exhibited higher initial contact resistances than the single-layer Au plated samples. One might have expected the Au and AuNi layers to have the same ECR if the Au layer was deposited in the same manner, under identical electrochemical conditions. However, the AuNi layers had greater ECR. This trend

may be correlated with the increase surface roughness of the AuNi films over the Au films. In other words it could be that the AuNi films had larger ECR's because they had larger surface roughness values, but the results in Table 6 would need to be strengthened statistically.

What is evident is that even for the finest surface preparation of 1 micron polishing, all results are significantly greater than the < 0.001 ohm results dictated by the numerical modeling of clean surfaces. Therefore, none of the experimental results should be compared directly with the numerical results without taking into consideration the existence of systematic inaccuracies in the numerical model or equivalently the presence of unknown effects in the experiments. With the exception of the AuNi 240 grit sample, Fig. 44 indicates that most of the experimental data exhibits an $L^{-0.5}$ to $L^{-0.66}$ dependence on the load in agreement with the previous data of Fig. 41. This dependence is not suggestive of a surface film, as the analysis leading to Eqn. (108) indicates that these surface films have an $L^{-1.0}$ dependence. The $L^{-0.66}$ dependence is actually indicative of a geometric effect, i.e., the first term in Eqn. (108) if ρ could somehow be increased substantially (2 or 3 orders of magnitude from values characteristic of metals). Note, because the plating films are 1 micron and *D*, the Hertzian diameter, is on the order of 37 microns, this increase in the effective value of ρ may be achieved if there are unintentional buried barrier layers, for example due to inadequate cleaning of the native Cu oxide before the plating process. Assuming the presence of a series resistance due to an extra barrier layer results in the following formula modified from Eqn. (108):

$$R_{ECR} = \frac{\rho_{BL} L_{BL}}{\frac{\pi}{4} D^2} + \frac{\rho}{D} + \frac{\sigma_i H}{F} = \frac{\sigma_{BL}}{\frac{\pi}{4} D^2} + \frac{\rho}{D} + \frac{\sigma_i H}{F} \quad . \tag{109}$$

where ρ_{BL} is the resistivity of the buried barrier layer and L_{BL} is the thickness of the barrier layer. Turning Eqn. (109) around we may solve for L_{BL} given a resistivity of 1000 ohm cm characteristic of Cu_2O given a "needed" value of 0.05 ohms for R_{ECR}, a typical experimental

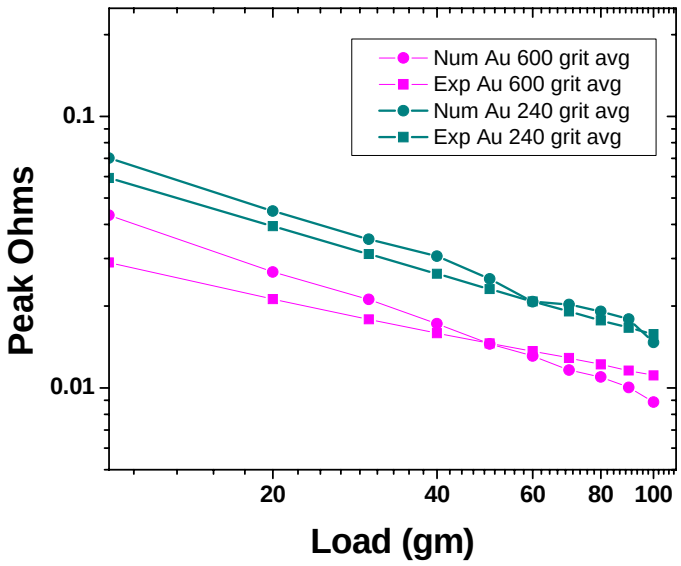

Fig. 45 Average contact resistance from experiment and the numerical model as a function of contact load for Au plated copper coupons

number. The result is $L_{BL} = 0.007$ nm, a submonolayer of Cu_2O value, which would certainly be easy enough to accumulate during the plating process. In Eqn. (109), we've replaced the barrier layer ρ_{BL} and L_{BL}, since the two are not separately identifiable: $\sigma_{BL} = \rho_{BL} L_{BL}$. Therefore, Eqn. (109) is a possible candidate for a modified theory, since it fits the experiment trends. In particular it fits the major trend with respect to the load dependence. Note, the barrier layer may exist either within the coupon, within the probe or within both. The fact that the ECR varies with coupon preparation, i.e., Fig. 44, indicates that the thickest buried barrier would be within the coupon.

The agreement in Fig. 45 demonstrates that Eqn. (109) does a fairly good job at representing the base case load dependence, though Eqn. (109) still over-represents the observed load dependence to some degree. The data are taken from the same coupons as those presented in Fig. 44. The numerical model was based on Eqn. (109) with surface roughness values input from Table 6. Initial corrosion film thicknesses of 7 nm were assumed. The 600 grit case assumed low and high values for σ_{BL} of 1.4E-7 and 2.0E-7 ohm cm^{-2}. The 240 grit case assumed low and high values for σ_{BL} of 1.8E-7 and 4.3E-7 ohm cm^{-2}.

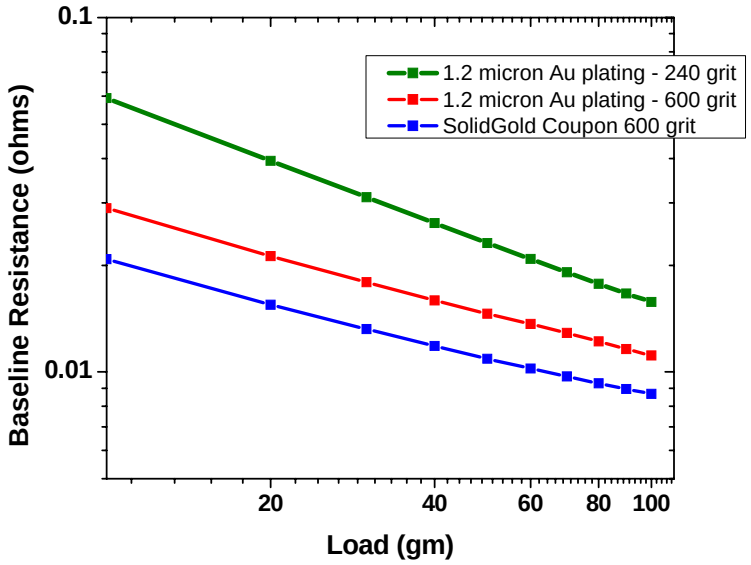

Fig. 46 Experimental averaged contact resistances as a function of applied load for a pure solid Au coupon compared with the previous Au-plated results. The solid gold coupon that was abraded to 600 grit, degreased, and then cleaned before the ECR measurement.

This discussion demonstrates that the plating process is not an innocent actor in the process, and may in fact provide the explanation for the disagreement between the numerical model and the experimental results. Recently we have carried out an experiment on a pure solid coupon polished to 600 grit. Fig. 46 contains the results, along with the previous Au-plating results for comparison. A significant decrease in the resistance is seen leading to at least partial but not conclusive support for Eqn. (109).

It should be noted that all of the data taken in Fig. 46 used the same Au-plated copper-bellurium probe. Therefore, it may be the case that much of the resistance is within the plating of the probe, a hypothesis that must await experiments with a pure gold probe which was not available to us. These preliminary results are inconclusive due to a lack of direct experimental support for the complete hypothesis, however, and it's clear that more experiments and attention must be focused on the plating process itself in the future.

Another possible issue might be the effects of surface films and surface preparation on the initial electrical contact resistance. Fig. 47 shows the results from an Auger sputtering analysis on a representative as-received Au-plated Cu coupon. A contamination over-layer consisting of hydrocarbons and possibly a Cu oxide was found on this coupon. The contamination layer was roughly 7 nm in depth. A UV ozone cleaning step was then added to the surface preparation, and the Auger sputtering analysis was redone. The final result, depicted in Fig. 47 (b) demonstrated that a 4 nm contamination layer persisted after the cleaning step.

(a) (b)

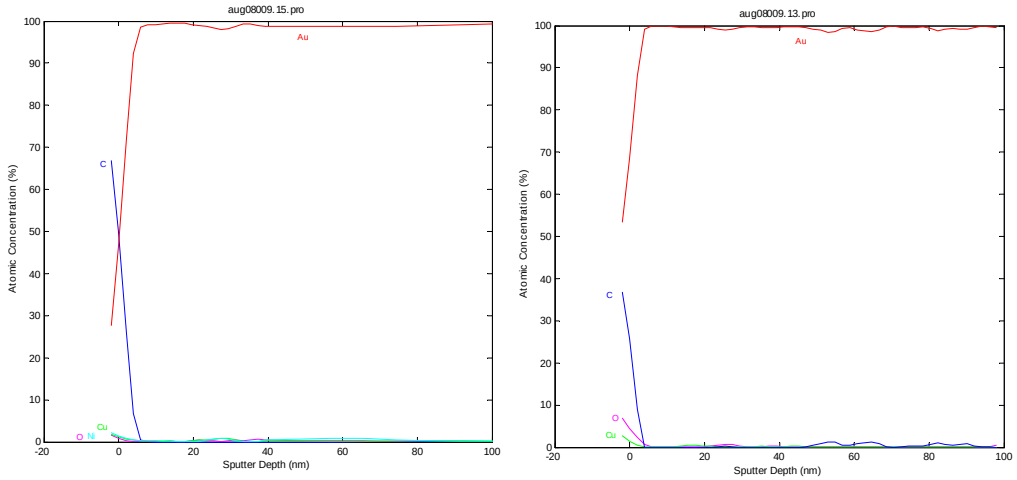

Fig. 47 A contamination over-layer consisting of hydrocarbons and possibly a Cu oxide was found on the as-received and UV ozone-cleaned samples. UV ozone cleaning did not completely remove the contamination layer: thickness of 7 nm for the as received sample and 4 nm for the cleaned sample. .

Fig. 48 exhibits the results of taking ECR measurements on the coupons before and after UV ozone cleaning. The minimum values in the CPD have not changed at all. However, the maximum values of the CPD curves are significantly decreased as a result of the UV ozone cleaning. In other words after cleaning the high end of the CPD curve was curtailed due to the cleaning, and therefore, the ECR measurement showed significantly less variability with a cleaning step than without it.

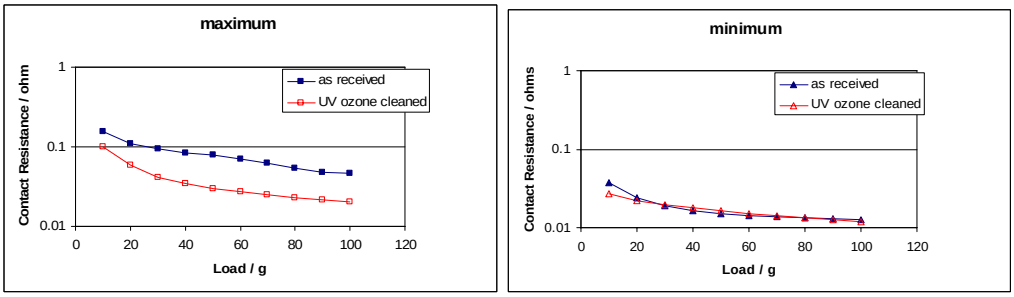

Fig. 48 The contamination layer contributes to an increased electrical contact resistance for baseline measurements. The clean samples exhibit lower peak values of ECR; minimum values of ECR are similar for as received vs. cleaned.

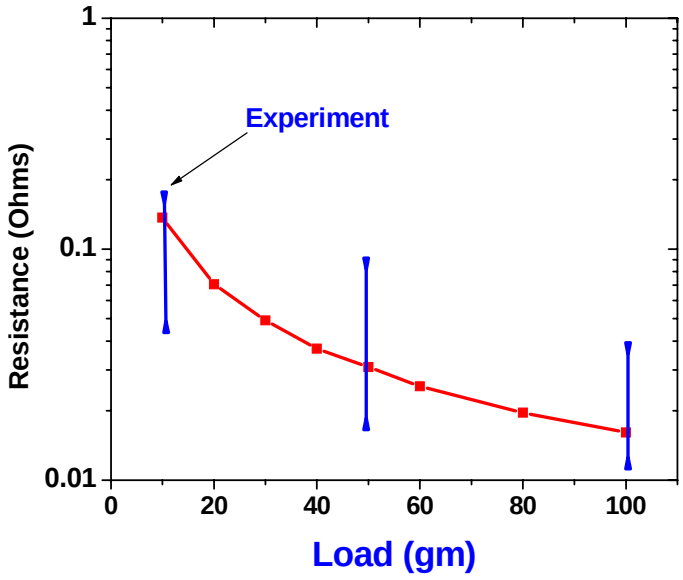

Fig. 49 Experiment vs numerical: Effect of surface roughness – assuming 1.0E-6 cm for the surface roughness Variation of the resistance with respect to the load on the probe is adequately captured by numerical model (red)

While the alteration in thickness of the surface film by the cleaning process may not be statistically significant, the contact resistance data presented in Fig. 48 suggests that the nature of the surface films can impact the measured electrical contact resistance. Fig. 49 demonstrates that the numerical model may be made to fit the experiments to an adequate degree if the numerical model is tweaked. The red line in Fig. 49 is from the 50% CPD numerical model with the surface roughness set to 1.0E-6 cm and a corrosion film thickness of 7.0E-7 cm assumed. The blue lines in Fig. 49 represent the bounds between the minimum and maximum measured ECR values. It's clear that the experimental data has less dependence on load than the numerical data does. However, the fit is somewhat adequate.

It seems clear that all terms in Eqn. (109) may be actually be applicable in practice. Both surface films and buried layers may be possible sources for the high baseline ECR measurements measured. It is not possible with the available experimental data to deconvolute the experimental data further.

Fig. 50 plots the effects of several parameters on the CPD. Fig. 50 (a) plots the results of changing the probe radius on the CPD. In agreement with Timsit [58], the effects of the probe radius are secondary. The reduced radius of the probe increases the surface pressure, creating a higher density of asperities with more interference, *I*, in each asperity.

(a) (b)

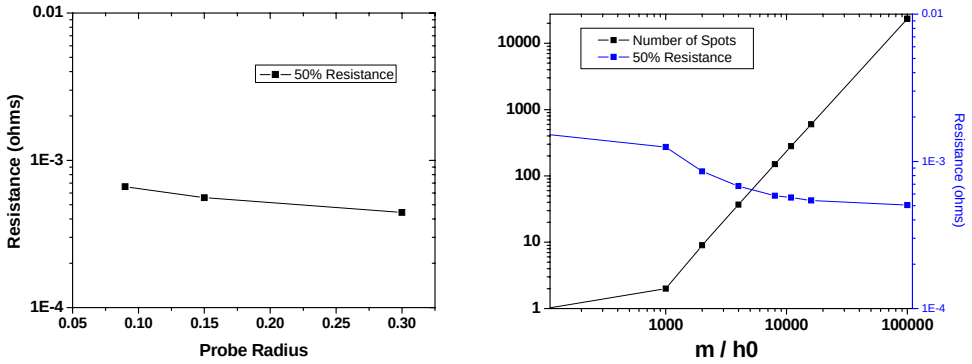

Fig. 50 Probe radius doesn't affect resistance much, in agreement with Timsit. The density of asperities does not matter until there are only 1 – 2.

In Fig. 50 (b) a key parameter m / h_o in the numerical model is varied over a large range. m / h_o controls the number of asperities per cm^2 of surface area. Fig. 50 (b) demonstrates that this parameter, which is relatively unknown, does not have a significant effect on the bottom line results until the number of asperities reaches the very low and physically unreasonable number of 5 or less.

7.3 Effect of Wipe: Baseline Model vs. Experiment

Most contacts, such as those that apply tines in a socket setup, work by applying both load and wipe during the contacting process. We've attempted to develop models within this program to account for the reduced experimentally verified reduction in the electrical contact resistance. Wipe affects the numerical model in two ways. The first way is the introduction of a wipe factor in Eqn. (93). This wipe factor has the effect of making more metal-to-metal contact for a given amount of corrosion film. The second effect is the inclusion of the wipe length multiplied by the Hertzian diameter into the formula for distinguishing between small and large blooms, Eqn. (64). When wipe occurs, the corrosion blooms have to be larger in order to exclude surface area.

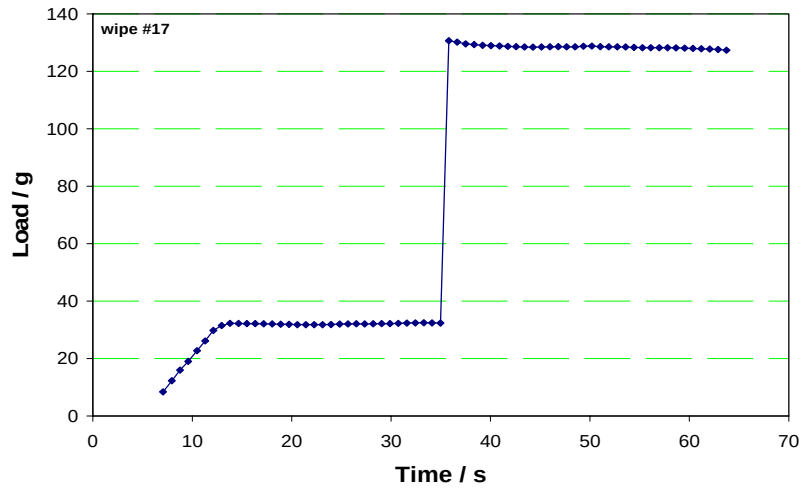

(a)

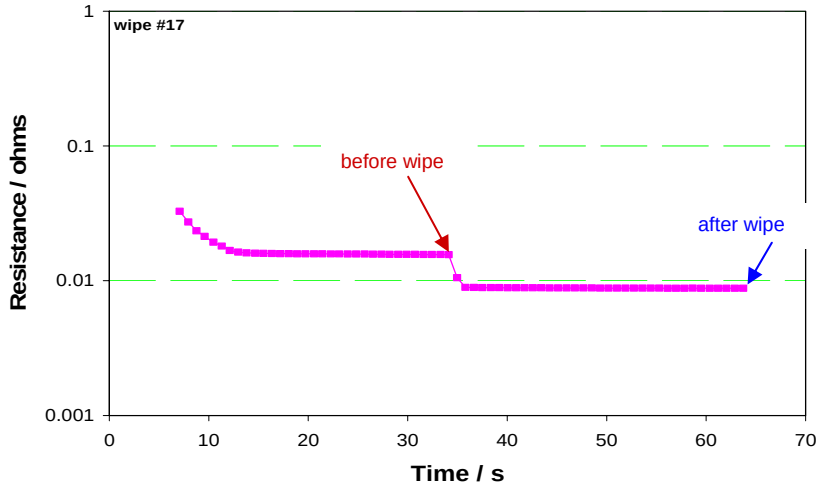

(b)

Fig. 51 The effect of wipe on the measured contact resistance.

Experiments were carried out with and without wipe. Scans with a wipe were carried out in the following way: the scan was initiated at a load less than 30 gm and increased in the +Z direction at a rate of 2E-4 mm/s until a nominal load of 30 gm was reached (this is referred to as "partial" automation). After a short relaxation time at 30 gm (approximately 30 seconds), the

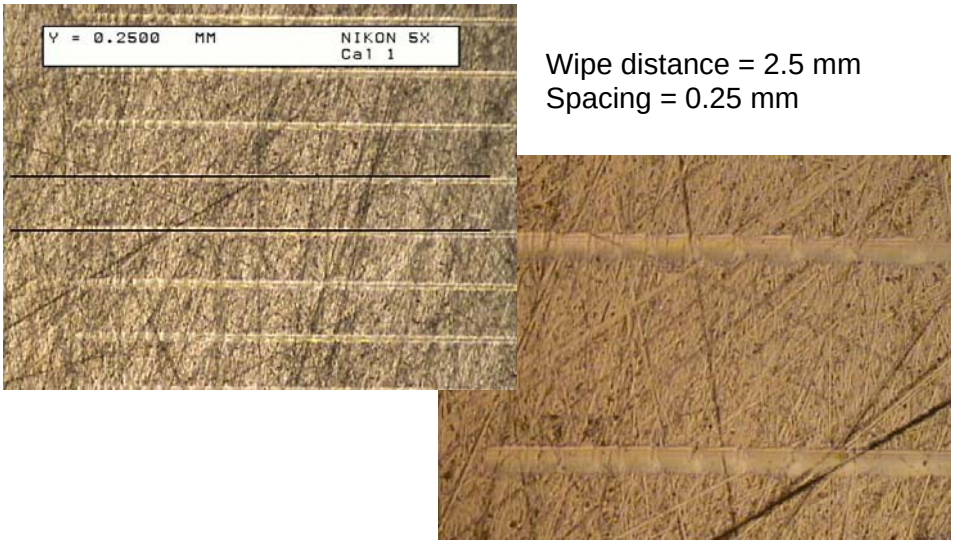

(a)

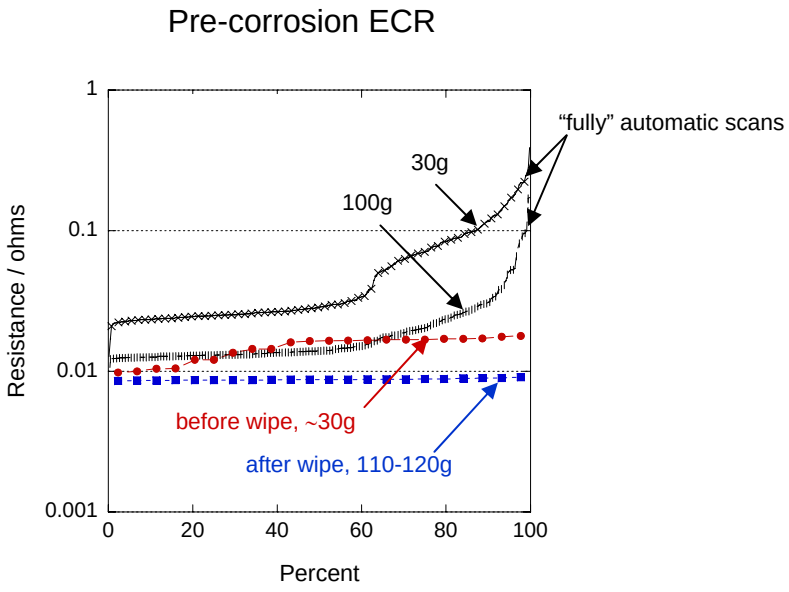

(b)

Fig. 52 CPD curves for wipe vs no-wipe: The wipe served to narrow the distribution significantly. Automation of scans affected the resistance results.

probe was moved in the +Y direction through a distance of 2.5 mm while still in contact with the sample surface. Fig. 51 (a) contains a recording of the load vs. time trace produced by this procedure. As soon as the wipe was initiated by traversing the probe along the surface under pressure, the measured load on the probe increased significantly. Therefore, wipe and load could not be varied independently from each other. Fig. 51 (b) shows that the ECR decreased by a factor of ~2. However, most of the decrease can be attributed to the increase in the load.

Fig. 52 (a) shows what a wipe trace of 2.5 mm looks like on a 600 grit copper coupon with a 1.2 micron Au plating. It is evident that significant damage to the baseline Au-plated surface occurs during a wipe. Fig. 52 (b) contains experimental results for the CPD curve for the case of wipe and no-wipe. Results are again fairly similar to no-wipe results with the equivalent load. As mentioned previously, the scans with wipe were partially automated and included relaxation times of ~30 s. This is compared to the "fully" automatic scans in which the entire load range of 0 to 100 gm was captured at a scan rate of 2E-4 mm/s, with effectively little to no relaxation time. Interestingly, the ECR at 30 gm measured by the fully automated scans is higher than the ECR at 30 gm measured by the partially automated scans and similar results are observed for the 100 gm ECR values. No resolution of this issue has been found.

7.4 Matching Data from Literature Sources

It has been mentioned that the contact resistance measured and reported in the literature is generally an order of magnitude lower than current Sandia experiments. We went through the exercise of actually modeling the results from one set of data [58] reported. Fig. 53 contains a demonstration that the numerical model can match representative literature data as long as the absolute contact resistance is low enough. Fig. 53 contains experimental results for a pure gold-on-gold system. The experimental dependence is roughly the $L^{-0.5}$ dependence required/predicted by the numerical method.

However, when we go to model the Sandia data, we can't do it, especially when we add in the dependence on load.

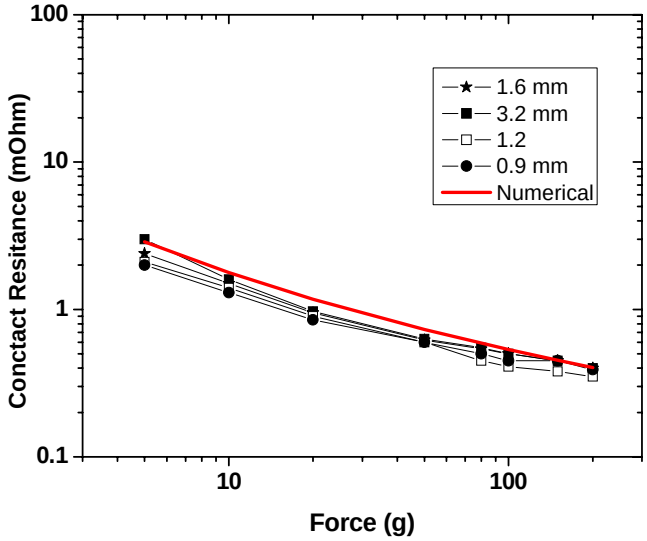

Fig. 53 Matching numerical vs literature experiment on gold-gold [58]

To model the results from Fig. 53, it was necessary to assume the existence of a corrosion film of 2.0E-6 cm with a nominal surface roughness of 5.00E-5 and a mixing power law exponent of 4. There was still significant blockage of the metal-to-metal contact at the asperity level in order to increase the contact resistance from the sub-milliohm level to the 1 milliohm-or-above level. However, the model can accommodate this, and does quite well.

Fig. 54 contains results from gold probe on pure “clean” copper coupon study also reported by Timsit [58]. The copper was cleaned just prior to the ECR measurement.

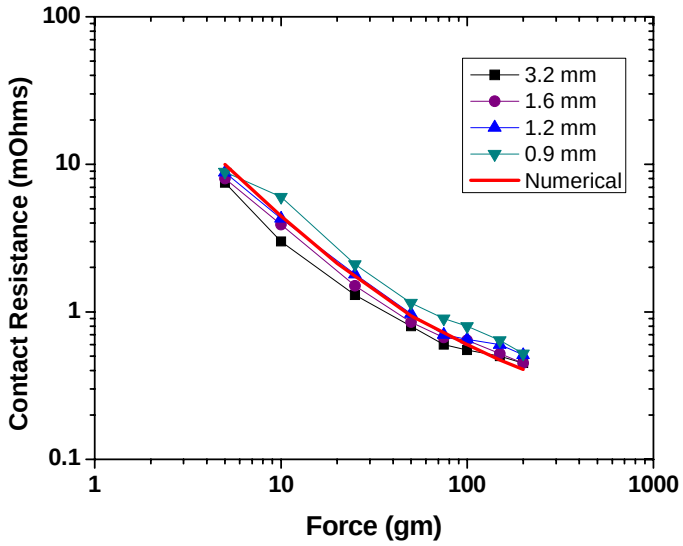

Fig. 54 Matching numerical vs literature experiment using a gold probe and a cleaned copper coupon with a copper oxide interface.

However, the copper grows a native oxide very quickly. The low load part of Fig. 54 clearly shows that the load dependence is L^{-1} in agreement with Eqn. (108). The numerical model can model the change from L^{-1} to $L^{-0.5}$ with load when the absolute contact resistance is in the 1 milliohm level. To model the results from Fig. 54, it was necessary to assume the existence of a corrosion film of 5.0E-6 cm with a nominal surface roughness of 5.0E-5 cm and a mixing power law exponent of 4.

7.5 Modeling the Evolution of Corrosion with Exposure

In the past sections we have attempted to study how well the numerical model can predict the baseline experimental cumulative probability distribution data as a function of load, wipe, surface treatment, copper polishing treatment, and plating treatments. We obtained mixed results that indicated there are systematic effects in the experiment that we don't yet have a good understanding of and that are therefore not included in the numerical model. Section 7.4 indicated that if those systematic effects were eliminated, we may do significantly better in matching the data. However, the main goal of the program was to model the evolution of the contact resistances as a function of the exposure to corrosive gases. In this section we attempt to use the model to match experimental results despite some of the current uncertainties.

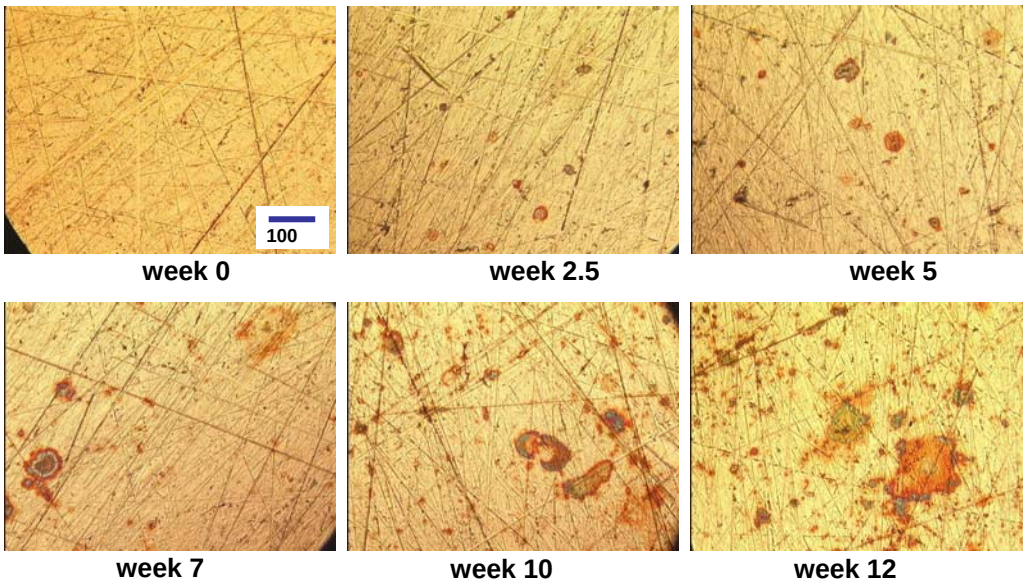

Fig. 55 Visual inspection of aged Au-plated coupons Samples shown: 1.2 μm ASTM-B-488 Type I, Code C Au on oxygen free copper. Pre-plating surface roughness (Ra) of 262 nm (600 grit finish))

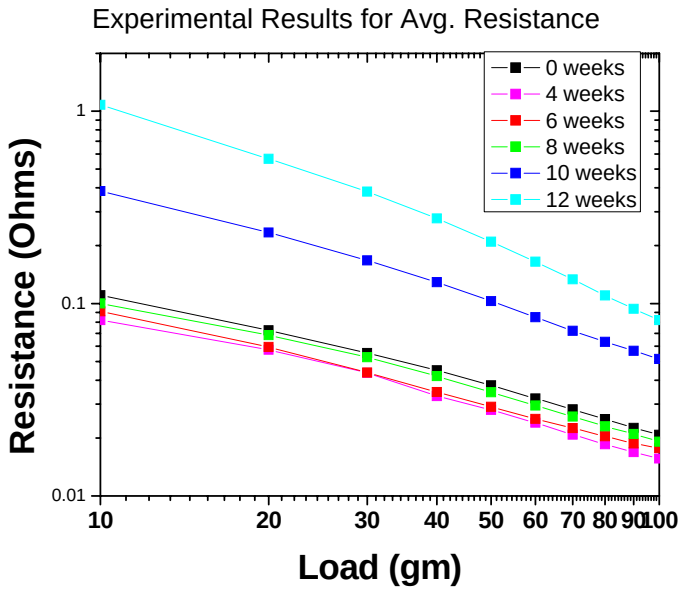

Fig. 56 Experimental results for the average resistance measured for a 1.2 μm ASTM-B-488 Type I, Grade C Au on oxygen free copper. Pre-plating surface roughness (Ra) of 262 nm (600 grit finish).

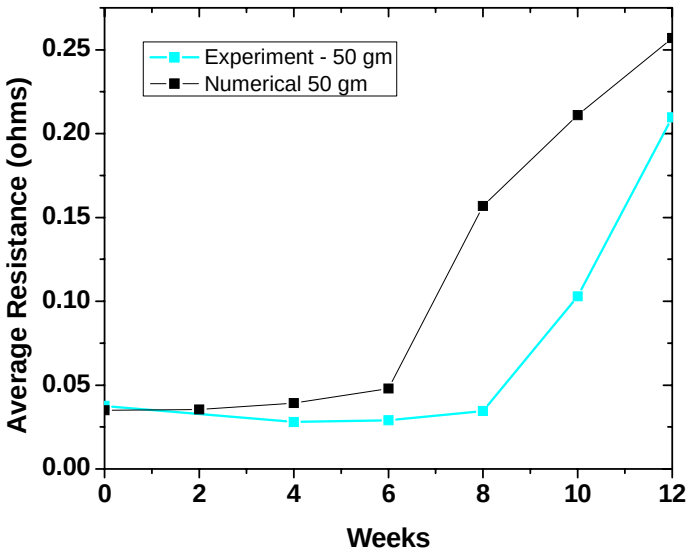

(a)

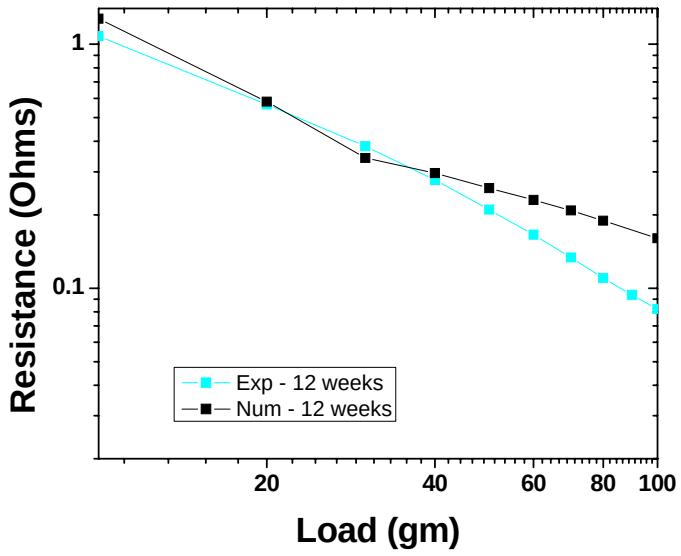

(b)

Fig. 57 Matching numerical vs experiment on aged coupons. (a) Time behavior of the 50% CPD values of the 50 gm numerical and experimental results. (b) 50% CPD values for the Numerical and experiment vs. load at 12 weeks.

Fig. 55 contains the pictures of the degradation of Au-plated copper coupons as a function of time for coupons corroded in the GES atmospheric corrosion testing exposure system. The coupons look increasingly splotchy as a function of exposure, indicating that halo effects are a significant part of the corrosion process. Fig. 56 contains results for the average contact resistance as a function of load measured from the Au-plated copper coupons.

We attempted to match the 12 week experimental data. The results for a 50% CPD are shown in Fig. 57, where we attempted to match the results at a load of 40 gm, and then see how well the dependence at other loads faired against experiment. At low loads, there is good agreement between the model and experimental data. However, at high loads the model exhibited a smaller fall-off compared to experiment. The time behavior of the numerical model, displayed in Fig. 57 (a), roughly captures the experimental behavior as well. In order to understand the model, a more detailed presentation of the model is contained in Fig. 58.

There are two regimes in Fig. 58 broadly represented by an absolute resistance of 0.15 to 0.5 and 0.5 to 4 ohms. The high data of 0.5 and larger cm actually represents the onset of surface occlusion by the large blooms portion of the model. Only a small portion of the geometric surface is open to allow the conduction in this part of the parameter regime. The other data represent conduction through asperities that are all coated by a thin layer of sulfide. The dependence on load in this layer mostly has to do with the predicted thickness of the oxide left after the contacting process, Eqn. (99), and the predicted total area of the asperity contact as a function of load, see Eqn.(77), i.e., there is conduction through a thin corrosion film on each asperity. There is no blockage of the surface due to large bloom effects for most of the cases, except for the tails of the CPD distributions.

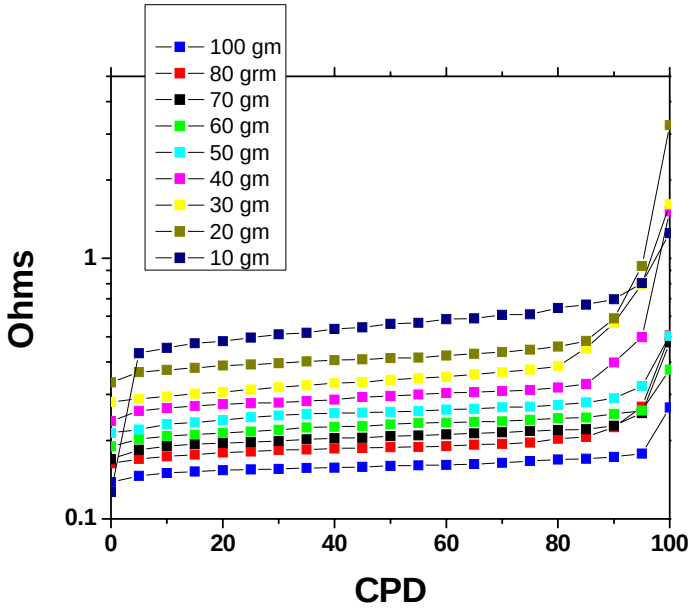

Fig. 58 Numerical results on aged coupons.

The reason for this is that the 0.45 ohm absolute contact resistivity level doesn't allow any other reasonable physical mechanism other than conduction through a thin corrosion film that coats each asperity for its explanation.

Fig. 55 illustrates that halo effects, created by creep corrosion from pores, dominates the behavior in the late time region. We have developed an ad hoc way of describing the growth of the halo, as it compares to the bloom, and have developed an ad hoc way to add its effects to the model for the electrical contact resistance. The controlling models that are critical for this parameter regime (i.e., Eqn. (99)) are currently all empirical in nature and await the development of an experimental discovery process.

Quantifying the relationship between halo and flower awaits detailed experimental discovery. Determination of a model for halo growth also awaits an experimental determination of the mechanism for halo growth, an exciting problem. There has been some qualitative work on how an electrical probe interacts with a halo by Martens et al. [32]. The results demonstrate that direct contact with a halo severely degrades an electrical contact, with the halo material acting like "paste". How the probe interacts with these big blooms, however, isn't understood or calibrated with experiment. Given these uncertainties and unknowns, the model does sufficiently well to claim qualitative agreement.

7.6 Studies of Low Relative Humidity Corrosion in Plated Geometries

In the past sections we have attempted to study how well the numerical model can predict the baseline experimental cumulative probability distribution data and past experimental and numerical models have solely been calibrated on 70% relative humidity data.

We have recently carried out experimental results on plated Au coupons using a 10% relative humidity. The results are presented in Fig. 59. Surprisingly very little corrosion was observed during a 14 week interval compared to the 70% relative humidity case.

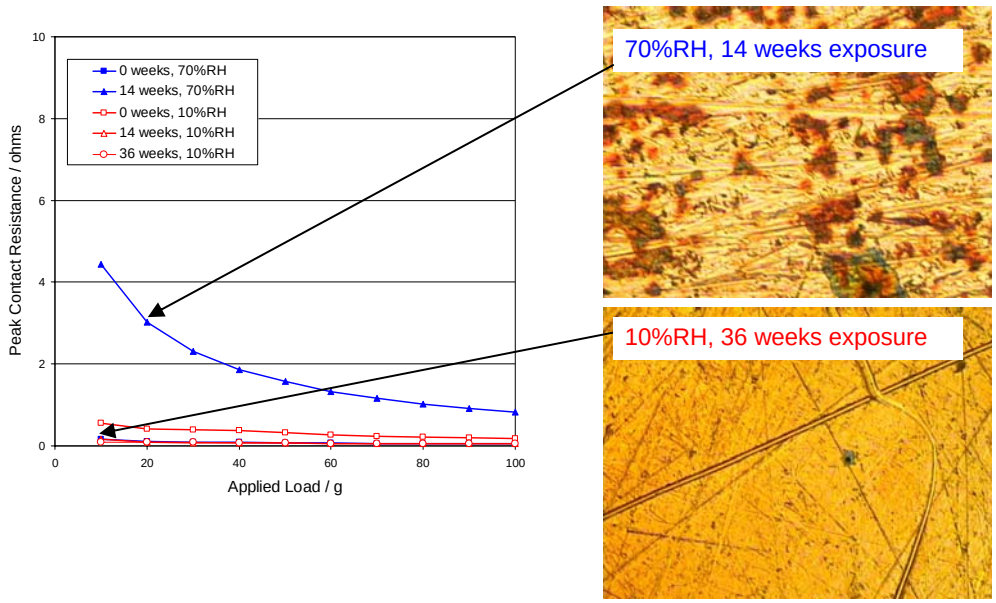

Fig. 59 Effect of the Relative humidity on the corrosion rate of Au or AuNi plated copper coupons.

The results from Fig. 59 should be placed in contrast to our earlier work on bare coupons, an example of which is provided in Fig. 10, Fig. 11, and Fig. 12. In the earlier work it was discovered that the corrosion proceeded on copper coupons at a very rapid rate for close to zero relative humidity. What has changed in the Au-plated case that caused the corrosion rate to be reduced so severely?

We have no conclusive evidence. However, the answer may lie in the previously seen induction period work displayed in Fig. 4, where it was experimentally determined that there was a humidity dependent induction period before Stage I was developed. It was conjectured that this induction period was caused by the need to puncture the Cu_2O native oxide and that H_2O helped catalyze this process. Additionally, in order to match the experimentally determined flower density growth presented in Fig. 28, we have had to invoke this induction period as an initiation rate constant λ in Eqn. (48).

Clearly, we could extend this initiation rate constant submodel represented by Eqn. (48) to model the 10% RH data represented in Fig. 59, given the experimental justification represented by Fig. 4. It should also be noted that grain size effects may play a significant role. The grain size of Cu_2S is on the order of expected pore sizes. Therefore, interaction of pores and grains may mitigate the growth rate in the 10% RH data, since grains are larger in the10% RH case than in the70% RH case [12]. Resolution of these issues awaits experimental discovery.

8.0 Summary

A model describing corrosion of gold plated copper and its effects on the resulting electrical contact resistance has been developed to study the aging of Au-plated copper electrical contacts. Experimentally, Au-plated copper coupons with two different thicknesses have been exposed to H_2S contaminated air and monitored for corrosion products. Site density, site distribution, and resistance data were taken over twelve weeks. The growth kinetics is based on earlier work of Larson et al. We have included pore-site initiation to account for an increase of observed bloom sites as a function of time and have included bloom passivation to account for relatively time-independent bloom distributions. Simulation results show that the model predicts the experimentally observed electrical resistance data at early times and overpredicts beyond the first week. This is due to the continual growth of corrosion film and blooms in the simulations, whereas the experimental data show little increase in electrical contact resistance as the coupons age. Finally, the distribution of experimental ECR is particularly biased towards large blooms, and the model only partially succeeds at accommodating this skewness by increasing the contact resistance for large blooms. A greater contribution to the ECR due to halo films around the blooms may be needed to be added to the model to portray the large tails in the ECR distribution found in this set of experimental data.

References

1. I. M. Notter, D. R. Gabe, "Polarization Resistance Methods for Measurement of the Porosity of Thin Metal Coatings", *Corrosion Science*, **34**, 851–870 (1993).
2. G. S. Frankel and J. W. Braithwaite, "Corrosion of Microelectronic and Magnetic Data-Storage Devices," Chapter 18 in Corrosion Mechanisms in Theory and Practice, 2nd edition, P. Marcus and J. Oudar, ed., Marcel Dekker, Inc., New York, 2000.
3. R. Larson, "A physical and mathematical model for the atmospheric sulfidation of copper by hydrogen sulfide," *J. Electrochemical Society*, **149**, B40–B46, 2002.
4. N. Sorensen et al., "Predicting the effects of corrosion on the performance of electrical contacts," *Electrochemical Society Proceedings*, vol. 2001, 22. 2001.
5. K.S. Chen, "Multi-dimensional modeling of atmospheric copper-sulfidation corrosion on non-planar substrates," Sandia Report, SAND2004-5878, Sandia National Labs, 2004.
6. J. Braithwaite, et al., "A modeling approach for predicting the effects of corrosion on electrical-circuit reliability," Sandia Report, SAND2003-0359, Sandia National Labs, 2003.
7. M. Sun et al., "A kinetic model for noble plated electrical contact behavior," *Scripta Mater*, 42, 1–8, 2000.
8. T. E. Graedel, J. P. Franey, G. J. Gualtieri, G. W. Kammlott, D. L. Malm, On the Mechanism of Silver and Copper Sulfidation by Atmospheric H_2S and OCS," *Corrosion Science*, **25**, 1163–1180 (1985).
9. S. P. Sharma, Reaction of Copper and Copper Oxide with H_2S, *J. Electrochem. Soc.*, **127**, 21–26 (1980).
10. D. W. Rice, P. Peterson, E. Be. Rigby, P. B. P. Phipps, R. J. Cappell, R. Tremoureux, "Atmospheric Corrosion of Copper and Silver," *J. Electrochem. Soc*., **128**, 275–284 (1981).
11. J. C. Barbour, J. P. Sullivan et al, "Mechanisms of Atmospheric Copper Sulfidation and Evaluation of Parallel Experimentation Techniques, Sandia Report, SAND2002-0699, Sandia National Labs, 2002.
12. J. P. Sullivan, J. C. Barbour, et al., "The effects of varying humidity on copper sulfide film formation," Sandia Report, SAND2004-0670, Sandia National Labs, 2004.
13. J. C. Barbour, J. W. Braithwaite, A. F. Wright, "Determination of solid-state sulfidation mechanisms in ion-implanted copper," *Nuclear Instruments & Methods in Physics Research, Section B Beam Interactions with Materials and Atoms*, **175**, 382-387 (1999).
14. K. Kosuge, *Chemistry of Non-stoichiometric Compounds*, Oxford University Press, Oxford, 1994.
15. M.J. Campin, "Microstructural investigation of copper corrosion: Influence of humidity," PhD Thesis, New Mexico State University, 2003.
16. H. K .Moffat, "Analysis of a stagnation point flow reactor design for use in corrosion experiments, Braithwaite's effluent experiments, "Sandia Internal Memo, Sandia National Labs, Albuquerque, NM, Sep. 2000.
17. L. H. Allen, E. Buhks, "Copper electromigration in polycrystalline copper sulfide," *J. Appl. Phys.*, **56**, 327–335 (1984).

18. R. Berger, R. V. Bucur, “Potentiometric measurements of copper diffusion in polycrystalline chalcocite, chalcopyrite, and bornite,” *Solid State Ionics*, **89,** 269–278 (1996).

19. A. Sun, H. K. Moffat, “Parameter Estimation of Atmospheric Copper Sulfidation Corrosion Mode,” Sandia Internal Memo, Sandia National Labs, Albuquerque, NM, Jan. 2003.

20. H. K. Moffat, A. Sun, “A Model for the Degradation of a Plated Au/Ni/Cu Electrical Connector due to the Growth of Corrosion Products from Atmospheric Copper Sulfidation,” Sandia Internal Memo, Sandia National Labs, Albuquerque, NM, Jan. 2004.

21. Cantera’s web site, http://sourceforge.net/projects/cantera .

22. Schunk, P. R., P. A. Sackinger, R. R. Rao, K. S. Chen, R. A. Cairncross, T. A. Baer, D. A. Labreche, “Goma 2.0 – A Full-Newton Finite Element Program for Free and Moving Boundary Problems with Coupled Fluid/Solid Momentum, Energy, Mass, and Chemical Species Transport: User’s Guide,” Sandia Report, SAND97-2404, Alb., NM (1999).

23. P. R. Schunk, et al., “Goma 5.0 – A Full Newton Finite Element Program for Free and Moving Boundary Problems with Coupled Fluid/Solid Momentum, Energy, Mass, and Chemical Species Transport: User’s Guide,” Sandia Report,SAND2006-5375/1, Sandia National Laboratories, Albuquerque, NM 2006.

24. H. K. Moffat, “Film Theory Model Approach to Copper Sulfidation – Pointing to where the emphasis should be placed,” Sandia Memo, Sandia National Labs, Albuquerque, NM 9/30/02.

25. Blackwell, B.F., “Demonstration of GOMA/DAKOTA interface for parameter estimation,” Sandia Internal Memo, Sep., 1998.

26. Simmermacher, T., “Slot coating optimization,” Sandia Internal Memo, Mar., 1999.

27. M. Antler, M. H. Drozdowicz, “Gold-Plated Contacts: The Relationship between porosity and contact resistance on elevated temperature aging,” *Plating and Surface Finishing*, pp. 19–21, Sept (1978).

28. Braithewaite, J.W., “Copper sulfidation – constitutive equations,” Internal email, April, 2002, and 4/17/2002

29. Vrentas, J.S. and J.L. Duda, “Diffusion in Polymer-Solvent Systems. II. A predictive theory for the dependence of diffusion coefficients on temperature, concentration, and molecular weight,” *J. of Polymer Science: Polymer Physics Edition*, **15**, 417–439, 1977.

30. R. J. Geckle, R. S. Mroczkowski, “Corrosion of Precious Metal Plated Copper Alloys Due to Mixed Flowing Gas Exposure,” *IEEE Transactions on Components, Hybrids, and Manufacturing Technology*, **14**, 162–169 (1991).

31. O. A. Svedung, L.-G. Johansson, N.-G. Vannerberg, “The Influence of NO_2 and Cl_2 at Low Concentrations in Humid Atmospheres on the Corrosion of Gold-Coated Contact Material,” *IEEE Transactions on Components, Hybrids, and Manufacturing Technology*, **9**, 286–292 (1986).

32. R. Martens, M. Pecht, “An Investigation of the Electrical Contact Resistance of Corroded Pore Sites on Gold-plated Surfaces,” *IEEE Trans. On Advanced Packaging*, **23**, 561–567 (2000).

33. W. H. Abbot, “The Development and Performance Characteristics of Mixed Flowing Gas Test Environments,” *IEEE Transactions on Components, Hybrids, and Manufacturing Technology*, **11**, 22–35 (1988).

34. M. S. Frant, “Copper Sulfide Creep on Porous Electroplating,” *J. Electrochem. Soc*., **107,** 1009 (1960).

35. V. Tierney, “The Nature and Rate of Creepage of Copper Sulfide Tarnish Films over Gold Surfaces,” *J. Electrochem. Soc.*, **128**, 1321 (1981).

36. F. Hilderbrand, Advanced Calculus for Applications, Prentice Hall, Englewood Cliffs, NJ, 2nd Ed., 1976.

37. J. Greenwood, “Constriction resistance and the real area of contact,” *Br. J. Applied Physics*, **7**, p. 1621, 1966.

38. R. Malucci, “Multispot model of contacts based on surface features,” *Electrical Contacts*, 625–634, 1990.

39. R. Malucci, “Dynamic model of stationary contacts based on random variations of surface features,” *IEEE Transactions on Components, Hybrids, and Manufacturing Technology*, 15, 339–347, 1992.

40. J. A. Greenwood, H. H. Tripp, “The Elastic Contact of Rough Spheres,” *J. Appl. Mech.*, 153-159 (1967).

41. R. Malucci, “Making contact to aged surfaces,” *IEEE Transactions on Components, Hybrids, and Manufacturing Technology*, **16**, 424–430 (1993).

42. L. Boyer, “Contact Resistance Calculations: Generalizations of Greenwood’s Formula Including Interface Films,” *IEEE Transactions on Components and Packaging Technologies*, **24**, 50–58 (2001).

43. R. D. Malucci, “Effects of Wipe on Contact Resistance of Aged Surfaces,” *IEEE Trans on Components, Packaging, and Manufacturing Tech. – Part A*, **18**, 701–707 (1995).

44. Y. Kimura, “Estimation of the number and mean area of real contact points on the basis of surface profiles, *Wear*, **15**, 47–55 (1970).

45. J. A. Greenwood, “The area of contact between rough surfaces and flats,” *J. Lubrication Technol.*, 81–87 (1967).

46. S. Harada, K. Mano, “The effects of surface roughness on electrical contact resistance,” in Proc. Engineering Seminar on Electrical Contact Phenomena, 39–48 (1967).

47. R. Holm, Electric Contacts, Springer-Verlag, New York, 32-37 (1967).

48. J. Trip, S. M Garte, “The gas tightness of separable base metal electric contacts,” in Proc. 26th Holm Conf. On Electric Contacts, pp. 227–236 (1980).

49. R. D. Malucci, “Effects of Wipe on Contact Resistance of Aged Surfaces,” Proceedings of the 40th IEEE Holm Conf. On Electrical Contacts, 131-144 (1994).

50. M. M. Yovanovich, “Four Decades of Research on Thermal Contact, Gap, and Joint Resistance in Microelectronics,” *IEEE Transactions on components and packaging technologies*, **28**, 182–206 (2005).

51. E. Takano, K. Mano, “The Failure Mode and lifetime of Static Contacts,” *IEEE Transactions o Parts, Materials, and Packaging*, vol. PMP-4, 51 (1968).

52. W. H. Abbott, “Recent Studies of Tarnish Film Creep,” *Electrical Contacts*, p. 117–121 (1978).

53. M. Antler, Corrosion Control and Lubrication of Plated Noble Metal Connector Contacts, IEEE Transactions on Comp. Pack., and Manufacturing Tech. A, 19, 304, 1996.

54. W. H. Abbott, “Corrosion of Porous Gold Plating in Field and Laboratory Environments,” *Plating and Surface Finishing*, 72–75, **74** (1987).

55. R. Martens, M. Pecht, “Effects and Interactions of design parameters for gold-plated electric contacts,” *J. of Materials Science: Materials in Electronics*, **11**, 209–218 (2000).

56. H. H .Law C. A. Holden, J. Sapjeta, G. R. Crane, S. Nakahara, Electrical Contact Phenomena of Nickel Electrodeposits with Sharp Micro-Asperities," *IEEE Trans. On Components, Hybrids, and Manufacturing Technology*, **14**, 585–591 (1991).

57. R. D. Malucci, "Accelerated Testing of Tim-Plated Copper Alloy Contacts," *IEEE Transactions of Components and Packaging Technology*, **22**, 53 (1999).

58. R. S. Timsit, "Electrical Contact Resistance: Fundamental Principles", in *Electric Contacts*, Ed. P. G. Slade, p. 1–88, Marcel Dekker, N. Y. (1999).

59. M. G. Pecht, L. T. Nguyen, and E. B. Hakim, *Plastic-Encapsulated Microelectronics*, John Wiley and Sons, New York, 1995.

Appendix A: Details of the Model Implementation

The model is separated into three logical segmented programs. The first program calculates the growth of Cu_2S through the pore using two one-dimensional treatments linked together. The second program combines the rate kinetics of the first program with the statistics involved with the number of pores and their distribution to derive an estimate of the uniform corrosion film thickness and the number distribution of large blooms and halos that interfere with the contacting process. The last program, `contactRes`, calculates the resulting contact resistance based on those inputs and on parameters related to the contacting process.

In this appendix we will describe the inputs to each of these three codes and the information contained in their connecting text files. We will first describe a common utility used within the connecting text files to describe a 1D probability distribution.

A-1 Definition of Normalized Binned Probability Distribution

Figure A-1 contains a schematic of a binned normalized probability distribution. This distribution is used throughout the code to describe probability distributions and to advect these probability distributions forwards in time using first order PDE's. The probability distribution, P_i, is given at a finite number of points, x_i. A control volume is assumed to exist centered at each point. In that control volume the probability distribution is assumed to be constant. The control volumes extend to the midpoints between the points, x_i, except for the first and the last point. The first and last points are labeled x_0 and x_n, where $n+1$ is the number of points. The control volumes start and end at x_0 and x_n, respectively. The integral over these control volumes of the probability distribution is equal to one; this relationship is stated mathematically in Eqn. (110).

$$1 = \sum_{i=0}^{n-1} 0.5\left(P_i + P_{i+1}\right)\left(x_{i+1} - x\right) \tag{110}$$

The probability distribution may be thought of as a discontinuous function in x, $P(x)$, where

$$P(x) = \begin{cases} P_o & x_o < x < \dfrac{x_i + x_{i+1}}{2} \\ P_i & \dfrac{x_{i-1} + x_i}{2} < x < \dfrac{x_i + x_{i+1}}{2} \\ P_N & \dfrac{x_{N-1} + x_N}{2} < x < x_N \end{cases} \tag{111}$$

$P(x)$ is zero outside the range of x_0 and x_N .In order to obtain a dice roll against the probability distribution, we first must form the function,

$$F(x) = \int_0^x P\left(x\right) dx \quad , \tag{112}$$

which can be thought of as all of the probability distribution which is smaller than the value, x. Then

$$y(x) = F^{-1}(x) \tag{113}$$

may be defined as the inverse function of $F(x)[]$. And, $y(x) = F^{-1}(P[0,1])$ where $P[0,1]$ represents a uniform dice roll between 0 and 1, is therefore the transformed deviate that corresponds to the probability distribution, $P(x)$, defined by Eqn. (111).

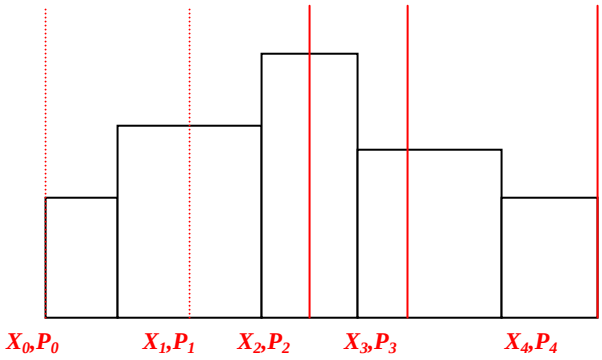

Fig. A-1 Schematic of a binned normalized probability distribution. Red numbers represent the probability distribution, P_i, at the position, X_i. Control volumes are centered on the red lines. The area under the black curve is defined to be equal to one.

Other types of normalized probability distributions are also used in the code. For example, a hat distribution (in $\log(x)$) is used to describe the initial pore distribution function. In all cases the integral $F(x)$ function and its inverse $F^{-1}(y)$ is used to calculate transformed deviates according to the underlying probability distributions.

In order to advect these probability distributions according to a first order PDE, it serves to just to advect the boundaries of these distributions, i.e., the black lines in Fig. A-1, along the characteristics lines of the first order PDE. Then, the integral probability within these lines is conserved and may be reevaluated to conserve the total amount of probability between the characteristics.

A-1 Model for the Flower Growth

Calculation of the kinetics for bloom growth is handled by the first of the programs called, `cu2s_mps`. Essentially it handles the rate of growth of all possible pore sizes, represented by Eqn. (46) in the main text. For each sized pore, it also handles the rate of "pore death" by the Kirkendall voiding mechanism. Fig. A-2 and Fig. A-3 contains a sample input deck for `cu2s_mps`.

The input file is structured in terms of nested blocks. Within each block are "cards" which have keylines, i.e., everything before the "=" sign, and values, which is everything after the "=" sign. Cards may be required or may be optional. An exclamation point or the "# "symbol at the beginning of a line denote the start of a comment. The sample input deck is structured to give an explanation of the card as a comment just before the value of that card is given. It's assumed that units are specified in the CGS system, except where noted.

The card `Diffusion Coefficient` specifies the value of D_V used in Eqn. (3), while the value of the card `Initial Thickness` specifies the initial height of the Cu_2S layer that the diffusion calculation starts off with. This initial thickness and the initial value of the vacancy concentration, specified by the card `Initial Vacancy Concentration` don't actually affect the numerical answers to the program, since their values are set to small enough quantities. An initial thickness is needed, however, in order to initiate the diffusion calculation. The domain then grows with time, with the mesh expanding with the growing domain.

The `Molar Concentration of Lattice` card specifies the density of the Cu_2S lattice. It's assumed that the diffusing species, C_V, is a substitutional impurity located on the copper lattice.

The cards labeled "`Problem 1 - CS Mechanism A1", Problem 1 - CS Mechanism Aneg1,` and `Problem 1 - CS Mechanism A2` are inputs for the corresponding preexponential factors in Eqns. (1) and (2). The activation energy in Eqn. (1) for the forward and reverse direction is set at 6.3 kcal mol-1, while the activation energy for the forward direction in Eqn. (2) is set to 0 kcal mol^{-1}.

The card labeled `Problem 3 - Au Plating Thickness` determines the thickness of the Au plating through which the corrosion product initially grows.

The card `Number of Grid Points` specifies the number of control volumes in the moving control volume simulation.

The `MPS - Low Value of the Pore Size = 2.E-5` and the `MPS - High Value of the Pore Size = 8.E-5` cards specify the values of r_p^a and r_p^b in Eqn. (44). Pores size densities are distributed according to Eqn. (47). The number of pore calculations is given by the card `MPS - Number of Pore Size Calculations = 40` . Pores size calculations are logarithmically distributed between the r_p^a and r_p^b values, according to Eqn. . (47), with the binned probability distribution (see section A-1) being evenly distributed in the $\log\left(r_p\right)$ coordinate.

The card `Kirkendall Cutoff Beta = 4` specifies the value of the adjustable rate constant β in Eqn. (55), which determines the rate of cutoff of large-volume blooms.

Fig. A-3 contains a continuation of the `cu2s_mps` input deck. It contains the items dealing with the time integration of the equations. Each pore size is integrated in time from the initial time, 0, to the final time given on the card , `Final Time = 7.2576E6` . given in seconds. Intermediate data is written out at fixed times to the output file, given in the card, `Intermediate Output Delta Time = 0.6048E6`. Currently, it's set at a day. The intermediate times are used to the method to delineate what times are used for further processing of the simulation data.

```
! Gas Temperature - double (no default) (required) units = Kelvin
Temperature = 298.
!-----------------------------------------------------------------
! Initial Thickness
Initial Thickness = 1.0E-6
!-----------------------------------------------------------------
! Diffusion Coefficient (default = 1.0)
!         (units = cm2/sec)
Diffusion Coefficient = 7.0E-8
!-----------------------------------------------------------------
! Initial Vacancy Concentration (default = 1.0)
!         (units = mol/cm3)
Initial Vacancy Concentration = 1.523E-12
!-----------------------------------------------------------------
! Molar Concentration of Lattice
!               (i.e., each Cu2S counts as one)
!               Units = mol /cm3          default = 1.0
Molar Concentration of Lattice = 3.52E-2
!-----------------------------------------------------------------
! Problem 1 - CS Mechanism A1
!             Preexponential for the reaction on the gas Cu2S surface
!             involving the creation of Cu2S lattice sites and Cv from H2s.
!             units = cm/sec default = 2.71E5 cm/sec.
Problem 1 - CS Mechanism A1 = 4.00E7
!-----------------------------------------------------------------
! Problem 1 - CS Mechanism Aneg1
! Prexponentialf for the reverse reaction that creates
!     Cu2S lattice sites from H2S.
!     units = cm4/mol/s   default = 1.01E5 cm4/mol/s
Problem 1 - CS Mechanism Aneg1 = 4.27E3
!-----------------------------------------------------------------
!  Problem 1 - CS Mechanism A2
! -> Prexponentialf for the reaction with extinguishes
!       copper vacencies at the copper - copper sulfide interface
!     units = cm4/mol/s    default = 9.97 cm4/mol/s
Problem 1 - CS Mechanism A2 = 2.0E2
!-----------------------------------------------------------------
!  Problem 1 - CS Mechanism X_H2S
!                 Input mole fraction for H2S
!                  units = unitless         default = 1.41E-7
Problem 1 - CS Mechanism X_H2S = 10.000E-9
!-----------------------------------------------------------------
!  Problem 3 - Au Plating Thickness
!                -> Input thickness of plating
!                    units = cm      default = 1.E-4
Problem 3 - Au Plating Thickness = 1.1684e-4
!-----------------------------------------------------------------
! Number of Grid Points - int (default = 10) (required)
!           Specify the number of grid points to use in the control volume method.
Number of Grid Points = 100
!-----------------------------------------------------------------
! MPS - Low Value of the Pore Size (default 1.0E-5)
!            Multiple Pore Size Run -> Specify the lowest value of the
!                       pore size to be attempted.  The default is 1.0E-5 cm or 0.1 micron.
MPS - Low Value of the Pore Size = 2.E-5
!-----------------------------------------------------------------
! MPS - High Value of the Pore Size (default 1.0E-4)
!         Multiple Pore Size Run -> Specify the highest value of the
!              pore size to be attempted.  The default is 1.0E-4 cm or 5.0 micron.
MPS - High Value of the Pore Size = 8.E-5
!-----------------------------------------------------------------
! MPS - Number of Pore Size Calculations (Default 10)
!                  Number of Pore size calculations
MPS - Number of Pore Size Calculations = 40
!-----------------------------------------------------------------
! Kirkendall Cutoff Beta (default 0.0) (optional)
!      Proportionality factor for specifying the probability
! of a pore being cut-off from further growth.
Kirkendall Cutoff Beta = 4.
```

Fig. A-2 Excerpts from an input deck for `cu2s_mps`

```
##########################################################################
# START BLOCK TDCADS TIME STEP PARAMETERS
##########################################################################
!----------------------------------------------------------------
! Initial Time Step - double (no default) (required)
!    units = sec
!  Initial time step
Initial Time Step = 1.0E-7
!----------------------------------------------------------------
! Final Time - double (no default) (required)
!    units = sec
!  Final time for integration = 84 days = 12 weeks
Final Time = 7.2576E6
! ---------------------------------------------------------------
! Intermediate Output Delta Time (0.0) (optional)
!        This time is used by the UQ algorithm to provide intermediate
!        solution output at a sequence of times. (2 weeks) units = sec
Intermediate Output Delta Time = 0.6048E6
!----------------------------------------------------------------
! PrintFlag - Int (default 1) (optional)
!               Set the amount of printing from each time steo
PrintFlag = 1
! ---------------------------------------------------------------
! Maximum Number of Time Steps - Int (default large) (optional)
                                                      !
!  Set the maximum number of time steps
Maximum Number of Time Steps = 1000000
! ---------------------------------------------------------------
! Relative Time Step Error Tolerance - dbl (default 1.0E-3)
!                                          (optional)
!               limits 1.0E-9 < RTol < 0.5
!  Set the relative time step error tolerance
Relative Time Step Error Tolerance = 1.0E-3
! ---------------------------------------------------------------
!  Absolute Time Step Error Tolerance - dbl (default 1.0E-6)
!                                       (optional)
!               limits 1.0E-30 < ATol < 1.0E-4
!  Set the absolute time step error tolerance.
Absolute Time Step Error Tolerance = 1.0E-15
! ---------------------------------------------------------------
!  Number of Constant Delta T Time Steps - int (default 0)
!                                          (optional)
!               limits 0 < num < MAX_INT
!
!  Set the number of initial time steps that will be taken
!  where the time step error control will not be applied.
Number of Constant Delta T Time Steps = 2
! ---------------------------------------------------------------
!  Print Solution Every n Steps  - int (default 1)
!                                    (optional)
!               limits 0 < n < INT_MAX
!  Set the time step interval at which the solution
!  will be printed. This defaults to printing at every
!  time step
Print Solution Every n Steps = 0
! ---------------------------------------------------------------
!  Print Solution at n Regular Intervals - int ( default 0) (optional)
!                limits 0 < n < INT_MAX
!  Prints the solution at n regular intervals wrt to the  final time, TOUT.
Print Solution at n Regular Intervals = 0
! ---------------------------------------------------------------
!  Print Solution for first n Time Steps - int (default 0)
!                                         (optional)
!              Prints the solution at the first n time steps.
Print Solution for first n Time Steps = 0
```

Fig. A-3 Excerpts from an input deck for `cu2s_mps`

A-2 Calculation of the Uniform Product Growth

The `cu2s_pore` program takes the calculated flower growth distribution and sets up some rules for how it is distributed between a uniform product growth and large blooms, as a function of time. The basic mathematics for this is described in Section 4.0. `cu2s_pore`, solves the first order PDE equation for the probability distribution of bloom heights as a function of time.

The program takes as its input an ascii file, `cu2s_distribution.txt`, created from `cu2s_mps`. As described in the last section, it contains a description of the pore growth kinetics and death rates as a function of the pore size and time. It then propagates the pore probability distribution in time via the method of characteristics. It keeps track of the distribution of both live and dead flowers. Finally it makes decisions about which flowers will be thrown into the uniform corrosion bin and which flowers will be considered as discrete statistical events.

The output file from the `cu2s_pore` program is called `ProbDens_CorrosionProd.txt`. It contains a normalized probability distribution for the discrete flowers as well as a single corrosion film thickness value at each of the intermediate times delineated in the `cu2s_mps` program.

Fig. A-4 and Fig. A-5 contains a sample of a `cu2s_pore` input deck. Several options are repeated from the previous program, and their description won't be repeated here.

The parameter "`CRP - Length of Wipe`" specifies the length of the wipe. Essentially, this option influences the size of blooms that gets treated as large and therefore statistically, versus those that get lumped into a constant corrosion product. The total volume of small blooms is assumed to comprise a uniform surface corrosion product layer and is used as input to contact resistance model. The cutoff formula for treating blooms statistically is given by Eqn. (114).

$$V_{bloom} > f\,\sigma\left(A_{hertz} + l_{wipe} D_{hertz}\right) \tag{114}$$

If a bloom occupies an area larger than a fraction, f, of the product of the Hertzian contact area, A_{hertz} and diameter, D_{hertz}, and surface roughness, σ, then the effect of the bloom is treated in a different manner. The bloom fraction cut off, *f*, is an adjustable parameter in the model, nominally set to 0.01. This choice of *f* reflects bloom population in a subset of "small" and all of "medium and above" categories. If the bloom area exceeds *f*, then parts of the Hertzian contact area will be unavailable for direct contact except via conduction through the corrosion product bloom due to steric hindrance. Wipe serves to greatly increase the area over which the bloom product may be "wiped" below the thickness where it would preclude close contact between the two surfaces. This empirical model serves to adjust the degree of a tail end distribution on CPD plots for electrical contact resistance.

Eqn. (114) contains the expression for D_{hertz}, the diameter of the Hertzian contact area. In order to calculate this area, details of the contact process need to be supplied to cu2s_pore. These input parameters are listed in Fig. A-5. These parameters specify the input for calculation of Eqn. (69).

```
Type of Pore to Bloom File = GrowthRateMatrix
!  Problem 3 - Au Plating Thickness
! -> Input thickness of plating (cm)
Problem 3 - Au Plating Thickness = 1.1684e-4
!-------------------------------------------------------------
! MPS - Low Value of the Pore Size (default 1.0E-5
! Multiple Pore Size Run -> Specify the lowest value of the
! pore size to be attempted.
! The default is 1.0E-7 cm or 0.1 micron.
!-------------------------------------------------------------
MPS - Low Value of the Pore Size = 2.E-5
                  ! MPS - Low Value of the Pore Size = 30.E-6
!-------------------------------------------------------------
! MPS - High Value of the Pore Size (default 1.0E-4)
! Multiple Pore Size Run -> Specify the highest value of the
! pore size to be attempted.
! The default is 5.0E-4 cm or 5. micron.
!-------------------------------------------------------------
MPS - High Value of the Pore Size = 8.E-5
!-------------------------------------------------------------
! MPS - Number of Pore Size Calculations (Default 10)
! Number of Pore size calculations
! the default is 10.
MPS - Number of Pore Size Calculations = 40
!-------------------------------------------------------------
! MPS -Distribution Type of Pore Sizes
! This specifies P_s the pore distribution function.
! By definition, the integral over the distribution must equal 1
! The default is 1
! 0 - log pore size is evenly distributed between
!     PO.MPS_LPoreSize and PO.MPS_HPoreSize
! 1 - log pore size is distributed in a hat function fashion between
!     PO.MPS_LPoreSize and PO.MPS_HPoreSize
MPS - Distribution Type of Pore Sizes = 1
!-------------------------------------------------------------
! MPS - Average Density of Pores (per cm-2)
! This input card specifies the average density of pores on
! the sample. It's what you get when you take a photograph
! of a sample, and visually count the number of pores that
! show up as a function of the area.
! default = 1 cm-2
MPS - Average Density of Pores (per cm-2) = 2.5E04
!-------------------------------------------------------------
! CRP - Length of Wipe = [double]
! This input card specifies the Length the wipe (cm) under load
CRP - Length of Wipe = 0.0
!-------------------------------------------------------------
```

Fig. A-4 Sample input deck for `cu2s_pore`.

The output of the `cu2s_pore` program is fairly simple. For each time output, it produces an estimate of the uniform corrosion product in cm. It produces a binned normalized probability distribution for the large blooms, and an associated number density of large blooms. The axis of this distribution is the bloom radius. These values comprise the sole input to the contact resistance subprogram defined in the next section.

```
!-------------------------------------------------------------
! CRP - Probe Radius = [double] [required]
!
! This input card specifies the nominal radius of the probe.
! The actual radius of the contacting area will be
! calculated from the Heinz stress formula for elastic
! solids.          units = [cm]
CRP - Probe Radius = 0.15
!-------------------------------------------------------------
! CRP - Probe Load = [double] [required]
! This input card specifies the force that the probe makes
! when contacting the contacting plate. The units of the
! force are in grams.   units = [gm]
CRP - Probe Load = 30.
!-------------------------------------------------------------
! CRP - Contact Modulus of Elasticity [double] [optional]
!  Modulus of elasticity of the proble
!  default = 87.E10 (gold)  units = cgs
CRP - Contact Modulus of Elasticity = 125.E10
!-------------------------------------------------------------
! CRP - Contact Surface Roughness [double] [required]
(CONTINUED)
```

Fig. A-5 Sample input deck for `cu2s_pore (cont)`.

```
!-------------------------------------------------------------
!   Type of Corrosion File = [single time | multiple times ]
!  Determines which file type to process.
Type of Corrosion File = single time
!-------------------------------------------------------------
!  Problem 3 - Au Plating Thickness
! -> Input thickness of plating
!     units = cm
!     default = 1.E-4
Problem 3 - Au Plating Thickness = 1.0E-4
!-------------------------------------------------------------
! CRP - Length of Wipe = [double]
! This input card specifies the Length of the wipe under
! load
! units = [cm]
CRP - Length of Wipe = 0.025
!-------------------------------------------------------------
! CRP - Probe Radius = [double] [required]
! This input card specifies the nominal radius of the probe.
! The actual radius of the contacting area will be
! calculated from the Heinz stress formula for elastic
! solids.
!units = [cm]
CRP - Probe Radius = 0.5
!-------------------------------------------------------------
! CRP - Probe Load = [double] [required]
! This input card specifies the force that the probe makes
! when contacting the contacting plate. The units of the
! force are in grams.
CRP - Probe Load = 100.
!-------------------------------------------------------------
! CRP - Contact Modulus of Elasticity [double] [optional]
!
!  Modulus of elasticity of the proble
!  default = 125.E10 (gold)
!  units = cgs
CRP - Contact Modulus of Elasticity = 125.E10
!-------------------------------------------------------------
! CRP – Contact Microhardness [double] [optional]
! Microhardness of the softest material
! Default = 170.E3
! Units = PSI
CRP – Contact Microhardness = 170.E3
```

Fig. A-6 Input file for `contactRes` program

A-3 Electrical Contact Resistance Model

In the previous sections, an evolution model for the growth of copper sulfide blooms is created and documented. It must be linked to a contact resistance model such that the impact of corroded surface topology may be assessed. The program `contactRes` takes the corrosion product as described in the file `ProbDens_CorrosionProduct.txt` and produces an estimate of the cumulative probability distribution of contact electrical resistances at each discrete time. Output is written to the file `CPG_ContactResistance.txt`, which contains the cumulative probability distribution function for a set of discrete times. It should be noted that contact with respect to all blooms in the normalized probability distribution are treated in a statistical manner, i.e., according to the algorithm described in Section 5.2.1. The distinction between a uniform corrosion product layer and a discrete bloom has already been made in the program `cu2s_pore` and the results incorporated into the input file for `contactRes`.

```
!-------------------------------------------------------------
! CRP – Contact mdivh0 [double] [optional]
! Scaled slope of the asperities
! Default = 2.78E4 / 2.54
! Units = number / cm
CRP – Contact mdivh0 = 1.094E4
!-------------------------------------------------------------
! CRP - Contact Surface Roughness [double] [required]
! Surface Roughness of the contact / probe combination.
! default = 0.3E-4 (gold)
!units = cm
CRP - Contact Surface Roughness = 0.3E-4
!-------------------------------------------------------------
! CRP -  minimum corrosion film thickness [double] [optional]
! default = 0.0
!   units = cm
CRP - minimum corrosion film thickness = 0.0e-4
!-------------------------------------------------------------
! CRP - Mixing Power Law Exponent [double] [optional]
!  Power law exponent in the mixing rules for asperity contact
! default = 7.0
!    units = unitless
CRP - Mixing Power Law Exponent = 7.0
!-------------------------------------------------------------
! CRP - Probe Resistivity [double] [optional]
! Defaults to copper (1.7E-6 ohm cm)
! -------------------------------------------------------------
CRP - Probe Resistivity = 1.7E-6
!-------------------------------------------------------------
! CRP - Surface Resistivity [double] [optional]
! Defaults to gold (2.255E-6 ohm cm)
! -------------------------------------------------------------
CRP - Surface Resistivity = 2.255E-6
!-------------------------------------------------------------
! CRP - Corrosion Film Resistivity [double] [optional]
!
!   Units are Ohm Cm. Note valid ranges of this
!   go up to 1.0E14 and go down to 0.01, depending on the material system
!   the 1000 is for Cu2O, 0.01 would be for Cu2S, and 1.0E14 would be
!   for aluminum oxides.
!   This defaults to 0.1 Ohm cm
CRP - Corrosion Film Resistivity 0.1
!-------------------------------------------------------------
! CRP – Series Resistance
!     Added resistance due to conduction through metal
!     units = volts, default = 0.0
CRP – Series Resistance = 0.0
```

Fig. A-7 Input File for `contactRes` program (cont)

Fig. A-6 and Fig. A-7 contains excerpts from the input file to `contactRes`. Much of it is self-explanatory. The card `CRP – Contact mdivh0 = 1.094E4` defines the horizontal one-dimensional density of asperities. Therefore, the total number of asperities at low loads is actually proportional to the square of this number. However, it should be noted that results are less dependent on this value than one might think, because the relative area of contact is not affected by this value. We have no definitive experimental data for the value of `Contact mdivh0` so we have stuck with a nominal value supplied by Malucci. The card `CRP - Contact Surface Roughness = 0.3E-4` specifies the roughness of the surface in the vertical direction. The default value is again a nominal value in rough agreement with supplied vendor data.

One of the most important tasks in creating an agreement between experiment and theory is to making an agreement between the zero time results. We have included two modifications to the original electrical contact treatment to accommodate agreement with experiment at the zero time level. One is to add in an initial corrosion product that is formed before the actual accelerated corrosion experiments start. The card `CRP - minimum corrosion film thickness = 0.0e-4` supplies this initial thickness. The default value is zero. However, nominal values for the initial product measured (using Auger) from vendor supplied data have been in the range of 7.0 nm, consisting of CuO_2 and an organic mixture. Even after a UV ozone treatment, the nominal value is 4.0 nm. Therefore, every surface has some residual film on it, and this parameter may be used to specify it. The relative value of the minimum corrosion thickness and the surface roughness is an important determiner of the initial contact resistance.

The other modification is to add in a series resistance that exists in the experiments before testing for agreement of the model. In actuality, the experiments do include a series resistance. The probe makes contact with the aged surface. However, the measurement actually includes another connection to the coupon via a clamped-wire connection. The experimental device actually measures the combined resistance of the probe –coupon and coupon-clamped-wire interfaces, as well as the resistance created through conduction through the probe and wafer. This series resistance is handled via the `CRP – Series Resistance` card, which has a default of 0 volts.

A-4 Sample Input Deck and Calculation

If the `contactRes` program is run using the input from Fig. A-6 and Fig. A-7, assuming that there is no initial corrosion thickness, the CPD curve in Fig. A-8 will result. The resulting CPD curves for resistance is flat and very close to the constriction resistance limiting value (Eqn. (83)) of 0.5 milliohms for the parameters in Figure A-5. It turns out that there are enough asperities with enough real contact area to cause the constriction resistance, R_{int} , Eqn. (83), to be larger than the resistance through the asperities, R_{spots} , Eqns. (84). In this limit, the contact resistance is experimentally observed to have a -1/3 to -1/2 power law dependence on the applied load; this dependence and relatively low milliohm level values have been observed by multiple researchers [43, 27].

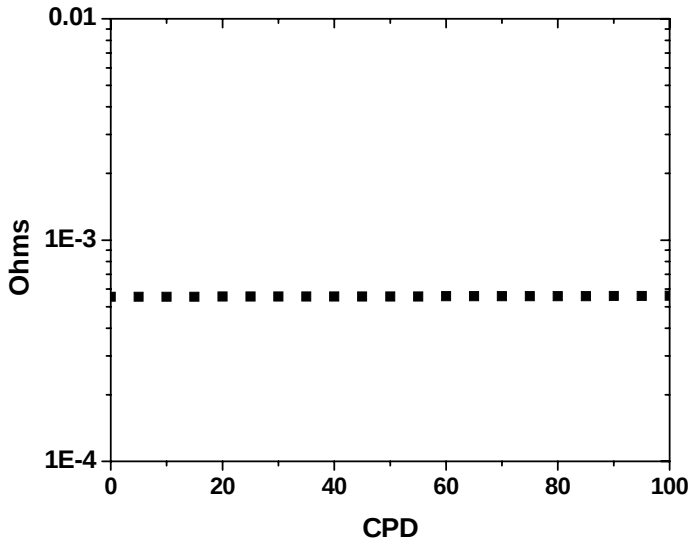

Fig. A-8 Sample Baseline Results for `contactRes` program. Input file from Fig. A-6 and Fig. A-7.

Acknowledgments

The authors would like to thank Mike Starr (1526) for helpful discussions and for a thoughtful review of the manuscript. This work was supported by a Sandia Laboratory ASC and ESC projects. Sandia is operated by the United States Department of Energy under Contract DE-AC04-94AL85000. Sandia is a multi-program laboratory operated by Sandia Corporation, a Lockheed Martin Company, for the United States Department of Energy.

9.0 DISTRIBUTION

1	MS 0346	M. J. Starr 1526
1	MS 0525	P. V. Plunkett, 1734
1	MS 0735	A. S. Sun, 6313
1	MS 0754	L. J. Criscenti, 6316
1	MS 0824	M. R. Prairie, 1510
1	MS 0836	J. S. Lash, 1516
5	MS 0836	H. K. Moffat, 1516
1	MS 0885	J. E. Johannes, 1810
1	MS 0885	J. W. Braithwaite, 1826
1	MS 0888	D. G. Enos, 1825
1	MS 0888	L. M. Serna, 1825
1	MS 0888	S. J. Glass, 1825
1	MS 0888	S. J. Lucero, 1825
1	MS 0889	N. R. Sorensen, 1825
1	MS 1304	J. P. Sullivan, 1132
1	MS 1411	C. C. Battaile, 1814
1	MS 1411	R. A. Roach, 1814
1	MS 9409	R. S. Larson, 8757
1	MS0899	Technical Library, 9536 (electronic copy)


Sandia National Laboratories